ISSN 2189-6909
November 2018

LASTI
Annual Report

Laboratory of Advanced Science and Technology for Industry
University of Hyogo

Vol.19 (2017)

LASTI

PREFACE

This annual report reviews the research activities of the Laboratory of Advanced Science and Technology for Industry (LASTI) in the academic year of 2017 which is from April 2017 to March 2018) including research activities using NewSUBARU light source at the SPring-8 site and other research activities of the micro and nanoscale are carried out energetically at the Center for Advanced Science and Technology (CAST) II.

NewSUBARU facility has a 1.0-1.5 GeV electron storage ring, which provides light beams from IR to Soft X-ray regions. The researches which are carried out are the light sources for next generation through a machine R and D, and the industrial applications such as EUVL lithography, LIGA process, material analysis.

The annual report describes mainly that topics of the NewSUBARU research activities of this year including 1) the research and development of gamma ray application at BL1 beamline, 2) the next generation lithography by Extreme UltraViolet (EUV) lithography at BL3, BL9B, BL9C, and BL10 beamlines, 3) Lithographie, Galvanoformung, and Abformung (LIGA) process technology at BL2 and BL11 beamlines, 4) the chemical analysis using soft X-ray absorption fine structure at (BL5, BL9A, and BL7 beamlines and soft X-ray emission spectroscopy at BL5 and BL9A beamlines at soft X-ray energy region.

Most of our research activities are being conducted in collaboration research works with industries, research institutes, and other universities, inside and outside Japan.

We will continue to respond to the community's demand by offering new science and technology.

Takeo Watanabe

Takeo Watanabe

Director of Laboratory of
Advanced Science and
Technology for Industry,
University of Hyogo

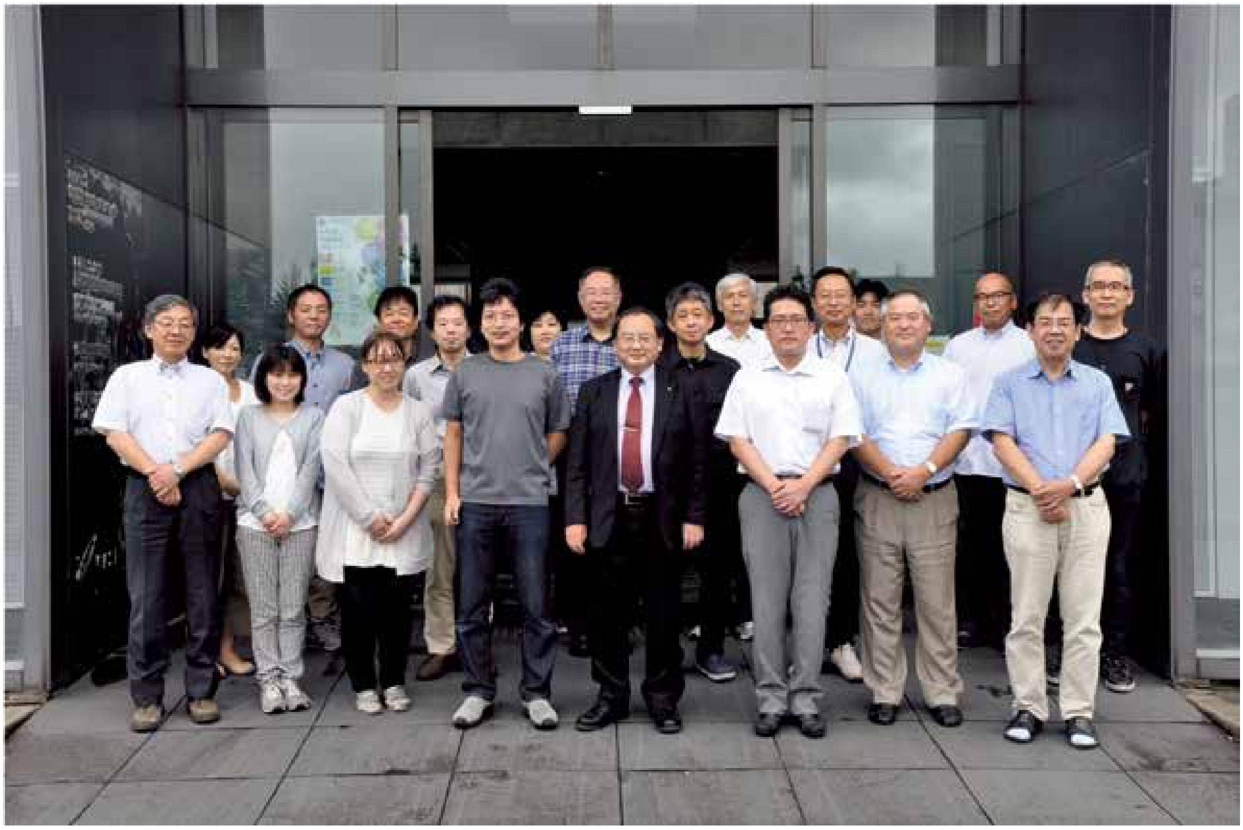

Staff of NewSUBARU
((In front of Advanced Research Building)

The Organization of
Laboratory of Advanced Science and Technology for Industry
University of Hyogo

The organization

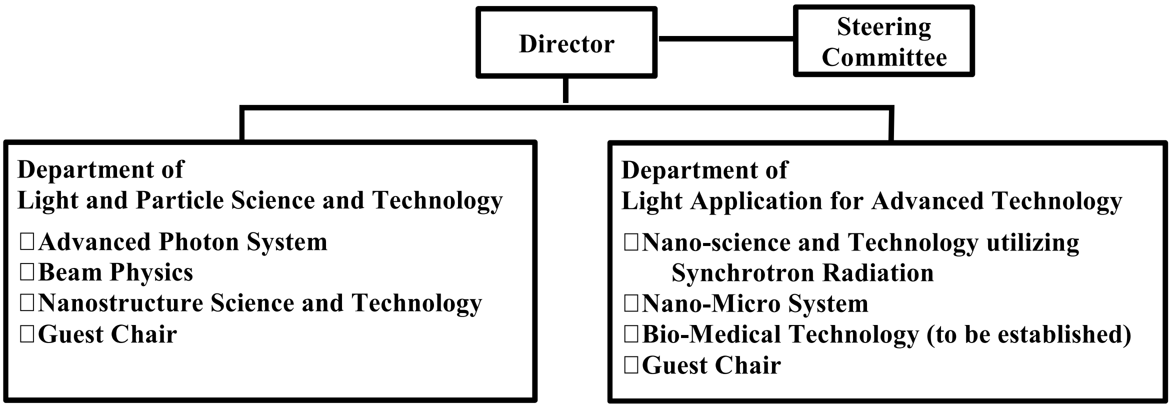

Staff (FY 2017)

Research and faculty staff

WATANABE Takeo, Professor , Director
MIYAMOTO Shuji, Professor
KANDA Kazuhiro, Professor
UTSUMI Yuichi, Professor
SUZUKI Satoru, Professor
NIIBE Masahito, Associate Professor
SHOJI Yoshihiko, Associate Professor
HARUYAMA Yuichi, Associate Professor
YAMAGUCHI Akinobu, Associate Professor
AMANO Sho, Research Associate
HASHIMOTO Satoshi, Research Associate
HARADA Tetsuo, Research Associate
OKADA Makoto, Research Associate

Specially appointed staff

KINOSHITA Hiroo, Professor
TERANISHI Nobukazu,Professor

Administrative staff

HAYASHI Masahiko, General Manager
ISHIHARA Yasunori, Manager
KURODA Takashi, Chief
KANATANI Naoko, NewSUBARU
KUWATA Ayami, NewSUBARU
YAMAMOTO Keiko, CAST
YOKOYAMA Yuka, CAST
HASEGAWA Miwa, CAST
AKAMATSU Sumiyo, CAST
FUJIMAKI Hisae, CAST
YAMAMOTO Mako, CAST
KUSUMOTO Kumi, CAST

Coordinator

FUKADA Noboru, NewSUBARU
FUKUOKA Takao,CAST

Guest staff

MOCHIZUKI Takayasu, Professor
MATSUI Shinji, Professor
OHKUMA Haruo, Professor
ASANO Yoshihiro, Professor
FUKUSHIMA Sei, Professor
BAN Hiroshi,Professor
KUDOU Hiroto, Professor
HORIBE Hideo,Professor
NAGATA Yutaka, Assistant Professor
HARADA Yoshihisa, Assistant Professor

Contact address

Advanced Research Building
3-1-2 Kouto, Kamigori-cho, Ako-gun, Hyogo, 678-1205 JAPAN.
T:+81-791-58-0249 F:+81-791-58-0242
NewSUBARU Synchrotron Radiation Facility
1-1-2 Kouto, Kamigori-cho, Ako-gun, Hyogo, 678-1205 JAPAN.
T:+81-791-58-2503 F:+81-791-58-2504
Web URL http://www.lasti.u-hyogo.ac.jp/, http://www.lasti.u-hyogo.ac.jp/NS/
e-Mail lasti@lasti.u-hyogo.ac.jp
Access http://www.lasti.u-hyogo.ac.jp/NS-en/access/

CONTENTS

Part 1. Current Status of NewSUBARU and Other Light Source

Part 2. Research Activities

List of publications

Part 1. Current Status of NewSUBARU and Other Light Source

Staff of NewSUBARU

（In front of NewSUBARU Facility）

NewSUBARU Storage Ring

Shuji Miyamoto, Satoshi Hashimoto, Yoshihiko Shoji,
Yasuyuki Minagawa, Kazuyuki Kajimoto, Yusuke Hamada
LASTI, University of Hyogo

1. Storage Ring Parameters

The machine parameters of the NewSUBARU storage ring are listed in Table I. The machine condition remains the same with last year.

Table I Main parameters of the NewSUBARU storage ring.

Circumference	118.73 m	
Lattice	DBA+Inv. bending	
Number of bending	12	
Radius of curvature	3.217m	
RF frequency	499.955 MHz	
Betatron tunes	H: 6.30, V:2.23	
Bunch length (sigma)	33ps (normal operation)	
Harmonic number	198	
Radiation loss per turn	33.4 keV (@1GeV)	
Electron energy Mode	1.0GeV TopUp	1.5GeV Decay
Natural energy spread	0.047%	0.072%
Natural emittance	50 nm	112 nm
Storage current	300 mA	350mA

2. Operation Status

The ring has two user-time operation modes, 1.0 GeV top-up operation mode and 1.5 GeV current decay operation mode. The basic operation time is 9:00 - 21:00 of weekdays. Monday is used for machine R&D, Tuesday is for 1.5 GeV user time, Wednesday and Thursday are for 1.0 GeV top-up user time, Friday is for 1.0 GeV or 1.5 GeV user time. Night period or weekend is used for machine study and user time with the special mode, such as a single bunch operation and a changing the electron energy, if necessary. Range of the electron energy is from 0.5 GeV up to 1.48 GeV with 1 MeV step.

The total machine time in FY2017 was 2460 hrs, 99.5% of that of FY2016, excluding the beam down time. Figure 1 shows the breakdown of operation time of the electron storage ring. The beam down time includes not only the down by a failure, but also off-beam periods by a beam abort or others due to the beam instability. The down time due to the machine trouble was 1.1 % of the total operation time.

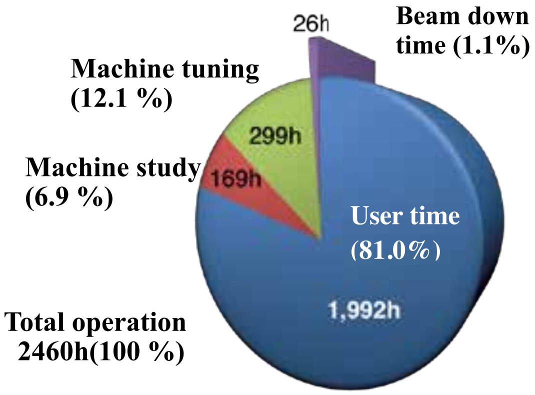

Fig.1 Operating time breakdown of NewSUBARU storage ring in FY2017.

Figure 2 shows overview of the NewSUBARU electron storage ring. The ring is consisted with 6 DBA cells with an inverse bending magnet with auxiliary coil. There are 6 straight sections between each cells, and they are used for an injection septum, an accelerating RF cavity, two undulators and a laser Compton scattering gamma ray source. Electrons are injected from the linac of SPring-8 through the beam transport line (L4BT).

3. Machine Trouble

The machine troubles in FY2017 are listed in Table II. The typical hardware troubles were as follows.

(1) Instability of the new switching power supply for auxiliary coil of the inverse bending magnet.

This type of power supply occasionally oscillates at low operation current. The trouble was settled by changing the deceleration

Table II Machine troubles in FY2017.

Group	Failure / trouble	down time (hr)
Safty interlock	Beam line, L4BT monitor, Emergency earthquake	0.00
Control	GUI, VME, Operator console, Signals	10.77
Magnet	Power supply failure, interlock	1.58
Other	Vacuum, Instability, UPS	13.63
Total		25.98

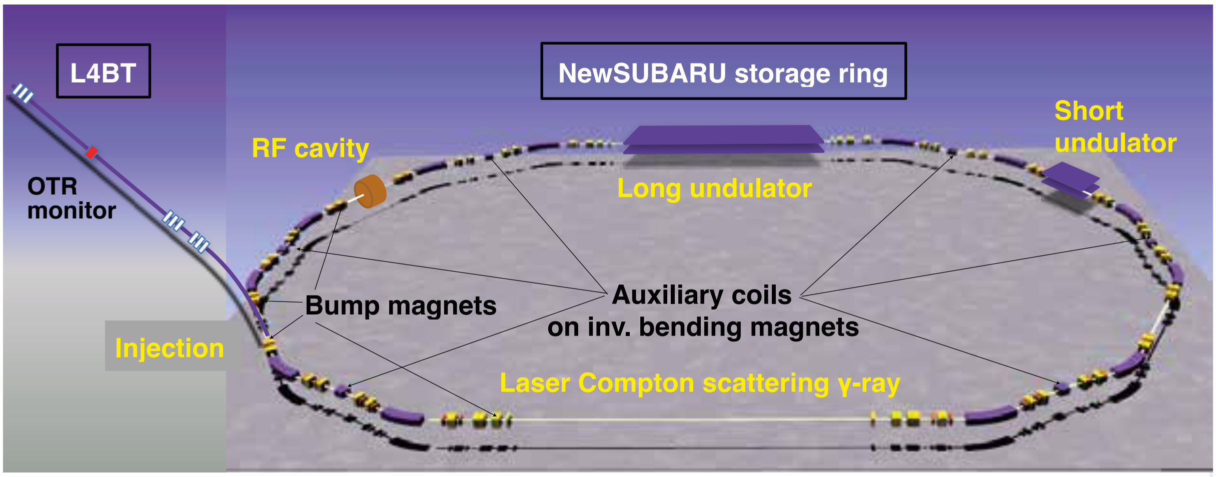

Fig.2. Layout of NewSUBARU electron beam transport line (L4BT) and storage ring. The electron beams are injected from the linac at SPring-8 to the storage ring through transport line.

sequence to keep a sufficient current in auxiliary coil even at low energy operation.

(2) Interlock alarm of power supply.

Power supply for quadruple magnet families often showed “Heat” alarm at start up time. The automatic startup sequence stopped due to this alarm. We are planning to update the quadruple power supply.

(3) Failure of bump magnet power supply.

One of the fore bump magnet was failed due to the broken of the control power supply. This was temporary repaired. All four power supplies will be updated.

(4) Vacuum leak at beam line absorber.

Gradual deterioration of vacuum was detected at a one of the beam line absorber section. The beam line absorber was temporary exchanged with a rigid absorber. This beam line could not be used for about three months, now permanent repair is completed and it is ordinary use.

4. Machine Study and Special User Time

Table III shows the list of machine studies in FY 2017. Some improvements on the operation of accelerator were performed.

Realtime image analysis system for beam profile monitor was developed. This was used for five monitors in the L4BT transport line. The quantitative beam profile and trajectory data improves improved stability of every day injection tuning.

In addition, new OTR beam profile monitor was installed at beam transport line (L4BT). This improved quality of profile monitoring of electron beam compared with the fluorescent plate monitor.

Automatic betatron tune control system is being developed at NewSUBARU. High performance real-time spectra analyzer system (Tektronix RSA306B) realized stable tune monitoring.

The computer aided accelerator control system is being continually improved, for the automatic electron beam injection, acceleration and deceleration.

5. Summary

The NewSUBARU synchrotron light facility has been 20 years since construction. Failures of various equipment are increasing. We will intend to continue stable and sophisticated operation with appropriate inspection and necessary updates of equipments.

Table III List of machine studies and special user mode in FY2016.
(unit is an operation shift = 12 hrs)

R & D theme and special user mode	Responsible person	Operation shifts
New filling test for TOF	S.Miyamoto	3
Accelerator tuning	S.Hashimoto, Y.Shoji	5
Deceleration sequence	S.Miyamoto	5
Long undulator tuning	S.Hashimoto	2
Mirror & Beamline burnt out by SR	K.Kanda, M.Niibe, Y.Haruyama	5
Deceleration sequence	S.Miyamoto	5
Educational student experiments	Y.Haruyama	3

Beamlines

Masahito Niibe
LASTI, University of Hyogo

The arrangement of the beamlines in the NewSUBARU synchrotron radiation (SR) facility is shown in Fig.1. Total nine beamlines are operating in the NewSUBARU SR facility.

Four beamlines of BL01, 03, 06 and 11 were constructed until 1999. Three beamlines of BL07, 09 and 10 were started the operation from 2000.

BL02 beamline was constructed for the usage of LIGA in 2003.

BL03B beamline branched from the BL03 beamline propose for the usage of the EUVL (extreme ultraviolet lithography) microscope for the EUVL finished mask inspection.

BL05 beamline was constructed in response to a demand in the industrial world in 2008, which is the enhancement of the analysis ability in the soft X-ray region with the development of nanotechnology.

BL09B beamline branched from BL09 beamline for the usage of the EUV interference lithography to evaluate. And BL09C beamline branched from BL09B beamline for the usage of the thickness measurement of the carbon contamination originated to the resist outgassing during the EUV exposure.

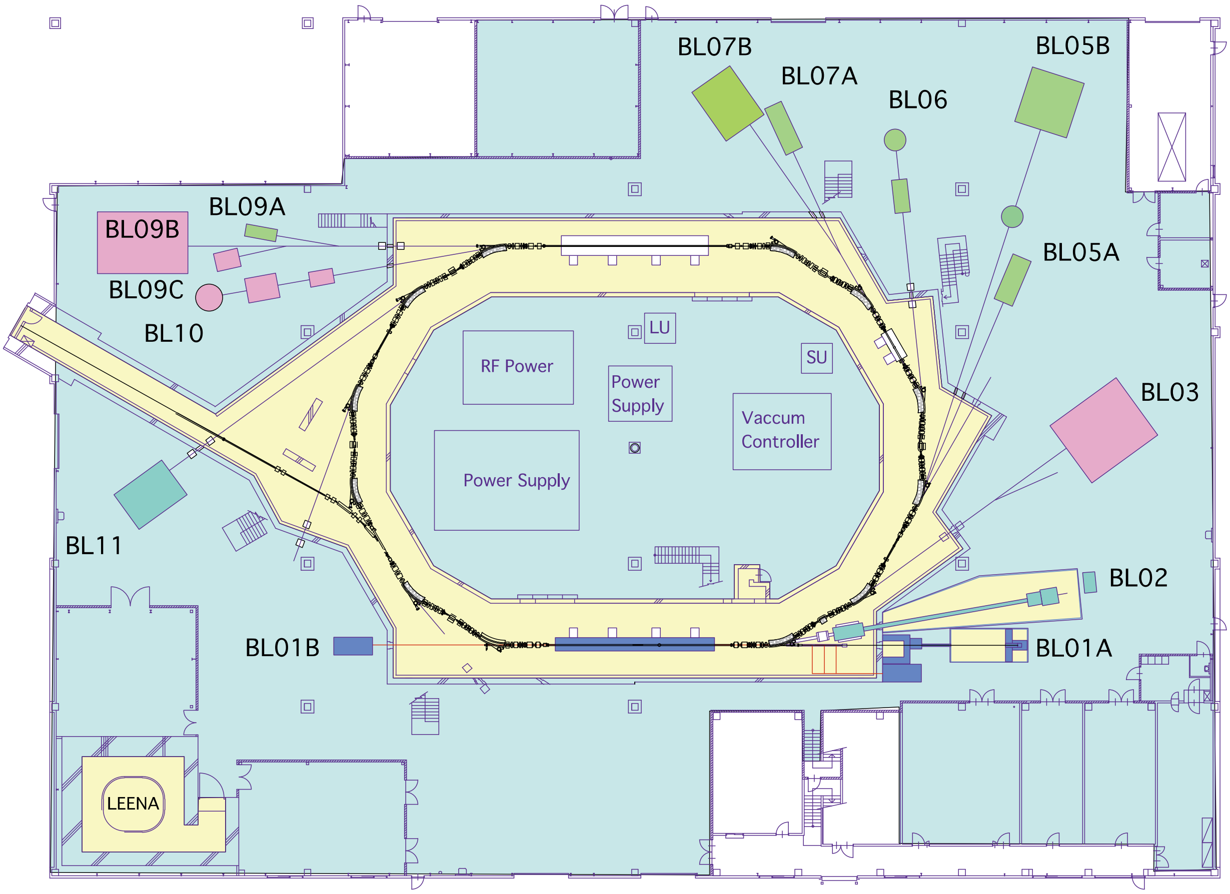

Fig. 1 Beamline arrangement in NewSUBARU.

I. BL01

BL01 is a beamline for research and developing new light sources. Present light source is a polarized quasi-monochromatic gamma-ray beam generated by the laser Compton scattering. Photon energy range of this gamma-ray beam source is from 1MeV to 76MeV with a maximum power of 0.33mW. The layout of the beamline BL01A is shown in Fig.1. This beamline consists of a long straight section on NewSUBARU storage ring and two gamma-ray irradiation hutches. Laser beams are injected from the downstream side of the beamline, and the scattered gamma rays concentrate at narrow divergence angles in the electron beam traveling direction and propagates through the atmosphere, passes through the lead collimator, and reach to the irradiation hatches.

Specification of this gamma-ray sources are listed in Table 1. Gamma-ray irradiation hutch just outside of the storage ring tunnel was constructed in 2004 for gamma-ray experiments. Second gamma-ray irradiation hutch "GACKO" was installed for collaborating with Konan University in 2012. Table 2 shows the measured gamma-ray flux at “GACKO”.

Table 1. Specification of BL01 gamma beam

Max gamma-ray beam power	0.33 mW
Gamma-ray energy range	1.0 - 76 MeV
Gamma-ray polarization	>95%*
Gamma-ray beam divergence	0.5 mrad**

*with 3mmφ collimator.
** E_e=1.0 GeV.
(measured at the irradiation hutch "GACKO")

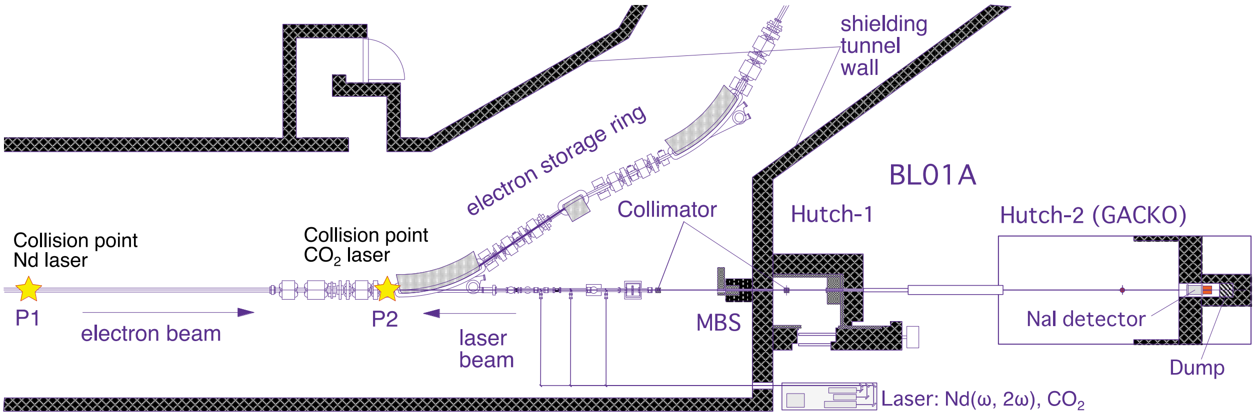

Fig.1 Layout of the gamma-ray beamline BL01.

Table 2. Measured gamma-ray photon energy and flux at GACKO

Laser	E_e=982 MeV, I_e=300mA	E_e=1480 MeV, I_e=300mA
CO_2 laser λ=10.52 μm, P=10W	E_γ=1.73 MeV F_γ=6 x10^5 γ/s (ΔE=10%)	E_γ=3.92 MeV F_γ=6 x10^5 γ/s (ΔE=20%)
Nd: YVO_4 laser λ=1.064 μm, P=10W λ=0.532 μm, P=10W	E_γ 17.0 MeV: F_γ=7 x10^5 γ/s (ΔE=5%) 33.3 MeV: F_γ=3 x10^5 γ/s (ΔE=5%)	E_γ 38.1 MeV, F_γ=7 x10^5 γ/s (ΔE=8%) 74.3 MeV, F_γ=3 x10^5 γ/s (ΔE=10%)
	*with 3mmφ collimator	

E_e is electron energy, I_e is electron current, E_γ is gamma-photon energy and F_γ is gamma-photon flux.

II. BL02

The LIGA (abbreviated name of Lithogaphic, Galvanoformung and Abformung) process which consists from deep X-ray lithography, electroforming, and molding process is one of the promising candidates for such 3D micofabrication. More than hundreds aspect ratio for microstructure can be attained by the usage of the higher energy X-rays (4-15 keV) from synchrotron radiation (SR) with deeper penetration depth to the photosensitive resist. In this system we have succeeded to enlarge the exposure area up to A4 size and the fabrication dimension from submicron to millimeter by varying the energy of the X-ray source in accordance with the size of desired microparts. Microstructure with high aspect ratio over several hundred will be achieved using the X-rays over 10 keV since high energy X-ray has deep penetration depth to the photo-sensitive resist materials. Whereas, in the case of lithography for low energy X-rays from 1 keV to 2 keV, submicron structures with high aspect ratio will be achieved using the X-rays mask with precise line-width and thinner absorber, since low energy X-rays has low penetration depth. Based on this principle, the beamline for x-ray exposure have constructed with continuous selectivity of X-rays from 100 eV to 15 keV by using the X-ray mirrors (plane and cylindrical mirror) and Be film filters. The horizontal angle of the outgoing SR could be obtained up to 12.5 mrad, which corresponds to the horizontal size of 220 mm (A4 horizontal size) at the exposure position. The second characteristic performance of the beamline is the high efficiency differential pumping system. This was necessary for maintain the vacuum difference between the storage ring (<10^{-9} Pa) and the end-station (<10^{-9} Pa) at which gasses for substrate cooling will be introduced in the exposure apparatus.

The flexibility for the shapes and functions of microstructure will be enlarged by achieving 3D microfabrication process using multi step exposure at various configuration between X-ray mask and substrates. The relative positions between X-ray mask and substrates, tilt and rotation angle to the SR incident direction can be moved simultaneously during SR exposure using 5 axis stages. The movement of each axis is controlled by the PC in terms of the scanning speeds, scanning length, and repetition number. In order to decrease the heat load of sample substrate suffered during SR irradiation helium introduction and substrate cooling mechanism were also equipped. Specification of spectrometer is listed in Table 3.

Table 3. Specification of the LIGA exposure system

Optics	Plane and cylindrical mirror, Be filters
Exposure energy	100 - 2 keV, and 4 – 15 keV
Exposure method	Proximity and multi-step exposure
Wafer size	A4 or 8 inch
Exposure area	230 mm(H) ×300 mm(V)
Exposure environment	< 1 atm (He-gas)

III. BL03

BL03 is a beamline for the developing the next generation lithographic technology so called extreme ultraviolet (EUV) lithography. The extreme ultraviolet lithography (EUVL) is a promise technology for fabricating a fine pattern less than 7-nm node. There are (1) a EUV resist-sensitivity evaluation tools, (2) a VUV reflectometer, and (3) an EUV microscope with Schwarzschild optics. At (1) tool, EUV resist is exposed with SR light of EUV monochromatized by 7 Mo/Si multilayer mirrors. The exposure spectrum of this tool was same as the ASML exposure tools. The monochromator of (2) reflectometer was UV – VUV reflectometer. At EUV lithography, out-of-band radiation (100 – 300 nm) of EUV source degrades image quality. Thus, optics and resist property of out-of-band region was essential to evaluate, for example EUV mask reflectivity, and EUV resist sensitivity. The monochromator specification was shown in Table 4. The EUV microscope (3) has Schwarzschild optics, which were fabricated with collaboration of Dr. Toyoda (Tohoku Univ.). The spatial resolution was quite high of less than 28 nm, which was equal to 7 nm at wafer printing size.

Table 4. VUV monochromator specification

Mount type	Collimate plane grating monochromator
Grating	Plane Grating (1,000 l/mm)
Energy range	4 - 120 eV (UV ～ VUV)

Resolving power (E/ΔE)	～1000

IV. BL05

BL05 was constructed in response to a demand in the industrial world, which is enhancement of the analysis ability in the soft x-ray region with the development of nanotechnology. BL05 consists of two branch lines for use in the wide range from 50 eV to 4000 eV. BL05A and BL05B are designed to cover the energy range of 1300-4000 eV and 50-1300 eV, respectively. The incident beam from the bending magnet is provided for two branch lines through different windows of a mask. Therefore, these two branch lines can be employed simultaneously. At the end stations of each branch, the transfer vessel systems were mounted for the measurements of sample without exposure to air. In addition, globe box was placed for the preparation of samples into transfer vessel.

1) The double crystal monochromator was installed at the BL05A. InSb, Ge, Si, SiO_2, Beryl and KTP crystals are prepared for a double-crystal monochromator. Toroidal mirrors are used as a pre-mirror and a focusing mirror of BL05A. XAFS measurement in the total electron yield mode and fluorescence XAFS measurement using SSD (SII Vortex) can be performed. The fluorescence XAFS spectra can be measured for samples at the end station filled with He gas. Table 5 shows the specification of monochromater.

Table 5. Monochromator specification

Monochromator	Double crystal monochromator
Monochromator crystals	SiO2（1010）, InSb（111）, Ge（111）, Beryl（1010）, KTP（110）, Si（111）
Energy range	1300-4000 eV
Resolution	E/⊿E=3000

2) The constant-deviation monochromator consisting of a demagnifying spherical mirror and a varied-line-spacing plane grating (VLSPG), which can provide high resolution, simple wavelength scanning with fixed slits, was mounted on BL05B. The optical system consists of a first mirror (M0), a second mirror (M1), an entrance slit (S1), a pre-mirror (M2), and three kinds of plane grating (G), an exit slit (S2) and a focusing mirror (M3). The including angle of the monochromator is 175°. Two measurement chambers are prepared at the end station of BL05B. The XAFS spectra in the total electron yield mode and fluorescence XAFS spectra using SDD (Ourstex) can be measured in a high vacuum chamber. In addition, the photoelectron spectrum can be measured using spherical electron analyzer (VG Sienta, R3000) in an ultrahigh-vacuum chamber. The chambers can be replaced by each other within 1 hour. Table 6 shows the specification of the monochromator.

Table 6. Monochromator specification

Monochromator	Varied-line-spacing plane grating monochromator
Grating	100 l/mm, 300 l/mm, 800 mm/l
Energy range	50-1300 eV
Resolution	E/⊿E=3000

V. BL06

BL06 has been mainly developed for irradiation experiments such as photochemical reaction, SR-CVD, photo-etching, surface modification. The white radiation beam from bending magnet is introduced to the sample stage using a pair of mirror, whose incident angle was 3°. The SR at BL06 sample stage had a continuous spectrum from IR to soft x-ray, which was lower than 1 keV. A differential pumping system can be utilized for experiments in a gas atmosphere, which is difficult in the soft x-ray region. A sample holder can install four pieces of samples at a time. By using heater set in the sample holder, the sample can be heated from room temperature to 220°C. The temperature of sample is monitored using a Cr-Al thermocouple mounted on the sample holder.

VI. BL07A and BL07B

This beamline was designed for the development of new materials by SR technology. This beamline consists of two branch lines, which are provided with an incident beam from a 3-m-long undulator by switching the first mirror. One of them is a high photon-flux beamline with a multilayered-mirror monochromator for the study of SR-process (BL07A) and another is a high-resolution beamline with a varied line spacing grating monochromator for the evaluation of nano-structure characteristics by SR-spectroscopy (BL07B). The useful range of emitted photons from 50 to 800 eV is covered at both beamlines. The light source of BL07 is a 3-m length planar undulator, which consists of 29 sets of permanent magnets, a period length of which is 76 mm. The incident beam from the undulator is provided for two branch lines by translational switching of first mirror.

1) BL07A

The multilayered-mirror (MLM) monochromator, which has high reflectivity in the soft X-ray region, was installed at the BL07A. It consists of a switching mirror chamber, a slit chamber, a MLM monochromator, a filter chamber and a reaction chamber. To obtain a large photon flux, we decided to use only first mirror (switching mirror), M0, for focusing. The MLM monochromator is designed to cover an energy range of up to about 800 eV by combination of three kinds of mirror pairs with 4 kinds of filter. The flux deliver by this design is estimated to be between a maximum of 10^{17} photons/s at 95 eV and a minimum 2×10^{14} photons/s at 300 eV for a 500 mA ring current. Table 7 shows the summary of BL07A. In addition, X-ray fluorescence (XRF) apparatus using spherical varied line spacing grating was mounted at the downstream of irradiation chamber. The poly capillary was used to enhance beam-condensing efficiency. Measurement energy range was from 30 eV to 450 eV. This XRF apparatus was expected to utilize the chemical analysis on the light metals, Li and Be, and light elements, B, C and N.

Table 7. Summary of BL07A.

Energy range (eV)	Multilayer mirror					Filter	
	Material	spacing	Thickness Ratio	number of layers	ΔE/E	material	Thickness
50-60	Mo/Si	20 nm	0.8	20	6.2 %	Al	100 nm
60-95						None	—
90-140	Mo/B_4C	11 nm	0.5	25	3.3 %		
140-194						Ag	100 nm
190-400	Ni/C	5 nm	0.5	60	2.5 %		
400-560						Cr	500 nm
550-800						Ni	500 nm

2) BL07B

The constant-deviation monochromator consisting of a demagnifying spherical mirror and varied line spacing plane grating (VLSPG), which can provide to high resolution, simple wavelength scanning with fixed slits, was mounted on BL07B. The optical system consists of a first mirror (M0), an entrance slit (S1), a premirror (M1), and three kinds of plane grating (G), an exit slit (S2) and two focusing mirrors (M2 and M3). The monochromator is designed to cover the energy range 50-800 eV with three gratings, of which including angle are 168°. The VLSPG has been well known to obtain high resolution in extreme ultraviolet region by diminishing various kinds of aberration. The total resolving power about 3000 can be realized in the whole energy region. Table 8 shows the specification of the monochromator.

Table 8. Monochromator specification

Mount type	Hettrick-Underwood type
Grating G1, G2, G3	Plane VLS (600, 1200, 2400 l/mm)
Energy range	50-150 eV, 150 – 300 eV, 300-800 eV
Resolving power (E/ΔE)	～3000

VII. BL09

A purpose of this beamline is studies on a soft x-ray interferometry or a holographic exposure experiment with making use of highly brilliant and coherent photon beams radiated from 11 m long undulator in NewSUBARU.

BL09 consists of M0 mirror, M1 mirror, G grating and M2 mirror. M0 mirror is used for horizontal deflection and beam convergence, M1 is used for vertical beam convergence at the exit slit, and M2 is used for vertical deflection and beam convergence. A monochromator is constructed by M1 and a plane grating. The maximum acceptance of the undulator beam is 0.64 mrad in horizontal and 0.27 mrad in vertical. The acceptance can be restricted by 4-jaw slits equipped at upstream of the M0 mirror.

BL09A beamline is used for material analysis: X-ray absorption spectroscopy (XAS) and X-ray photoelectron spectroscopy (XPS). In 2013, X-ray emission spectrometer (XES) was introduced at the endstation of the BL-09A. The energy range and resolving power of the XES system was designed to be about 50-600 eV and 1500, respectively.

BL09B beamline branched from BL09 beamline for the usage of the EUV interference lithography for the evaluation of the exposure characteristics of EUV resist. Coherence length of 1 mm at the resist exposure position was achieved using BL09B beamline. And BL09C beamline branched from BL09B beamline for the usage of the thickness measurement of the carbon contamination originated to the resist outgassing during the EUV exposure. Table 9 shows the specification of the monochromator.

Table 9. Monochromator specification

Mount type	Monk-Gillieson type
Grating	Plane VLS (300, 900, 1200 l/mm)
Energy range	50 – 750 eV
Resolving power (E/ΔE)	～3000

VIII. BL10

BL10 is for EUV reflectometry and soft X-ray analysis. M0 mirror is used for horizontal deflection and beam convergence, M1 is used for vertical beam convergence at the exit slit, and M2 is used for vertical deflection and beam convergence. A monochromator is constructed by M1 and a plane grating. At the beginning, the multilayer reflectivity measurement was carried out at this beamline. The characteristics of this beamline and the result of the Mo/Si multilayer measurement are carried out for the development of the EUV- mask technology.

BL10 utilizes a monochromator of the varied-line-spacing plane grating (VLS-PGM). The line density of the monochromator in central region of the gratings were 600, 1800 and 2,400 lines/mm. The reflectometer has a two axis vacuum goniometer. One axis carries the sample, which may be a mirror surface at the center of the reflectometer vacuum chamber (_-motion). The other (_-motion) carries the detector on a rotating arm. In addition there are linear motions to translate the sample in two orthogonal directions (x,y). All motors are controlled by computer. The reflectivity result obtained at BL10 has a good agreement with that at LBNL. Table 10 shows the specification the monochromator.

The micro-CSM tool was adapted at the most downstream of the BL10 beamline for the EUV mask defect inspection with coherent-diffraction-imaging method. This too is very effective for the inspection of the actinic patterned mask with phase imaging.

A large reflectometer was installed in a branch line for large EUV optical component including EUV collector mirrors. The reflectometer has a sample stage with y, z, [illegible], [illegible], and Tilt axis, which can hold large optical elements with a maximum weight of 50 kg, a diameter of up to 800 mm, and a thickness of 250 mm. The entire sample surface is able to be measured.

Table 10. Monochromator specification

Mount type	Monk-Gillieson type
Grating	Plane VLS (600, 1800, 2400 l/mm)
Energy range	50 – 1,000 eV
Resolving power (E/ΔE)	～1000

IX. BL11

A beam line BL11 is constructed for exposure Hard X-ray Lithography (DXL) in the LIGA (German acronym for Lithographite Galvanoformung and Abformung) process. LIGA process, that utilizes a useful industrial application of SR, is one of the promising technologies for fabrication of extremely tall three-dimensional (3D) microstructures with a large aspect ratio. This process was invented at the Institut Fur Mikrostrukturtechnik (IMT) of the Karlstuhe Nuclear Center (KfK) in 1980. Microstructures with height of over a few hundreds μm have been widely applied to various fields such as micro-mechanics, micro-optics, sensor and actuator technology, chemical, medical and biological engineering, and so on. This beam line was designed by the criteria ; photon energy range from 2 keV to 8 keV, and a density of total irradiated photons [illegible] 10^{11} photons/cm^2. The BL11 can provide the most suitable photon energy for microfabrication in X-ray lithography, while the BL2 is equipped for fabricating fine pattern submicron-scale structure and microstructure with high aspect ratio by selectivity of X-rays using movable mirror system. That is, LIGA process in NewSUBARU can provide the best 3D microfabrication because the BL11 and BL2 are complementary. The beamline BL11 is consisting of an absorber chamber, a first-mirror chamber (M1), a 4-way slit chamber, a Be and polyimide window chamber, and an exposure chamber. The horizontal angle of the outgoing SR could be obtained up to 17.8 mrad, providing a beam spot size on the exposure stage [illegible] 80 [illegible] mm^2. The micron-scale structure with high aspect ratio will be achieved using the toroidal typed mirror M1 which can produce a parallel collimated beam of X-rays. In addition, the homogeneity of the beam is excellently controlled by a novel adding system.

Using the precision stage in the exposure chamber, the flexibility for the shaped and functions of microstructure will be enlarged by achieving 3D microfabrication process using multi step exposure at various configuration between x-ray mask and substrates. The exposure area of 200 mm × 200 mm is brought to fruition. In order to decrease the heat load of sample substrate suffered during SR irradiation, helium introduction and substrate cooling system were also equipped. The specification of the LIGA exposure system is listed in Table 11.

Table 11. Specification of the LIGA exposure system

Exposure method	Proximity exposure
Wafer size	8 inch
Exposure area	200 mm(H)×200 mm(V)
Exposure environment	< 1atm (He-gas)

Establishment of Research Center for Advanced Synchrotron Radiation Analysis

In order to respond to diverse analysis needs from industries, it is necessary to advance technological development for analyzing beamlines (BLs) of NewSUBARU SR facility to advance integrated and strategic development of analyzing technology. For this reason, the Research Center for Advanced SR Analysis was launched in August 2016. As an organization crossing in university courses, this center is consulted and administered by all members of the LASTI related to analysis, and in collaboration with the SR Nanotechnology Center of Hyogo Prefecture, a wide range of energy from hard X-rays to soft X-rays. We aim to respond to various analysis needs of the area on a one-stop basis.

Acknowledgement

We would like to thank all the staff who work at NewSUBARU synchrotron radiation research facility for their help to describe the update details of the beamlines.

Recent improvements on accelerator equipment of NewSUBARU storage ring

Satoshi HASHIMOTO[1], Shuji MIYAMOTO[1], Kazuyuki KAJIMOTO[2], Yasuyuki MINAGAWA[2]
1. LASTI, University of Hyogo 2. JASRI / SES

Abstract

We have been working on improving various kinds of accelerator equipment for more stable operation and the advancement of the NewSUBARU electron storage ring. In this paper we introduce the recent successful improvements on beam monitor systems.

Introduction

NewSUBARU synchrotron radiation facility [1,2] has been operated for nearly 20 years. At NewSUBARU, soft X-ray, EUV light and gamma ray by Compton scattering have been used for mainly industrial applications.

For the stable operation of the accelerator, the measurement and the control of electron beams with higher precision are key issues. In this paper we report the recent improvements of devices for the NewSUBARU storage ring such as;

(1) Profile monitors

Keeping the beam injection efficiency high for a long time is important for a top-up operation of the ring. And it is necessary to know always the status of injected beams. For an easy control of devices and reliable measurements, we upgraded beam profile monitor systems for measuring the status of injected beams.

(2) OTR monitor

We newly developed an OTR monitor for the precise measurement of injected beams.

(3) Noise reduction of Current Transformer

The noise level of a CT near an injection point of the ring, which was affected by pulse magnets such as bump and septum, was reduced.

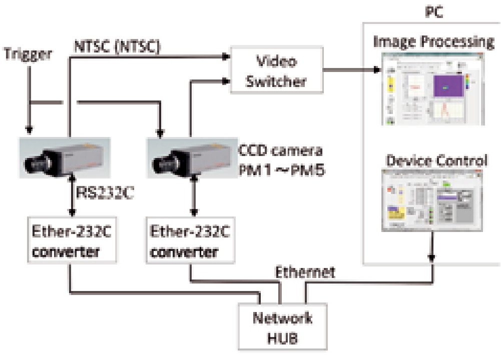

Fig.1 Layout of the image processing and camera control system for L4BT profile monitors.

(4) Upgrade of tune measurement system

By introducing an inexpensive USB-type real-time spectrum analyzer, betatron frequencies of electron beams (tunes) could be measured with higher accuracy and higher update speed than before.

Development of Camera Control and Image Processing Systems for Profile Monitors

1.0 GeV electron beams are injected from the SPring-8 Linac to the NewSUBARU ring through the L4BT beam transport line. To measure position and size of injected beams, five profile monitors (M1~M5) using a fluorescent screen have been used at L4BT. We developed a camera control system that can remotely adjust to the optimum setting for each camera from a PC in the control room as shown in Fig. 1.

We also developed an image processing software, which can measure beam size and position from the observed fluorescence (Fig.2). Because fluorescence was observed by visual observation using a TV monitor previously, the measurement accuracy has been greatly improved.

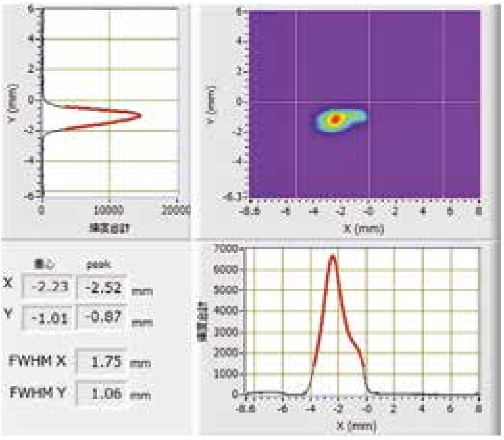

重心 peak
X -2.23 -2.52 mm
Y -1.01 -0.87 mm
FWHM X 1.75 mm
FWHM Y 1.06 mm

Fig.2 Profile monitor image processing software developed using LabVIEW.

Introduction of OTR Monitor to L4BT Beam Transport Line

Because fluorescence light is very bright, it is easily observed but the measured beam size is often over-estimated. In general an OTR (optical transition radiation) monitor is often used in the precise beam measurement in a beam transport and a Linac. When an electron passes through a thin metal film such as Al, due to an abrupt change in dielectric constant, a transition radiation is emitted in a broadband frequency range (Fig.3).

We installed an OTR monitor at the upstream of the L4BT. A GigE camera observes a weak OTR light in an optical region. The OTR light is a very short pulse, so the camera is triggered by a timing signal. Fig. 4 shows the horizontal and vertical beam sizes measured using the OTR monitor. For comparison, the measurement data using the fluorescence monitor (M5) in the immediate vicinity of the OTR monitor. It was found that the beam sizes measured using the OTR monitor are about 75% smaller than those of M5 monitor. The exact beam size measurement makes it possible to optimize parameters of the L4BT for ideal transport of electron beams.

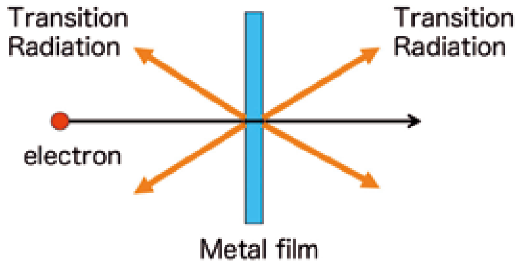

Fig. 3 Transition radiation

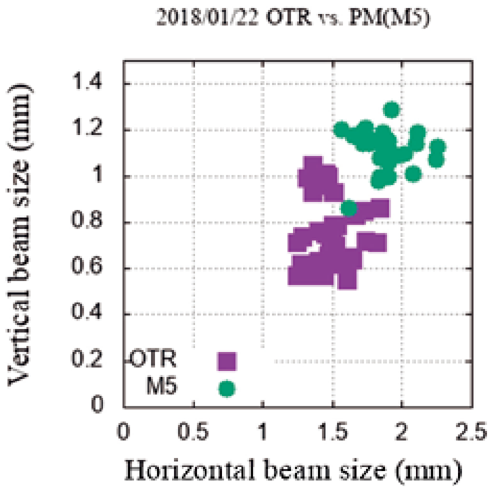

Fig. 4 Horizontal and vertical beam sizes measured by the profile monitor (M5) and the OTR monitor.

Noise reduction in a Current Transformer (CT3) signal

The intensity of the beam passing through the L4BT line can be non-destructively measured using current transformer (CT). In the L4BT, three CTs are used as show in Fig. 5. The CT closest to the ring (CT3) has suffered from severe noises in measured signal, which come from pulsed magnets such as bump and septum through a vacuum chamber and a girder. Thus we have been using CT1 located far from the ring for evaluating beam injection efficiency.

As a result of trial and error, we succeeded in suppressing the noise in CT3 as shown in Fig.6. Before noise countermeasure, the noise intensity was about 70 mV in peak-to-peak. By short-circuiting the downstream of the CT and the vacuum pipe, a ground level fluctuation was canceled and noise disappeared. This made it possible to precisely measure beam intensity just before the ring and to calculate injection efficiency accurately.

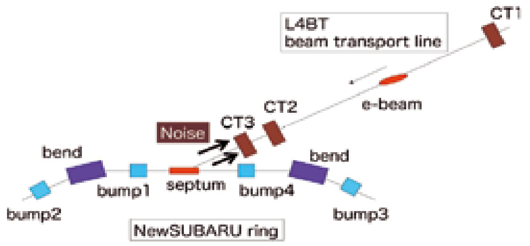

Fig. 5 Layout of the beam injection point of the NewSUBARU ring.

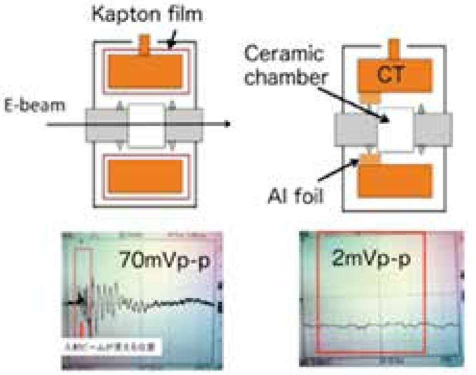

Fig. 6 Reduction of noise in beam signal measured by CT. Before (left) and after (after) the noise reduction.

Upgrade of Tune Measurement System

While stored electrons circulate in the ring, each electron oscillates in both horizontal and vertical directions around a stable closed orbit (betatron oscillation). The number of oscillation per ring circumference is called tunes. For stable operation of the ring, tunes should be kept to the optimum values.

The former tune measurement system was based on PXI platform and could measure tunes with high accuracy. However, because the system performed FFT of an acquired waveform data in a PC, it took time to update the data and was not suitable for high-speed measurement.

In the newly developed system, a differential signal from two electrodes at diagonal positions in one beam position monitor is analyzed in frequency domain using a spectrum analyzer (Tektronix RSA306B). This compact device transferred .the FFT waveform to a PC through USB-3.0 and signal processings such as smoothing, curve-fit, peak detevtion, error handling are performed in an application software developped using LabVIEW. Tune resolution is about 0.0001 and update period is less than 200ms. A smart algorithm was also developped to exclude incorrect results due to a temporal waveform distortion during beam injection, energy ramping.

This tune measurement system with higher update speed and higher accuracy could measure a dynamic change of tunes and is useful to reveal beam dynamics in the ring. Currently, a real-time tune correction system is under development, which will corect tune shift caused by various factors.

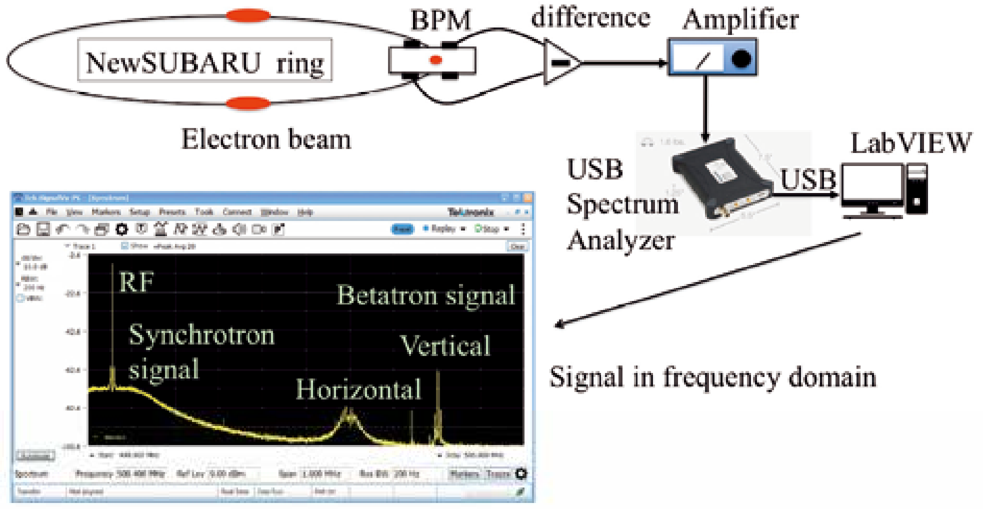

Fig.7 Real-time tune measurement system using USB-type spectrum analyzer.

Summary

Although our facility has lower maintenance cost and lower manpower, we have been working on improving accelerator equipment.

The upgrade of measurement systems on beam injection contributes to a recent stable operation. The tune measurement with high precision and high speed is useful to the reduction of beam instabilities. Stack of small improvements is necessary for the stable operation of a huge device.

References

[1] A.Ando et al., J. Synchrotron Rad., 5, 342-344 (1998)
[2] http://www.lasti.u-hyogo.ac.jp/NS-en

Broadband vacuum ultraviolet lights from solid rare-gas plasmas

Sho Amano
LASTI, University of Hyogo

Abstract

The laser plasma emission spectra in a broadband from 30 to 200 nm of solid Ar, Kr, and Xe targets are presented for the first time. The spectra are composed of a broadband continuum and lines. The spectral intensity integrated from 30 to 200 nm indicates that the VUV average power generated in the wavelength range is 30 mW when the laser energy is 1 J at 1 Hz. The number of photons of monochromatic light after passing through the spectrometer is estimated to be more than 5×10^6 photons/nm/pulse over the wavelength range and is considered to be useful for applications of broadband VUV spectroscopy.

Introduction

Vacuum ultraviolet (VUV) light, whose photon energy is sufficient for ionizing most molecules, interacts strongly with matter. VUV light is therefore useful in many research areas such as surface physics, chemistry, and biology. As VUV light sources, a deuterium discharge lamp, an excimer lamp/laser or the high harmonics of an IR laser have been used, but their emission wavelengths are fixed and lack continuous and wide tunability. However, a widely tunable VUV light source is required in spectroscopy experiments for various material studies. A synchrotron radiation (SR) source is versatile for having continuous tunability over a wide range of VUV to X-ray, but it is not suitable for a small laboratory or a factory, owing to its large size and high cost. Therefore, laser plasma sources that are compact and inexpensive compared with the SR source have been studied to achieve continuously tunable VUV light [1,2].

We have been studying laser plasma sources using solid rare-gas targets that can generate continuously repetitive pulses on a long-term basis [3]. To study the characteristics of VUV emissions from the targets, we developed a VUV spectrometer that could measure the broadband VUV spectra in the wavelength range of 30 to 200 nm. Measurement results showed broadband continuous spectra in the 30–200 nm range from the solid Ar, Kr, and Xe targets, which are the first reports as far as we know. In this paper, we report the VUV characteristics from the solid rare-gas targets including the measured spectra. Finally, we evaluate its performance for VUV spectroscopy.

Experiments

Figure 1 shows the experimental setup of the laser plasma VUV light source, composed of a target supply system and a driving laser. The developed target system was described in detail previously [4].

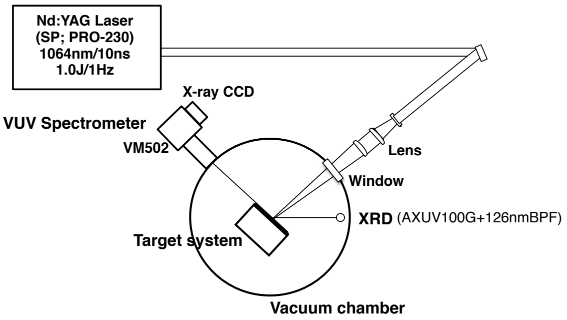

Fig. 1. Experimental setup of the laser plasma VUV source (top view).

To measure the VUV energy generated, an X-ray diode (XRD) (OptoDiode, AXUV100) was located at 45° to the axis of the incident laser beam. A band-pass filter (Acton, 126-N-1D), with transmission in the range from 110 to 200 nm, was placed in front of the diode. To measure the VUV spectra, a VUV spectrometer was located tangentially with respect to the target surface. The spectrometer consisted of a commercial VUV vacuum monochromator (Acton, VM-502-V) and a back-illuminated two-dimensional charge-coupled device (CCD) (Princeton, PI-SX400). The VUV vacuum monochromator contained an iridium-coated grating with a 1200 lines/mm pattern, which covered a range of more than 30 nm, and its focal length and resolution were 200 mm and 0.1 nm, respectively. The exit slit was removed from the VUV vacuum monochromator and the CCD was attached to position its surface at the focal point of the grating. The CCD could record one spectrum from a single shot plasma by triggering an external laser signal.

Results & Discussion

The spectral intensity was calibrated absolutely using the XRD data. The absolutely calibrated emission spectra in the VUV region (30–200 nm) from the solid Ar, Kr, and Xe targets are shown in Fig.

2. This is the first report of such broadband VUV spectra from solid Ar, Kr, and Xe, as far as we know. The irradiated laser energy was 1 J and the laser intensity was 5×10^{12} W/cm^2. These spectra for all targets show that the broadband continuums in the 30–200 nm range and many peaks, which can be attributed to the transitions of charged ions and neutrals. The vertical axis represents the spatially integrated energies generated from the targets at each wavelength. The spectra were also time-integrated and involved both fast excitation and slow relaxation processes. In the fast excitation process when the very hot and dense plasma was produced during the laser pulse irradiation, free-free radiation (Bremsstrahlung radiation) and free-bound electron recombination were the main mechanisms and contributors to the spectral continuum. In the slow relaxation process when the expanded and relaxed plasma was produced after the laser irradiation, bound-bound electronic transitions of ions and neutrals were the main mechanism and contributors to the spectral lines. Figure 2 indicates that the generated VUV energy integrated in the 30–200 nm range was roughly the same (approximately 30 mJ) for all the solid Ar, Kr, and Xe targets. Because the laser repetition rate was 1 Hz, the VUV average power obtained was approximately 30 mW.

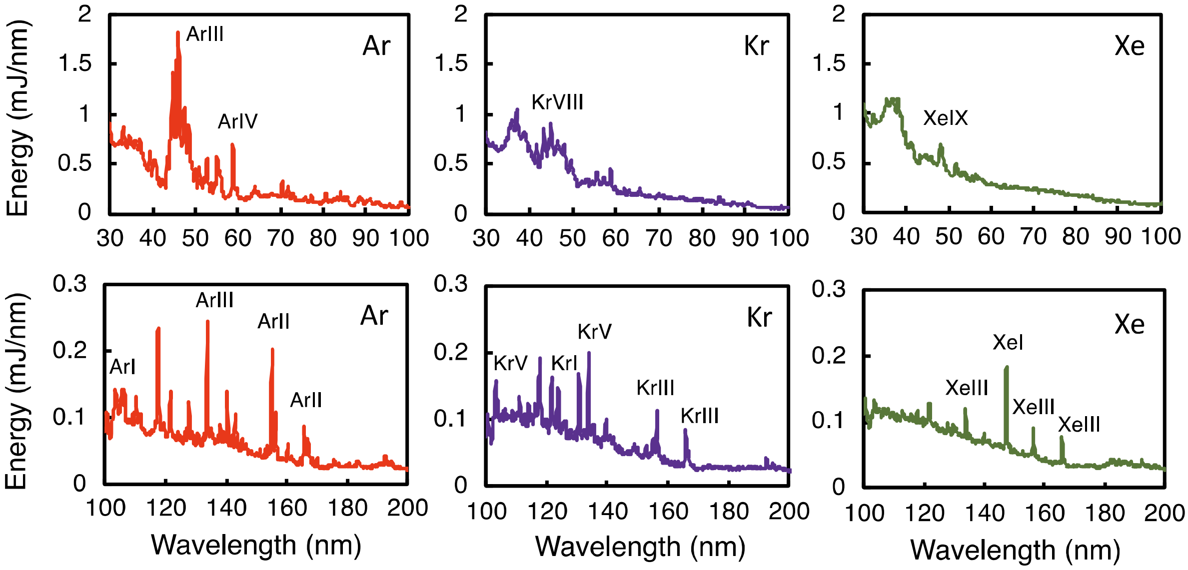

Fig.2 VUV emission spectra in the ranges of 30 to 100 nm (upper) and 100 to 200 nm (lower) from the solid Ar (left), Kr (center), and Xe (right) targets. The vertical axis represents emission energy integrated in total space and time per wavelength. The laser energy was 1 J and the laser intensity was 5×10^{12} W/cm^2.

Finally, we considered the number of photons of monochromatic light after passing through the spectrometer, which could actually be used for spectroscopy. To increase the number of photons as much as possible, we reset the spectrometer at 45° to the axis of the laser beam incidence and measured the spectra again. The spectral shape did not change, but its intensity increased by one order of magnitude compared with that obtained with the initial setup. In the measurement, the number of photons on the CCD was calculated to be more than 5×10^6 photons/nm/pulse over the 30–200 nm range using the CCD sensitivity, when the laser energy was I J at 1 Hz. The number of photons depends on the distance between the spectrometer and the plasma, for example, more than 1×10^8 photons/nm/pulse can be obtained when the spectrometer is placed close at 150 mm. The number of photons is considered to be useful for applications of broadband VUV spectroscopy and is particularly sufficient for photon counting and one-photon ionization spectroscopy. In conclusion, our laser plasma VUV sources using solid rare-gas targets are unique sources that can emit a broadband continuum with wide tunability and can be operated continuously.

Acknowledgments

This work was supported by JSPS KAKENHI (Grant No. 23654204).

References

[1] T. M. Di Palma and A. Borghese, Nucl. Instr. and Meth. B **254**, 193 (2007).

[2] M. Kaku, T. Yamaura, T. Higashiguchi, S. Kubodera, and W. Sasaki, Jpn. J. Appl. Phys. **42**, 3458 (2003).

[3] S. Amano, Appl. Phys. Exp. **9**, 076201 (2016).

[4] S. Amano, Rev. Sci. Instrum. **85**, 063104 (2014).

Mechanical stability of the main axis of double multilayer film monochromator by change of Bragg angles in BL07A

Masato Okui[1, 2], Naoki Yato[1], Ren Konno[1], Akinobu Watanabe[1], Sei Fukushima[2, 3] and Kazuhiro Kanda[2]
1. Kohzu Precision Co., Ltd. 2. LASTI, University of Hyogo, 3.Kobe Material Testing Laboratory Co., Ltd.

Abstract

The mechanical stability of the main axis with elapsed time is one of the basic factors to achieve high stability of beam position from monochromators. The authors have been made preliminary experiment by using BL07A, NewSUBARU to improve the more mechanical of the main axis. In this experiment, the stability of the Bragg angle of its monochromator was measured by a ring scale encoder, when the Bragg angle was 10 degrees and 20 degrees, respectively. The results lead to the possibility that the axis would be drift largely when the Bragg angle is about 20 degrees or upper. This possibility shall lead the necessary that we should produce the new design and new concept for a monochromator and the concept should be the geometry of a monochromator with keeping perfect balance whatever Bragg angle.

Introduction

Recently, the beam size of synchrotron tends to smaller than the previous. Thus, the optical stability that is beam position change by time from upstream monochromators would be important than the previous them. This optical stability from monochromator would be caused by various factors, but the mechanical stability of the main axis with elapsed time is one of the basic factors to solve this optical stability problem.

The authors have been made a preliminary experiment by using Kohzu MKZ-7NS type double multilayer films monochromator set up on the BL07A to improve the more mechanical stability of their main axis.

And in the last year annual report [1], the possibility of mechanical slight drift was pointed out by observation of ring scale encoder. In this report, the preliminary experiment has been continued in this year.

The new facts about the mechanical stability of the main axis in the monochromator was gotten and the reappearance of the last year 's experiment was gotten too.

Experimental

As well as the previous study, the present experimental has been made by using MKZ-7NS type double multilayer films monochromator set up on BL07A in NewSUBARU. This specification of the multilayer films monochromator has already been reported by Okui *et al.*, [2] [3].

Fig. 1 shows the photograph of panoramic view of MKZ-7S type monochromator. The schematic system drawings of MKZ-7S type monochromator is shown as Fig. 2.

Fig.1. Photograph of MKZ-7NS type double multilayer films monochromator.

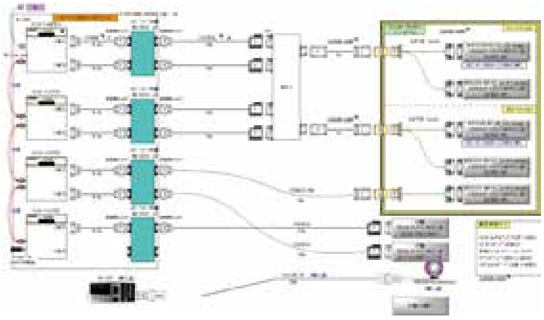

Fig. 2. The schematic system drawings of MKZ-7NS type monochromator.

The experiment was made when the storage ring energy was 1.5GeV, then, the ID gap tuned as 48.3mm after the injection.

The Bragg angle was 10 degree and 20 degree, respectively and the other axes were tuned for each main axis angle. After these tuning, the data of mechanical stability of the main axis theta had been collected.

In during the measurement, the motor pulse of the pulse motor was fixed after the positioning not to move all axes from the positions tuned. The output pulse of the ring scale encoder (Heidenhain RON886) was recorded, and during the experiment the authors checked keeping still each motor pulse values from the initial values.

Result and Discussion

Result of experiment is shown as Fig.3. In the figure, the vertical axis shows relative the positional displacement from the initial position of the main axis θ, Bragg angle after the all axes tuned and the horizontal axis shows the elapsed time since starting each experiment.

The Orange circle and line shows the relative position displacement by elapsed time when the Bragg angle is 10 degrees. As well as the above, blue circle and line shows the relative positional displacement by elapsed time when the Bragg angle is 20 degrees.

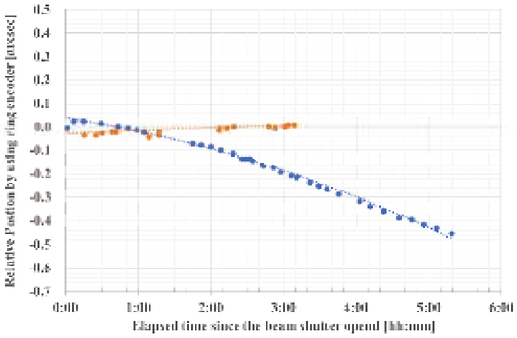

Fig. 3. Mechanical stability of the main axis θ of MK-7NS type monochromator set on BL07A in NewSUBARU.
In this graph the blue circle and line shows the10 degrees case and Orange circle and line shows the 20 degrees case.

Surprisingly, the curves of the relative displacement of the main axis is different between the 10 degrees Bragg angle case and 20 degrees case remarkably in this experiment. The 10 degrees curve is slightly up by elapsed time but almost have kept the initial value, but the 20 degrees curve have been remarkable down by the elapsed time.

The previous study [1] would be made with Bragg angle is 24.19 degrees. the previous result shows a similar curve as the present 20 degrees curve.

From these results, it would be suggested the possibility that the positional drift by the elapsed time of the main axis in MKZ-7NS type monochromator would depend on the Bragg angle. The authors would like to propose the possibility that the axis would be drift largely when the Bragg angle is about 20 degrees or upper.

The schematic design drawing reported by Okui *et al.* [3] is shown as Fig.4.

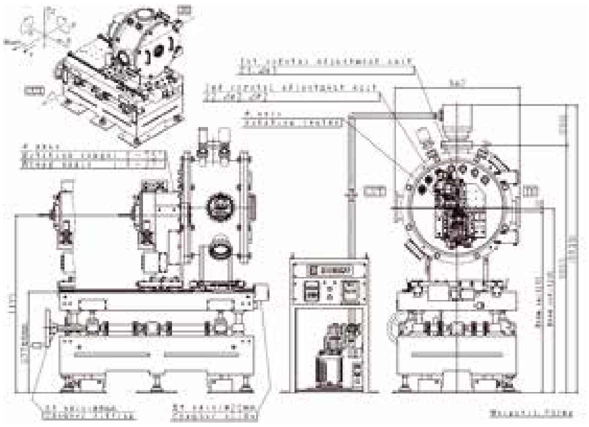

Fig.4. The schematic design drawing of MKZ-7NS type monochromator.

The rotation center of main axis is on the first monochromatic devise, and only Z2 axis go far side when Bragg angle go to higher side. Thus, it is possibility that the center of gravity is slightly different from rotation center when the Bragg angle is high.

This suggestion shall lead the necessary that we should produce the new design and it would be new concept for next generation monochromator and the concept should be the optical geometry of a monochromator keeping perfect balance whatever Bragg angle. For satisfaction with the optical geometry, it is needed that the control system with integrated computing using computing electronic cam.

The authors had the presentation of this electronic cam technology for this monochromator in AnalytiX-2018, Florida, USA in March 2018.

Acknowledgement

The authors thank for support by the project members of the development of next generation monochromator in Kohzu Precision Co., Ltd.

References

[1] Okui *et al.*, LASTI Annual Report, **18(2016)**, 15-16. (2017).

[2] Okui *et al.*, LASTI Annual Report, **17(2015)**, 15-16. (2016).

[3] Okui *et al.*, AIP Conference Proceedings **1741**, 030033, (2016).

Part 2. Research Activities

Dr. Nobukazu Teranishi, guest professor of LASTI, became the first Japanese to win Queen Elizabeth Prize for Engineering in 2017

（Source: http://qeprize.org/photo-gallery/qeprize-presentation-2017/）

Photoneutron cross-section measurements on ^{209}Bi for the IAEA CRP on updating the photonuclear data library

I. Gheorghe[1], H. Utsunomiya[2], the Phoenix* Collaboration
[1] ELI-NP, "Horia Hulubei" National Institute for Physics and Nuclear Engineering,
30 Reactorului, 077125 Bucharest-Magurele, Romania
[2] Konan University, Department of Physics, Okamoto 8-9-1, Higashinada, Kobe 658-8501, Japan

Abstract

The Phoenix Collaboration aims to provide new data of total and partial (γ, xn) cross sections with x=1-3 for 11 nuclides to the IAEA (International Atomic Energy Agency)-CRP (Cordinated Research Program) F41032 on updating the photonuclear data library. For the first measurement within the project, the total and partial photoneutron cross sections for ^{209}Bi have been investigated in the energy range of 7.7 – 42.2 MeV using the quasimonochromatic Laser Compton scattered γ-ray beams provided by the γ-ray Beam Line 1 of the NewSUBARU facility. *(****Pho****to****e****xcitation and* ***n****eutron* ***e****mission cross (****x****) sections.)*

Introduction

A new coordinated research project has been launched by the IAEA to update the current photonuclear data library [1]. One of its main objectives is to provide new total and partial photoneutron cross sections for selected nuclei to resolve the longstanding discrepancies between the Livermore and Saclay data [2].

The Phoenix Collaboration between the Konan University of Kobe, the Skobeltsyn Institute of Nuclear Physics of the Lomonosov Moscow State University and the Extreme Light Infrastructure-Nuclear Physics (ELI-NP) aims to measure the total and partial (γ, xn) cross sections with x=1-3(4) for ^{209}Bi, ^{9}Be, ^{197}Au, ^{181}Ta, ^{139}La, ^{169}Tm, ^{165}Ho, ^{159}Tb, ^{103}Rh, ^{89}Y and ^{59}Co.

Experiments and Results

Photoneutron cross-section measurements were performed in ^{209}Bi(γ, xn) reactions with x=1–4 using Laser Compton scattered (LCS) γ-ray beams at the Beam Line 1 of the NewSUBARU synchrotron radiation facility[3]. A schematic diagram of the experimental setup is shown in Fig. 1.

The high-power Nd:YVO4 laser INAZUMA (Spectra-Physics) was used in the first (λ = 1064 nm) and second (λ = 532 nm) harmonic to produce LCS γ-ray beams with maximum energies between 7.7 and 42.2 MeV. The beam irradiated a ^{209}Bi target placed at the center of the flat efficiency neutron detection system [4] comprised of ^{3}He counters embedded in polyethylene moderator block.

The laser was operated in Q-switch mode at 16.66 kHz frequency, corresponding to 60 µs between consecutive laser bunches. The 60 µs interval was extended to 480 µs by modulating the laser beam intensity with an additional optical system comprised of a Pockels cell and a polarizer which blocked seven out of eight consecutive laser pulses.

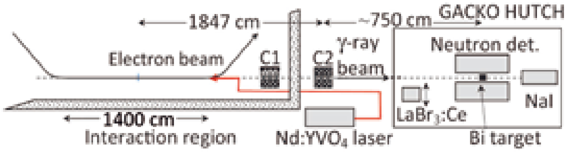

Fig.1 The LCS γ-ray Beam Line 1.

The γ-ray beam energy spectrum was monitored using a large volume lanthanum bromide ($LaBr_3$:Ce) detector. Energy resolution values between 1.6% and 3.2% in FWHM were obtained for the high energy γ-ray beams, above the S_{2n}. The γ-ray beams below the S_{2n} showed a broader energy spread of 4%–7%. The energy spectra and the average path length through the target per incident photon histograms are displayed in Fig. 2 for each of the γ-ray beams.

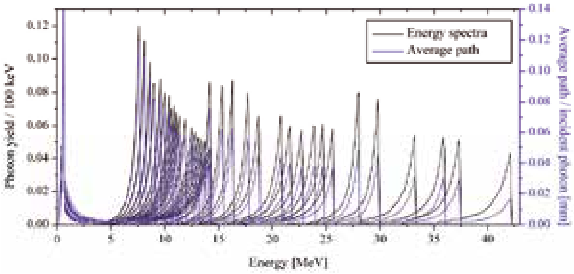

Fig.2 The energy spectra and the average path length through the target per incident photon for each of the incident LCS γ-ray beams.

Above S_{2n}, the number of events in which only one (single N1), only two (double N2), only three (triple N3), and only four (quadruple N4) neutron events were recorded, were determined from the neutron moderation time

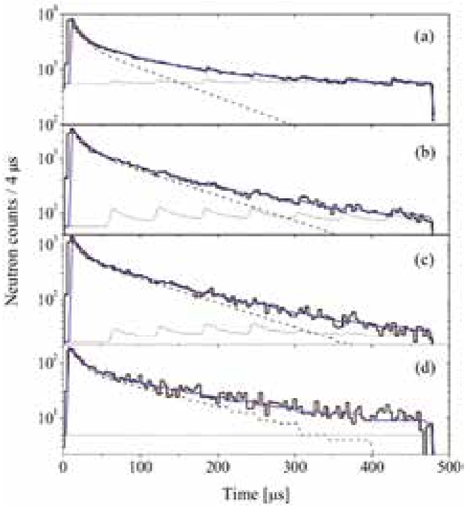

Fig.3 Neutron moderation time spectra of (a) single, (b) double, (c) triple, and (d) quadruple neutron events generated in ^{209}Bi(γ, xn) reactions induced by 42.2 MeV maximum energy LCS γ-rays. The experimental time spectra (solid black) are displayed along with the corresponding best fit (solid blue). The fit functions for reaction neutrons (dashed) produced by the main γ-ray bunches and the background (dotted) contributions are displayed separately.

spectra. Figure 3 shows examples of neutron time moderation spectra for single, double, triple, and quadruple events, respectively. The direct neutron multiplicity sorting technique described in Ref. [4] was applied to obtain the number of ^{209}Bi(γ, xn) reactions with x = 1–4.

The monochromatic cross sections were corrected by taking into consideration the probability of multiple firing events, in which more than one photon from the same LCS γ-ray beam bunch induces photoneutron reactions in the target. The corrections are necessary where there is a considerable difference between the cross sections of competitive reaction channels.

An energy unfolding procedure has been performed on the monochromatic cross sections. For each irradiation point, the average path length through the target per incident photon has been constructed using Geant4 simulations, in which the energy spectra of the LCS γ-ray beams and the physical dimensions of the irradiated targets are given as input. The unfolding procedure consists in iteratively adjusting a test cross section until the folding between it and the incident photon spectrum reproduces the monochromatic cross sections.

The partial ^{209}Bi(γ, xn) with x=1-4 cross sections are compared in Figure 4 with statistical model calculations performed with the EMPIRE code. The GDR component was calculated by a standard Lorentzian (SLO) model as well as by a Simplified version of the modified Lorentzian (SMLO) approach. We represented both the exclusive (γ,xn) channels and the inclusive (γ,xn)+ (γ,xnp)+ (γ,xna)+… ones. The present ^{209}Bi(γ, tot) cross sections obtained as the sum of the partial cross sections are displayed in Fig. 5 along with existing experimental results and evaluations and EMPIRE calculations.

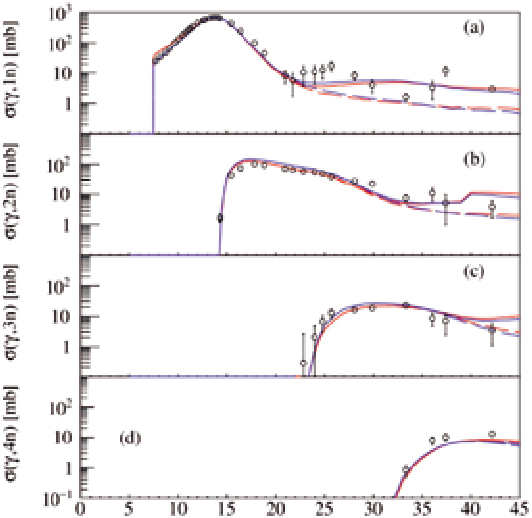

Fig.4 Present results of ^{209}Bi(γ,xn) with x=1-4 cross sections compared with statistical model calculations performed with the SLO (red curves) and SMLO (blue curves) gamma strength functions.

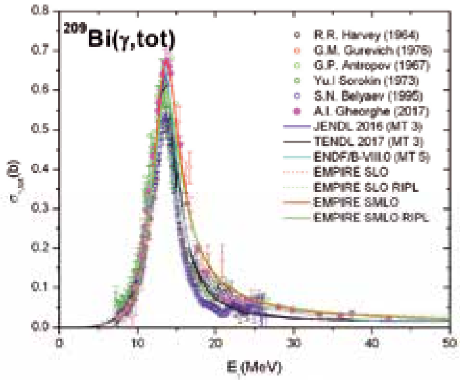

Fig.5 Present results of ^{209}Bi(γ,tot) cross sections compared existing experimental results and evaluations and EMPIRE calculations.

References

[1] IAEA Coordinated Research Project on Photonuclear Data and Photon Strength Functions, https://www-nds.iaea.org/CRP-photonuclear/.

[2] B. S. Ishkhanov *et al.*, Phys. At. Nucl. **67**, 1664 (2004).

[3] I. Gheorghe *et al.*, Phys. Rev. C **96**, 044604 (2017).

[4] H. Utsunomiya *et al.*, Nucl. Instrum. Methods A **871**, 135 (2017).

Development of positron annihilation apparatus for defects study in bulk materials using BL01 gamma ray

K. Sugita[1], S. Miyamoto[2], M. Terasawa[2], F. Hori[1]
[1]Osaka Prefecture University, [2] LASTI, University of Hyogo

Abstract

We have developed a new positron annihilation apparatus as direct implantation of Laser Compton scattering (LCS) gamma rays, which are derived at NewSUBARU beam line BL01, into bulk materials. By using this method, we have measured positron annihilation Doppler broadening spectra of bulk silicon and bulk iron before and after electron irradiation. LCS gamma ray maximum energy of 16.9 MeV using by Nd:YVO$_4$ laser and 982 MeV electron are injected directly into samples, caused pair creation and annihilation gamma ray emission in the samples. Positron annihilation gamma rays as the energy spectra were detected by HP-Ge detector. Doppler broadening spectra measured by this method is consistent with other measurement results of positron annihilation by using ^{22}Na radioactive source.

Introduction

Positron annihilation methods are used defect study in materials widely. Positron source usually use for defects research is mainly radioisotope (RI). Positron from RI are not mono-energetic and about several hundred keV in maximum so that it can be estimated only near surface in materials. In order to detect defects in mm depth of bulk materials with nondestructive, more than MeV ordered positron is needed. Therefore, we have constructed a new positron apparatus using high energetic positron created via pair creation from Laser Compton scattering (LCS) gamma rays at BL01 [1-2]. The energy of LCS gamma rays at this beam line is extremely high and controllable. We have now developing a new positron measurement system by using this LCS gamma ray. That is, both the pair creation and annihilation take place in the sample by implantation of this gamma ray into a sample directly. Detected annihilation gamma ray is analyzed the energy distribution of positron annihilation Doppler broadening. In this report, the measurement result of some different materials by this positron annihilation method are demonstrated.

Positron annihilation apparatus setup

Figure 1 shows the system of LCS gamma source at BL01. LCS gamma ray irradiated and positron annihilation experiment in hutch-2 GACKO. LCS gamma ray is produced by scattering between laser photon and circling electron in storage ring. Energy of LCS gamma ray is determination laser wavelength and electron energy [3]. Injection laser photon and circling electron is head on collision in Figure 1. Generated gamma ray passes through the vacuum duct and two lead collimators T and H, and finally reaches the optical hutch-2 GACKO. LCS gamma ray with maximum energy of 16.9 MeV generated from Nd:YVO$_4$ laser ($\lambda = 1064\,nm$) and circulated electron with the energy of 982 MeV. In this case, diameter of 6 mm two Pb collimators were used, therefore, LCS gamma ray minimum energy was 15.2 MeV at the BL01 setup. LCS gamma ray is implanted into a sample and annihilation gamma rays are detected in hutch-2. Figure 2 shows the schematic setup the positron creation and annihilation in sample system. Annihilation gamma rays detected by HP-Ge detector which is covered by Pb blocks. This gamma ray with

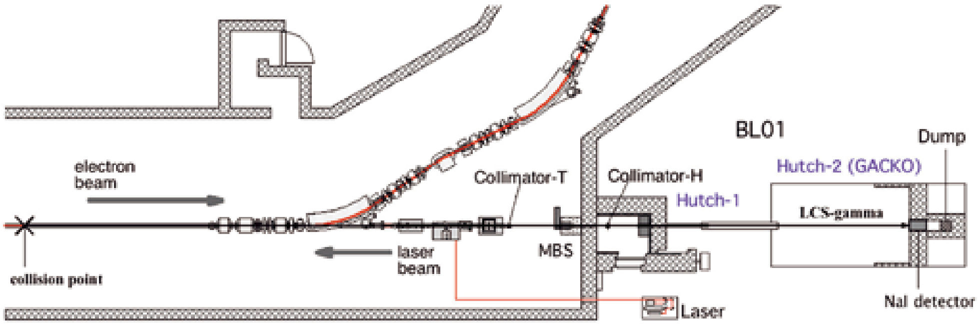

Fig.1 LCS gamma ray system at NewSUBRU BL01.

this energy is high enough to transmit mm thickness bulk samples as shown in figure 3. This figure shows that simulation of gamma tracks and created positron tracks by implantation of 16.9 MeV LCS gamma ray into iron calculated by PHITS code version 3.02 based on the Monte Carlo simulation [4]. As can be seen in this figure, positrons are created homogeneously on gamma ray tracks.

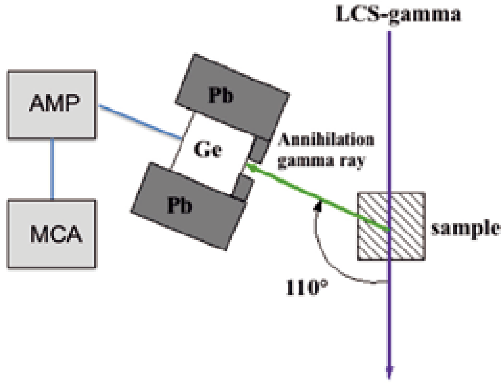

Fig2. Schematic illustration of positron creation and annihilation by direct LCS gamma ray implantation apparatus.

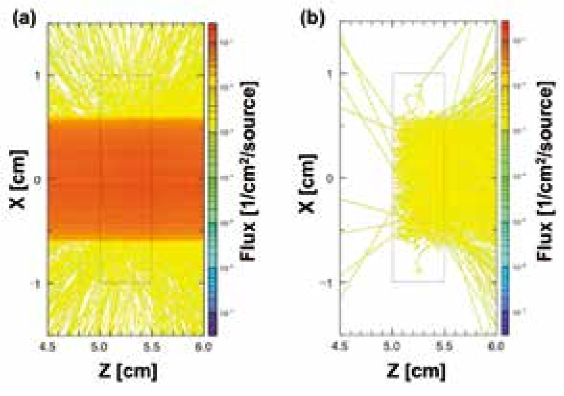

Fig3. Simulation of 16.9 MeV LCS gamma ray implantation into Fe calculated by PHITS code. (a) gamma ray tracks in iron and (b) created positrons.

Measurement

We have measured Doppler broadening spectra for pure silicon, pure iron and 8 MeV electron irradiated iron by this positron annihilation system. Table 1 shows the size of all samples. Pure samples are well annealed, and electron irradiation have performed by linear accelerator at Kyoto University Reactor Research Institute with fluence of 1 x 10^{18}/cm^2. In this case, electron irradiation introduces vacancy type defects with about 100 at.ppm into iron. However, an electron irradiated iron sample is thinner than non-irradiated one, then piled it on a non-irradiated iron plate was measured as irradiated sample. Positron creation and annihilation takes place on the gamma tracks homogeneously, hence observed positron parameters show average information in a whole sample. Figure 4 shows positron annihilation Doppler spectra in all samples. The spectra for Si and Fe show different peak height depending on their different electron distribution in these samples. Peak height of positron annihilation Doppler profile in Si is higher than in Fe, which is consistent with the results of general positron annihilation measurement for Si and Fe by using ^{22}Na as a positron source. On the other hand, it seems slight difference between iron samples before and after electron irradiation. This is because the average of positron annihilation events in an irradiated and non-irradiated iron plates. Table 2 shows S parameters of these samples. In this figure, S parameter for irradiated sample is larger than that for non-irradiated one. This result shows that extremely low concentration of vacancy type defects introduced by electron irradiation was successfully detected by this method.

Table 1. Sample conditions.

Sample	size
pure Fe (4N)	20mm x 50 mm x 5mm
electron irradiated Fe (8MeV, 1 x 10^{18}/cm^2) + pure Fe (4N)	20mm x 50 mm x 2mm + 20mm x 50 mm x 3mm
Si (Cz-Si)	20mm x 45mm x 16.5mm

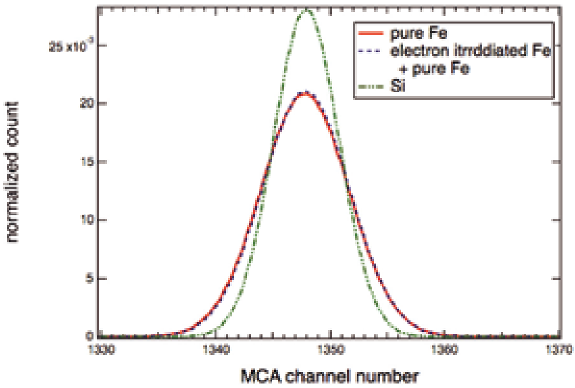

Fig4. Positron Doppler profiles in all samples.

Table 2. S parameter of sample.

Sample	S parameter
pure Fe	0.566
electron irradiated Fe+ pure Fe	0.571

Reference

[1] F. Hori *et al.*, Jpn. J. Appl. Phys. conf. proc.2 011301 (2014).

[2] F. Hori *et al.*, J. Phys. conf. Ser. **674** (2016) 012025.

[3] C. Sun and Y. K. Wu., Phys. Rev. ST Accel. Beams **14**, 044701(2011).

[4] Tatsuhiko Sato *et al.,* J. Nucl. Sci. Tecnol. **55**, 684-690(2018).

Measurement of deflection on germanium and gold prisms using 1.7 MeV laser Compton scattering γ-rays

T. Kawasaki[1], S. Naito[1], Y. Sano[1], T. Hayakawa[2], T. Shizuma[2], R. Hajima[2], and S. Miyamoto[3]
[1]Toshiba Corporation, [2] National Institutes for Quantum and Radiological Science and Technology,
[3] University of Hyogo

Abstract

The refractive indexes δ of Ge and Au prisms for γ-rays at 1.7 MeV were measured to explore if there are refractive index enhancements to 6th power of atomic number due to high order nonlinear process of Delbrück scattering by using Laser Compton scattering (LCS) γ-rays at BL01, NewSUBARU. The measured upper limit of δ for crystal Ge, crystal Au or polycrystal Au prisms are 4.0×10^{-8}, 2.9×10^{-7}, or 2.4×10^{-7}, respectively. This result does not support the hypothesis of the higher order Delbrück scattering suggested by Habs et al. [Phys. Rev. Lett. **108**, 184802 (2012)].

Introduction

The refractive index $|\delta(E\gamma)|$ following Snell's law is given by $n(E\gamma) = 1+\delta(E\gamma)+i\beta(E\gamma)$, where $E\gamma$, δ, and β are photon energy, phase shift affecting light deflection, and extinction coefficient affecting light absorption, respectively. Typically, $|\delta(E\gamma)|$ in an energy region above 1 MeV should be less than the order of 10^{-10}

On the other hand, Habs et al. found that the refraction index δ of a silicon prism was on the order of 10^{-9} which is higher than the predicted value by an order of magnitude at energies above 0.7 MeV [1]. They presented that the enhancement can be explained by higher order terms of Delbrück scattering with Z^4 and Z^6 dependence, where Z is atomic number. According to this hypothesis, the refraction of γ-rays has a strong dependence of the atomic number Z and the δ becomes approximately 10^{-5} at $Z = 79$ (Au). This value would be possible to make refractive optics for γ-rays in the MeV energy region, which would enable new experimental techniques for nuclear physics [2] and γ-ray astronomy [3].

In this experiment, we measured the refractive index of Ge (Z=32) and Au (Z=79) prisms using imaging plates (IP) with 1.7 MeV LCS γ-ray beams at the BL01 beam line in the NewSUBARU [4].

Experimental Procedure

Figure 1 shows experimental setup at BL01. The γ-ray beam was generated by Compton scattering of 1 GeV electrons and 10.6 µm CO_2 laser beams at the collision point [5]. The prisms were located inside the first experiment room, whereas the IP and NaI(Tl) detector were set inside the second experiment room. The approximate distance from the collision point to the prisms and from the prisms to the IP were 10 m and 8m, respectively. The peak energy of the γ-ray beam measured by NaI(Tl) detector was 1.7 MeV.

$\delta(E\gamma)$ was evaluated from the displacement of a γ-ray beam passing through the prisms by measuring the γ-ray distribution with the IP*. An IP reader (BAS-2500, FUJIFILM)* with a spatial resolution of 50 µm was used as a reader.

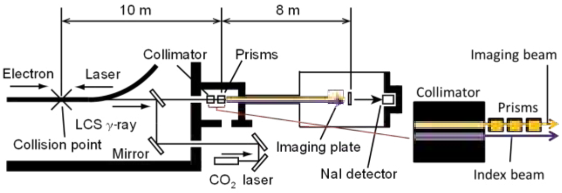

Fig.1 Experimental setup at BL01

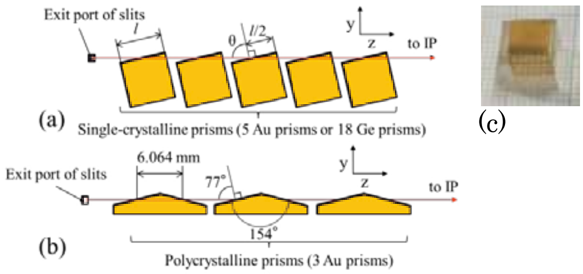

Fig. 2 Shape of prisms. (a) Au and Ge single crystalline-prism. The lengths l and angles θ of Au (Ge) prims are 6 mm and 77° (12 mm and 83.5°), respectively. (b) Au polycrystalline prism (c) Au single-crystalline prism.

In principle, the cross section of the Delbrück scattering depends on the angle of scattering plane and polarization [6]. Therefore, to investigate the correlation between δ and linear polarization plane angles, we used p- and s-polarized γ-rays for the Au single-crystalline prisms. The evaluated linearity of the γ-rays polarization from that of the CO_2 laser was 99.5%. In addition, we also used unpolarized beams to compare with the previous experiment [1] measured by using unpolarized γ-ray generated by neutron capture reactions.

In this experiment, we chose Au (Z=79) and Ge (Z=32) as prism materials that have Z larger than that of Si measured by Habs et al. [1]. The large Z

---

* Product names mentioned herein may be trademarks of their respective companies.

of Au should produce a large effect on δ, due to the Z^6 dependence. The Ge crystal has diamond structure as same as that of Si. In term of Z and crystalline, we fabricated three types of prisms with mirror finish surface: Au single-crystalline prisms, Au polycrystalline prisms, and Ge single-crystalline prisms as shown in Fig. 2. The Au single-crystalline prisms were a cube 6 mm on a side and were tilted at an angle of 77° to the γ-ray beam axis. The Au polycrystalline prisms were pentagonal and both the incident and output angles were 77° to the γ-ray axis. The Ge crystal prisms were a cube 12 mm on a side and were tilted at an angle of 83.5° to the γ-ray axis. The γ-ray beam entered the vertical center of the each prism's planes.

To increase the small deflection angle, 18 Ge single-crystalline prisms, 5 Au single-crystalline prisms, or 3 Au polycrystalline prisms were arranged. From the previous study [1], δ of Si (Z=14) was 10^{-9} for 1.7 MeV γ-rays. Therefore, if this enhanced δ is dominated by the term proportional to Z^6, the expected refractive index for Ge (Z=32) δ_{Ge} and for Au (Z=79) δ_{Au} are $(32/14)^6\times10^{-9} = 1.4\times10^{-7}$ and $(79/14)^6\times10^{-9} = 3.2\times10^{-5}$, respectively. According to these value and Snell's law, the expected displacement between the incident and the deflected γ-ray beam on the IP for the Ge single crystals, Au single crystals, or Au polycrystalline prisms should be 1.6×10^2 μm, 5.9×10^3 μm, or 6.7×10^3 μm, respectively.

As shown in Fig 1, the collimator has two slits with height of 0.5 mm and width of 2 mm that were horizontally arranged at 1 mm interval. One of the two beams separated by the collimator passes through a prism set and subsequently irradiated the IP, whereas the other beam directly irradiated the IP without passing through prisms to be used as an index beam to estimate relative displacement. To obtain the image of the only LCS γ-rays, we also subtracted the IP image of only bremsstrahlung x-ray obtained with the CO_2 laser-off from the image with the CO_2 laser-on.

RESULT AND DISCUSSION

Figure 3 shows measured image of γ-rays. The intensity was integrated along x- axis to estimate the distribution and displacement along y-axis.

Figure 4 shows the experimental results and the results calculated by "EGS5" [7]. The calculattion does not include the Delbrück scattering. However, the vertical peak position of each measurement result is not different from the corresponding calculated result within 50 μm error. According to this resolution of 50 μm, the upper limits of the refractive index of δ_{Ge}, $\delta_{Au,single}$, and $\delta_{Au,poly}$ are 4.0×10^{-8}, 2.9×10^{-7}, and 2.4×10^{-7}, respectively. These upper limits are 1-2 orders of magnitude lower than the expected values if the Z^6 dependence exists. Significant difference between the upper limits of single-crystalline and polycrystalline prisms for Au are also not observed. In addition, there is no difference among unpolarized, p-polarized, and s-polarized γ-rays. In this way, we cannot find any signature for the enhancement proportional to Z^6.

CONCLUSION

In order to explore a strong Z dependence of refractive index proportional to Z^6, which may originate from the nonlinear effect in Delbrück scattering, we measured the displacement at 8 m downstream of Au or Ge prisms for 1.7 MeV LCS γ-rays. The measured upper limits of the refractive index of $\delta_{Ge,}$ $\delta_{Au,single}$, and $\delta_{Au,poly}$ are 4.0×10^{-8}, 2.9×10^{-7}, and 2.4×10^{-7}, respectively. However, we could not find any evidence that such process occurs, which can contribute to realize the optical device for γ-rays in the MeV energy region. This result does not support the hypothesis suggested by Habs et al. [1]. Because we investigated only the Z^6 dependence in the present study, the reason for the δ enhancement [1] has remained an open question.

Acknowledgements

This work was supported by JSPS KAKENHI Grant Number 15H03665.

References

[1] D. Habs *et al.*, Phys. Rev. Lett. **108**, 184802 (2012).
[2] P.G. Thirolf *et al.*, EPJ Web of Conferences **38** 08001 (2012).
[3] B. C. Lacki *et al.*, Astrophys. J. **786**, 40 (2014).
[4] T. Kawasaki *et al.,* Phys. Lett. B. **381**, 3129 (2017).
[5] S. Amano *et al.*, Nucl. Instrum. Methods Phys. Res., Sect. A **602**, 337 (2009).
[6] J. K. Koga, and T. Hayakawa, Phys. Rev. Lett. **118**, 204801 (2017).
[7] H. Hirayama *et al.*, SLAC Report number: SLAC-R-730(2004)

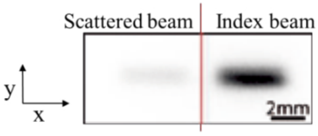

Fig. 3 γ-rays measured by IP

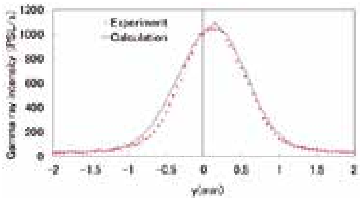

Fig. 4 Experimental result of Au single crystalline prism with p-polarized γ-rays

XAFS Measurements in the Soft X-ray Region around 1 keV in BL05A

T. Hasegawa[1, 2, 3], S. Fukushima[1, 2, 3] and K. Kanda[3]
1 Synchrotron Analysis L.L.C., 3-2-24 Wadamiya-dori, Hyogo-ku, Kobe-shi, Hyogo 652-0863 Japan
2 Kobe Material Testing Laboratory Co., Ltd., 47-13 Niijima, Harima-cho, Kako-gun, Hyogo 675-0155 Japan
3 LASTI, University of Hyogo, 3-1-2 Koto Kamigori-cho, Ako-gun, Hyogo 678-1205 Japan

Abstract

BL05A is a unique double crystal monochromator (DCM) beamline of NewSUBARU and is used for X-ray absorption fine structure (XAFS) spectroscopy. We have applied the DCM that consists of crystals of Beryl and KTP to cover the X-ray energy range lower than that of the InSb crystal. Furthermore, we have successfully improved efficiency of X-ray transmission by using a beryllium filter with thickness 25 μm in this energy region. Consequently, this setup has enabled practical analysis in the soft X-ray region around 1 keV. In addition, we conducted the evaluation of the radiation damage of the KTP crystal and confirmed that the intensity of Bragg reflection was decreased.

Introduction

X-ray absorption fine structure (XAFS) spectroscopy has been used as a powerful tool for analyzing the chemical state and the characterization of materials. Especially, XAFS analysis in the soft X-ray region around 1 keV is important to industrial utilization because *K* absorption edges of light elements such as sodium, magnesium, aluminum can be analyzed. BL05, beamline of NewSUBARU, was constructed on 2008 to respond needs for XAFS of X-ray region arising from various industries [1, 2]. BL05A, a branch line of BL05, is equipped with a double crystal monochromator (DCM) that can provide the photon in the region up to 4000 eV. XAFS measurements over the *K* absorption edge energy regions of silicon (more than about 1800 eV) have been commonly carried out by a crystal monochromator with InSb (111) crystal. In the lower-energy region than the *K* absorption edges of silicon, Beryl and KTP crystals are often used for XAFS measurements. However, it is well known that these crystals are likely to be affected by radiation damage caused by synchrotron light. In this paper, we report on the radiation damage of the KTP crystal of BL05A by synchrotron light.

1. XAFS measurements in the soft X-ray region around 1keV

There are high demands on XAFS analysis in the soft X-ray region 1 keV for industrial users. Therefore, we have tried improvement of the beryllium filter in BL05A to improve the X-ray transmission in the energy region. The filter is used to separate the ultra-high vacuum in the storage ring with the front-end from the high vacuum in the beamline. We succeeded to make the filter of thickness from 45 μm down to 25 μm[3, 4, 5]. In addition, in order to cover the lower-energy region than the Si *K*-edge, the DCM was equipped with pairs of crystals in 2014, Beryl (10$\bar{1}$0) and KTP (011). As a result, XAFS measurements around 1keV such as sodium, magnesium and aluminum became possible. A comparison of the measured magnesium *K*-edge XANES spectra by Beryl crystal and KTP crystal is shown in Fig.1. The sample was measured with the partial fluorescence yield mode. If X-rays of a constant energy are diffracted at the higher Bragg angle (in other words, the smaller the crystal lattice spacing), higher energy resolution can be obtained. This effect can be confirmed from the

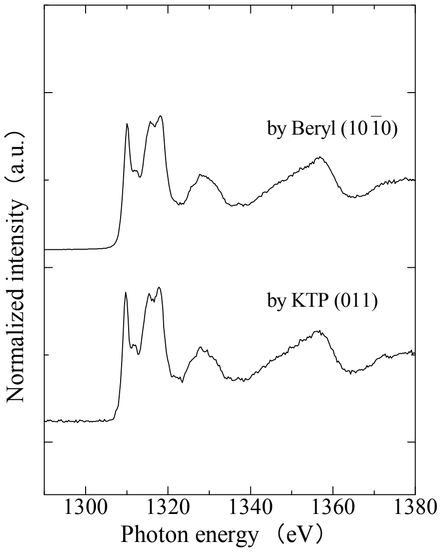

Fig.1 Mg *K*-edge XANES spectra of MgO powder.

fact that the resolution of the spectrum gained by KTP crystal is slightly higher than that gained by Beryl crystal as shown in Fig.1.

2. Evaluation of the radiation damage of the KTP crystal

Beryl crystals are often used for the XAFS measurements of sodium and magnesium. On the other hand, KTP crystals are used for aluminum. These crystals (in particular, KTP crystals) are susceptible to damage caused by synchrotron light. This may be attributed to their insufficient heat resistance. For the reason, high sensitive XAFS measurements for these light elements are generally very difficult in the synchrotron radiation facility with the high energy synchrotron light source. It is necessary to cool the crystals in order to reduce the thermal loading of the crystals. Because thermal expansion of crystals leads to a lattice strain in crystals and a difference in lattice spacing between first crystal and second crystal by X-ray irradiation, which account for the degradation of reflection efficiency of exit-beam. In BL05A, the plate equipped with the first crystals is maintained at a precisely-controlled temperature with accuracy of 22.0 +/- 0.1 degrees Celsius by a water-cooling system. In addition, these crystals are weakly adhered to a nickel coating copper plate with gallium-indium (GaIn) alloys to minimize thermal expansion. The transition of intensity of diffracted light on KTP crystals is shown in Fig.2. We considered the current measured by using an electrometer connected to the reference electrode (Ni mesh) as the intensity of Bragg reflection. Despite the sufficient cooling of the first crystals, the decrease in the current was observed. It is presumed that the decrease was caused by radiation damage. Furthermore, we measured the aluminum *K*-edge spectra of α-Al_2O_3 powder to investigate the effect of the radiation damage on the energy resolution of XAFS spectra (Fig.3). It is confirmed that no degradation of the energy resolution was observed in XAFS spectra while the current of the reference electrode was decreased.

References

[1] T. Hasegawa *et al.*, *Advances in X-ray Chem. Anal. Jpn.*, **41**, pp.99-106 (2010) [in Japanese].

[2] K. Kanda *et al.*, *J. Phys.: Conf. Ser.*, **425**, 132005/1-4 (2013).

[3] T. Hasegawa *et al.*, *LASTI Annual Report*, **vol.16**, pp.73-74 (2014).

[4] T. Hasegawa *et al.*, *LASTI Annual Report*, **vol.17**, pp.16-17 (2015).

[5] T. Hasegawa *et al.*, *LASTI Annual Report*, **vol.18**, pp.37-38 (2016).

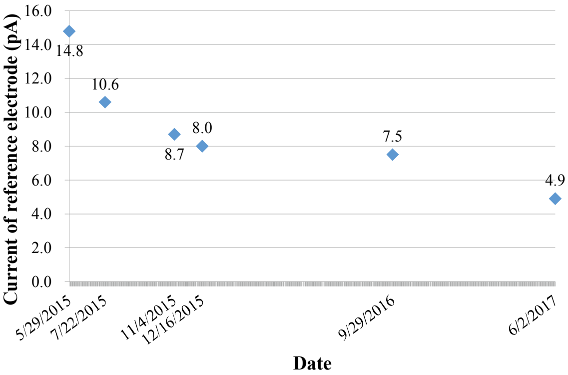

Fig.2 Relationship between variation with time and intensity of radiation light diffracted by KTP crystal. (Incident X-ray energy: 1400 eV).

(a)

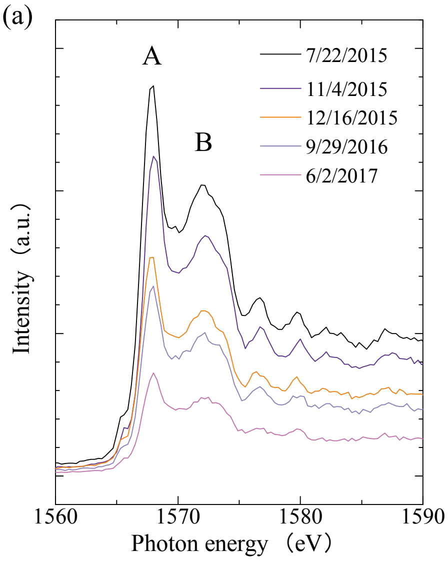

(b)

Date	FWHM (eV)	
	A	B
7/22/2015	1.64	8.14
11/4/2015	1.65	8.07
12/16/2015	1.63	8.26
9/29/2016	1.63	8.14
6/2/2017	1.65	8.47

Fig.3 Al *K*-edge XANES spectra of α-Al_2O_3 powder (a) and full width at half maximum (FWHM) as the photon energy resolution (b).

Soft X-ray irradiation effect on the hydrogenated Si containing DLC films

Kazuhiro Kanda[1*], Shotaro Tanaka[1], Ryo Imai[1], Shuto Suzuki[1], Takayuki Hasegawa[1,2], Tsuneo Suzuki[3],
Keiji Komatsu[4], and Hidetoshi Saitoh[4]
[1] Laboratory of Advanced Science and Technology for Industry, University of Hyogo, Kamigori, Hyogo, Japan
[2] Synchrotron Analysis L. L. C., Kamigori, Hyogo, Japan
[3] Extreme Energy-Density Research Institute, Nagaoka University of Technology, Nagaoka Niigata, Japan
[4] Department of Materials Science and Technology, Nagaoka University of Technology, Nagaoka Niigata, Japan

Abstract

The effect of soft X-ray irradiation on hydrogenated silicon-containing diamond-like carbon (Si-DLC) films, which were expected to use as lubricant material in outer space, was investigated using synchrotron radiation (SR). We found that the volume of hydrogenated Si-DLC films decreased by the SR exposure. This decrease in volume was attributable to desorption of hydrogen, and composition ratios of other elements hardly change by SR exposure. The local structure of carbon atoms in the hydrogenated Si-DLC film changed remarkably by SR exposure, on the other hand, that of silicon atom hardly changed.

1. Introduction

Diamond like carbon (DLC) is amorphous carbon film, and that has excellent properties, such as high hardness, a low friction coefficient, high abrasion quality, a gas barrier, chemical inertness and surface lubrication. Therefore DLC films are utilized as many industrial fields, for instance, automobile parts, hard disks, implant parts and food containers.

Recently, utilization of DLC films as solid lubricant for satellite is examined. Actuator of satellite is necessary to use lubricant, however, oil used in terrestrial cannot be used in outer space because it freezes in vacuum. Thus, DLC films expected to be used as lubrication instead of oil. Especially, higher hydrogenated DLC (H-DLC) films, which contain hydrogen more than 40 %, maintain low friction in vacuum, and are expected for solid lubricant in outer space, where is known for its unique hard environment, such as, soft X-ray, atomic oxygen and so on. Therefore, materials used in outer space are required the durable against space environment. However, the degradation of H-DLC film was reported to be caused by atomic oxygen exposure. We found that H-DLC films, which contained Si atom, had the durability against the irradiation of atomic oxygen. Soft X-rays is another important environment in outer space. Therefore, clarification of the effect of soft X-ray exposure on DLC films is important to ensure that DLC films are used in outer space safety.

In this study, modification of hydrogenated Si-DLC films by the exposure to soft X-ray was investigated. SR dose dependence on film volume change, elements contents of surface and bulk, integrated state of surface of C and Si, were measured.

2. Experimental

Hydrogenated Si-DLC film was deposited on Si wafer using an amplitude-modulated radio-frequency plasma-enhanced chemical vapour deposition method (Nippon ITF Co.). This method enables the deposition of DLC films containing a lot of hydrogen. Film thickness of as-deposited hydrogenated Si-DLC film was estimated to 522 nm from observation of section image using a scanning electron microscope (JEOL JSM-6700F).

The soft X-ray irradiation of hydrogenated Si-DLC films was carried out at BL06. The SR was irradiated onto the film surface perpendicularly. The SR at the BL06 sample stage had a continuous spectrum from the infrared to soft X-ray region less than 1 keV. This energy range includes 110 eV and 300 eV, which are the ionization energies of a silicon *L* shell and a carbon *K* shell, respectively. During the experiment, the electron energy of the NewSUBARU ring was 1.0 GeV and the ring current was 300 mA in the top-up mode. The SR dose [mA·h] was derived as the product of the ring current [mA] and the exposure time [h]. During the exposure of the hydrogenated Si-DLC films to soft X-rays, the pressure in the irradiation chamber was on the order of 10^{-5} Pa and the temperature of the sample stage was confirmed to be room temperature using a thermocouple. After the SR exposure, the modified Si-DLC films were stored in a dry box.

3. Results and Discussion

To investigate the soft X-ray irradiation effect on the hydrogenated Si-DLC films, we exposed such films to synchrotron radiation (SR) in the soft X ray region in the dose region from 0 to 2000 mA·h and measured the degree to which the films' properties depended on the SR dose.

3.1 Film thickness by stylus profiler and scanning electron microscope

To estimate the degree to which hydrogenated Si-DLC film thickness depended on the SR dose, the hydrogenated Si-DLC films were exposed to SR through an Au mesh (wire diameter φ 0.07 mm, 100 mesh/inch) as a mask. The step depth was estimated by using a stylus profiler (DEKTAK 6M) to measure the difference in altitude between the area exposed to SR and a shadow area due to the Au mesh. For the support to taking step depth measurements, we observed section images of the hydrogenated Si-DLC film, which were a film as deposition and films after SR irradiation with SR doses of 800 mA·h and 2000 mA·h, by using an SEM (JEOL JSM-6700F).

Figure 1 shows the degree to which the soft X-ray irradiation caused the film thickness to be dependent on the SR dose. The open and closed circles respectively show the variation of film thicknesses estimated from measurements using SEM and a stylus profiler. Variation on film thicknesses estimated from stylus profiler measurements accorded well with those estimated from SEM measurements. The variation on thicknesses increased gradually to about 60 nm after 2000-mA·h SR exposure. At doses of more than 2000 mA·h, the variation on thicknesses remained constant at 70 nm. From these results, we confirmed that the hydrogenated Si-DLC film thicknesses decreased due to soft X-ray irradiation, but that the increase was stopped at doses of 2000 mA·h or more.

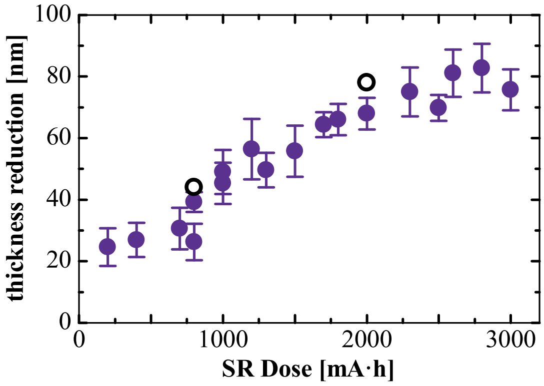

Fig. 1 Thickness reduction dependence of hydrogenated Si-DLC film bulk on SR dose. Open circles and closed circles were estimated from SEM and profiler, respectively.

3.2 Elemental composition in the hydrogenated Si-DLC film obtained by combining of elastic recoil detection analysis and Rutherford backscattering spectrometry

We combined ERDA and RBS to estimate the elemental compositions of hydrogenated Si-DLC films, using an electrostatic accelerator (Nisshin High Voltage, NT-1700HS) located at Extreme Energy-Density Research Institute, Nagaoka University of Technology. He^+ ion accelerated to 2.5 MeV using a tandem Pelletron accelerator were used as the incident beam, whose angle with respect to the surface normal was 72 degrees. At RBS experiments, recoiled He^+ ion was detected by solid state detector (SSD), whose angle with respect to the surface normal was 78 degrees. At ERDA experiments, hydrogen atom scattered by He^+ ion was detected by another SSD, whose angle with respect to the surface normal was 12 degrees.

Figure 2 shows the dose dependence of the hydrogen and silicon composition ratios in hydrogenated Si-DLC films. The atomic ratios of hydrogen and silicon were ≈0.4 and ≈0.2 before the SR irradiation and they were not changed after SR exposure. This result means that desorption of hydrogen in hydrogenated DLC was suppressed due to silicon doping.

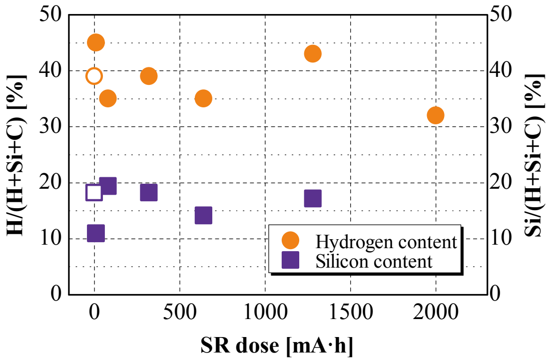

Fig. 2 Elemental composition ratio dependence on hydrogenated Si-DLC film bulk on SR dose, estimated by combining ERDA and RBS. Circles and squares respectively indicate hydrogen and silicon ratios. Open circle and square indicate hydrogen and silicon ratios before the SR irradiation.

3.3 Elemental composition and chemical state of hydrogenated Si-DLC film surface by X-ray photoelectron spectroscopy

We estimated elemental composition of the hydrogenated Si-DLC film surface by using a conventional X-ray photoelectron spectroscopy (XPS) apparatus (Shimadzu, ESCA-1000). The Mg Kα line (1253.6 eV) was used as the X-ray source and incident angle was 45 degrees.

Figure 3 shows the dose dependence of the atomic composition of the hydrogenated Si-DLC film surface. The circles, squares, and triangles respectively show carbon, silicon and oxygen contents. The carbon, silicon and oxygen contents in the hydrogenated Si-DLC film surface before irradiation were ≈0.4, ≈0.4 and ≈0.2, respectively. The atomic composition of the hydrogenated Si-DLC film surface was not changed after SR exposure. On the other hand, it was necessary to note that hydrogen content was not included in this XPS result.

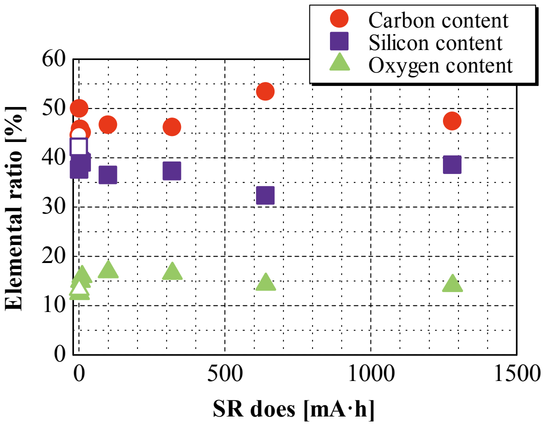

Fig. 3 Elemental ratio of hydrogenated Si-DLC film surface dependence on SR dose with XPS. Circles, squares, and triangles respectively show carbon, silicon and oxygen contents. Open circle, square, and triangle indicate carbon, silicon and oxygen contents before the SR irradiation.

3.4 Local structure of carbon and silicon atoms in the hydrogenated Si-DLC film obtained through near-edge X-ray absorption fine structure measurements

NEXAFS spectroscopy using synchrotron radiation is known to be sensitive to the local structure around the absorber atom. To discuss on variations in the local structure of the hydrogenated Si-DLC film due to the exposure to SR, Si-K edge NEXAFS spectra were measured. The NEXAFS measurement of the Si K absorption was performed at BL05A, which have a bending magnet as light source and a double crystal monochromator. The NEXAFS spectra of the Si K edge absorption were measured in the range 1810-1890 eV using InSb(111). The energy resolution was estimated to be less than 2.0 eV (FWHM). In the NEAXFS measurement, irradiation angle irradiation angle to the sample is the "magic angle" of 54.7° with respect to the surface. The electrons coming from the sample were detected in total electron yield (TEY) mode. The intensity of the incident photon beams (I0) was measured by monitoring the photocurrent from a gold mesh. The absorption signal was given by the ratio between the out-coming electron intensity from the sample, I_s, and I_0.

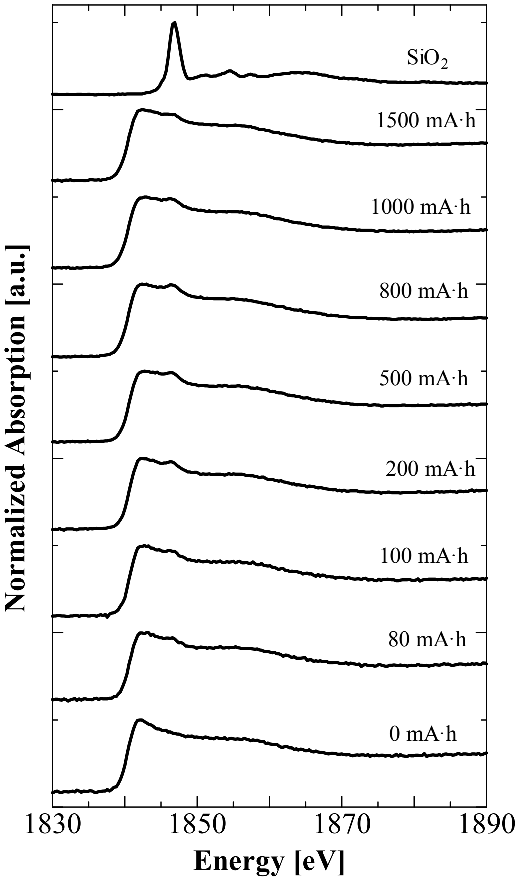

Fig. 4 SR dose dependent Si K-edge NEXAFS spectra of hydrogenated Si-DLC films and those of some reference materials.

Figure 4 shows the Si-K edge NEXAFS spectra of the hydrogenated Si-DLC film irradiated by SR, of the film before irradiation, of some referential materials, SiO_2 powder, Si wafer, β-SiC powder and amorphous hydrogenated silicon (a-Si:H) film. In the spectra of Si wafer and a-Si:H film, the peaks derived from SiO_2 due to native oxidation were observed at 1846.8 eV. The Si atoms in the hydrogenated Si-DLC film can be expected to have Si, C, H, and/or O as a neighboring atom. The chemical environment around the absorbing atom can be evaluated from the positions of the absorption edge and the white line. The edge position of Si K edge shifts to towards higher energy with increasing positive charge on the Si atom. The edge position of hydrogenated Si-DLC film before irradiation was observed to ≈1840 eV, which was located near those of Si wafer and a-Si:H film. White line was observed at about 3 eV above the absorption edge, which resembled those of Si wafer and a-Si:H film. As a result, the chemical environment of Si atom in the hydrogenated Si-DLC film was close to those in the Si wafer and a-Si:H film. After irradiation of SR, the peak of 1846.8 eV, which was derived from SiO_2, was appeared at the NEXAFS spectra of Si-DLC films. The intensity of this peak increased until 800 mA・h dose. However, it decreased in the dose region more than 1000 mA・h dose. On the other hand, the intensity of the energy range about 1843-1846 eV increased. This energy range derived from deoxidization of SiO$_2$. These results mean that SiO$_2$ layer was generated at the surface of hydrogenated Si-DLC film by the oxidation of surface Si atoms with residual oxygen in vacuum chamber due to irradiation of SR. The formed SiO$_2$ layer was deoxidized by the additional exposure to soft X-ray. On the other hand, the positions of the absorption edge and the white line did not varied by the SR exposure. Therefore, the chemical environment of Si atom in the hydrogenated Si-DLC film did not changed by the irradiation of SR.

The C-K edge NEXAFS spectra of the hydrogenated Si-DLC film irradiated by SR have been reported in previous work (K. Kidena et.al., *Trans. Mat. Res. Soc. Japan,* 40, (2015) 353-358). Those were reshowed in Fig. 5, with those of of the film before irradiation, of β-SiC powder and of a commercial DLC film as a typical DLC film. This commercial DLC film was deposited on 200 nm-thick Si wafers using the ion plating method; thus we call it IP-DLC film which consisted of only carbon and hydrogen without silicon and other hetero-elements. The hydrogen content of this IP-DLC film was estimated to be ≈20% from a combination of ERDA and RBS measurements. A sharp π^* peak observed at 285.38 eV is ascribed to the C1s> π^* resonance transition originating from the carbon-carbon double bonding. A broad σ^* peak observed at about 285-310 eV is ascribed to the C1s> σ^* resonance transition. The C K-edge NEXAFS spectra of Si-DLC films were classified as four types with the silicon content. The C K-edge NEXAFS spectra of hydrogenated Si-DLC films before SR irradiation used in the present study was classified to type-3 reported in ref. RP130122. That to say, the σ^* peak was narrower than that of typical DLC film and shifted to lower energy of ≈5 eV, due to influence of peak of 289 eV derived σ^*(C-Si) peak. In addition, the peak intensity of $1s\rightarrow\pi^*$ transition at 285.4 eV was weak. After irradiation of soft X-ray, the spectral features of C K-edge NEXAFS spectra of hydrogenated Si-DLC film greatly varied. The peak intensity of $1s\rightarrow\pi^*$ transition at 285.4 eV increased by the irradiation of 15 mA·h of the SR dose. The σ^* peak became broader and shifted to higher energy. In other words, the C K-edge NEXAFS spectra of hydrogenated Si-DLC films concerted from type-3 to type-1 or 2. As a result, the spectral features of hydrogenated Si-DLC film after SR exposure of more than 320 mA・h resembled that of the typical DLC film, which consisted of only carbon and hydrogen without silicon. Therefore, C-Si bond decreased by soft X-ray exposure at surface of hydrogenated Si-DLC films.

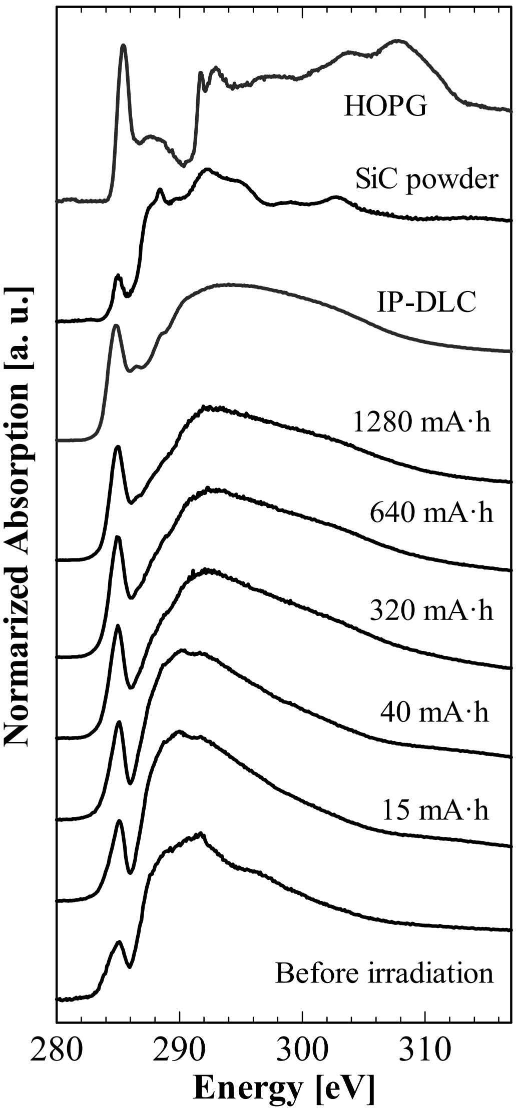

Fig. 5 SR dose dependent C K-edge NEXAFS spectra of hydrogenated Si-DLC films and those of some reference materials.

4. Conclusion

SR dose dependences on several properties of hydrogenated Si-DLC films were investigated. Film volume decreased with increasing of SR dose, which was due to desorption of hydrogen, Chemical states of carbon was changed by the SR exposure, but that of Si was not almost changed.

Refractive-index modifications in SiO_2 Films by Undurator Radiation with a multilayer spectrometer

K. Moriwaki[1], S. Tanaka[1], and K. Kanda[2]
[1]Graduate School of Eng., Kobe Univ., [2]LASTI, Univ. Hyogo

Abstract

Undurator radiation (UR) by the NewSUBARU (BL7A) is used for SiO_2 modifications for future applications of optical devices like waveguides. UR with a multilayer spectrometer is used for the samples irradiation. By a precise analysis, the refractive index is measured with a precision of less than $1x10^{-3}$. The resulted refractive indices indicate relatively flat dependence on the UR peak energy, and show gradual increase by increasing the irradiation dose, especially in lower doses less than 500mAh. Defects generated in the SiO_2 films by the UR irradiation are the most possible reason for the refractive index increases. Optical absorbance increases by the defects in SiO2 films are measured, but correlation between it and the refractive index is not simple.

Introduction

Synchrotron radiation (SR) and undurator radiation (UR) can be used especially for radiation-induced refractive index changes in SiO_2 film or bulk material for optical devices like optical waveguides[1,2)]. The former experiments revealed differences between UR-irradiated samples with and without a spectrometer[2)]. UR is a very useful tool for the materials modifications, because it can select a useful wavelength, and have very high intensity. UR with a multilayer spectrometer would be more useful for the purpose because the most suitable wavelength could be selected without higher order ones. In this report, refractive-index modification effects are investigated further than that in the previous repots[1,2)]. A new approach to obtain more precise refractive index is also tried in the measurement.

Experiments and Results

Thermally grown SiO_2 films (0.5µm thickness) on Si substrates and fused quartz substrates were used for the UR irradiation (BL-7A). UR with the first-peak energy ranging from 80 to 300eV is used with the spectrometer. Irradiated samples were characterized by refractive-index measurements by a reflection spectrophotometry and optical absorption spectroscopy.

Figure 1 shows refractive index changes measured simply on a uniform surface of a SiO_2 film 10 times. The results in Fig 1 means measurement precision of $7x10^{-3}$ in the refractive index values. As more precise values of the refractive index are needed in this study, we measured distribution of the refractive index n and thickness d of the same SiO_2 film on Si 100 times. Figure 2 shows that the product values of measured n and d is very precise in spite of the variation of the measured n in Fig.1. This is because optical measurements basically determine the product of the n and the propagation distance z of the electromagnetic wave (nz is called optical path length), as the wave expression is $\cos(\omega t-\beta nz)$ where ω is angular frequency, t is time, and β is propagation constant. By the results in Fig.2, n can be

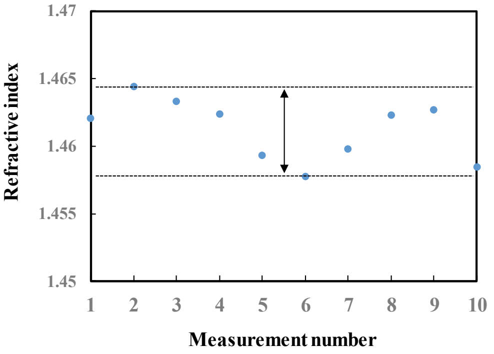

Fig.1 Measurement error of Refractive index in a same SiO_2 film by reflection spectrometry measurements. The arrowed range means the precision of the measurements.

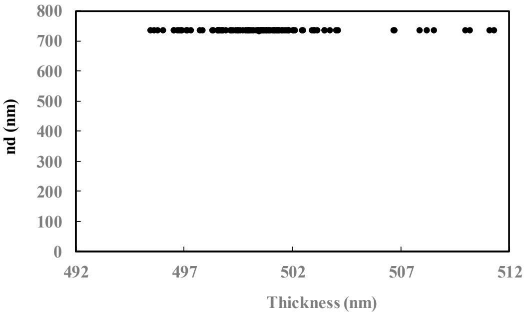

Fig.2 The product of the refractive-index n and the thickness d as a function of d in a same SiO_2 film by 100-times reflection spectrometry measurements.

determined more precisely (1×10^{-3} or less) utilizing the accurate value of thermally grown SiO_2-films thickness (500 nm). In the following part of this report, *n* is determined by this analysis scheme.

Very high refractive index changes after irradiation by UR without the spectrometer were introduced in the samples that are mainly by the surface reduction layer having Si-Si bonds[2)]. By using monochromatic irradiation with a multilayer film spectrometer, Si-Si bonds are not found, so that the refractive index rises were not as high as those without the spectrometer[2)]. In this report, the photon peak-energy dependence on the refractive index is shown in Fig.3. The refractive indices in Fig.3 have no clear peak, though they might be relatively higher at around lower peak energies. The reproducibility in Fig3 is not enough at the present experiments. Further experiments will by necessary because of their importance. On the other hand, the refractive indices as a function of irradiation dose shows a clear dependence on the dose as shown in Fig4. In the previous experiments[2)], lower dose region less than 500mAh were not characterized. By the data in Fig.4, the refractive index is found to rise gradually by increasing the irradiation dose.

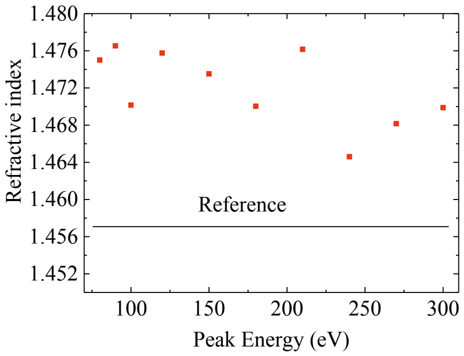

Fig.3 Refractive index changes at λ=633nm in SiO_2 films after irradiation by UR with the spectrometer as a function of peak energy.

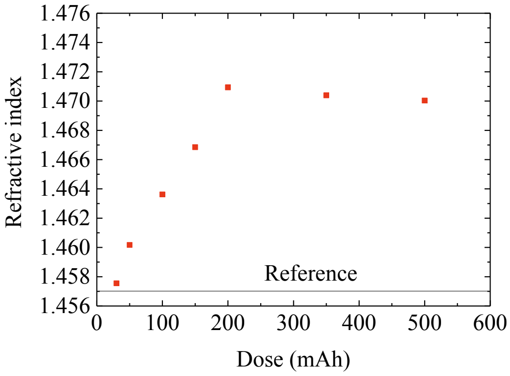

Fig.4 Refractive index changes at λ=633nm in SiO_2 films after irradiation by UR with the spectrometer as a function of dose.

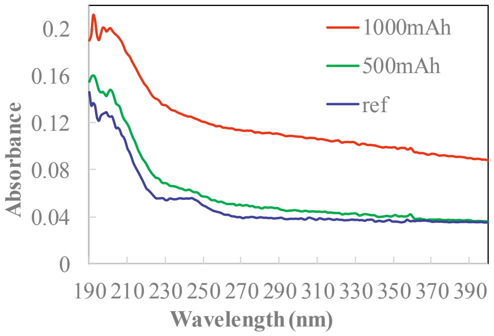

Fig.5 Optical absorbance for samples (dose of 500 and 1000 mAh) irradiated by UR with the spectrometer. The peak photon energy is 240 eV.

Although the reason of the refractive index increase by the irradiation is not clear enough, irradiation defects in SiO_2 films would be the main part of the origin. Correlation between the optical absorbance and the refractive index changes was confirmed in the previous report[2)], because defects increase the optical absorbance. Additional results are obtained as shown in Fig.5. By changing the irradiation dose, absorbance increases are also observed. However, the dependence on the dose is not simple as in a case in Fig.4. The mechanism to generate the refractive index increase may not so simple, and further investigation is necessary.

Conclusions

SiO_2 films were irradiated by UR with a spectrometer, and characterized for their refractive index changes. By fixing the SiO_2 film thickness, which is accurately determined as 500nm in the samples, the refractive index change is more precisely analyzed at less than 1×10^{-3}, comparing to the previous results. By using the analysis, refractive index changes were measured, as a function of irradiation dose or photon peak energy. The mechanism to increase the refractive index is not clear and the further investigations are necessary. The authors thank R.Fujiwara for his help in the measurements.

References

[1] K.Moriwaki et al., LASTI Annual Report **17**, 55 (2015).
[2] K.Moriwaki et al., LASTI Annual Report **18**, 43 (2016).

P $L_{2,3}$ Ultra-Soft X-ray Spectra of GaP and InP Obtained without Energy Discrimination

Sei Fukushima[1,3], Takanori Murano[2], Hideyuki Takahashi[2] and Kazuhiro Kanda[1]
[1] LASTI, University of Hyogo, [2] JEOL Co., Ltd., [3] KMTL Co., Ltd.

Abstract

The CCD camera of the ultra-soft X-ray fluorescence spectrometer set on BL07A has no ability of energy discrimination. Thus, the overlapping of higher order lines cannot remove from the measured spectrum so that the observed spectral change should be examined essential or not. In this report, the spectral changes observed on P $L_{2,3}$ of GaP and InP were studied using the relativistic cluster calculation.

Introduction

These past 4 years, new type ultra-soft X-ray spectrometer has been developed and studied at the end point of BL07A. As already shown in past Annual reports, the detecting system used of ultra-soft X-rays is a back-side illumination type SSD camera for achieving high sensitivity and high detecting efficiency[1]. One the other hand, this detecting system has no ability of energy discrimination. Thus, the spectrum obtained this spectrometer is easy to receive the interference of higher order lines originated from another heavy element in the sample. In the most cases such as oxides or nitrides, the course of the higher order lines can be estimated easily. An example of such cases, LiF, is shown in Fig.1[1], which spectrum was measured by electron beam excitation. In contrast, there are some cases that the course of the spectral changes cannot be easily estimated that it is essential or interference of the higher order lines. This point is the serious problem for the chemical state analysis using the spectral changes. One of the effective solution for this problem is the storage of the experience aided the theoretical study.

In this report, the spectral changes observed on P $L_{2,3}$ of GaP and InP were studied. The oxidation state and coordination state of P in both compounds is exactly same. Whether it could distinguish these two compounds from the change of the spectrum was discussed using the cluster calculation.

Measurement spectra

In Fig.2, P $L_{2,3}$ ultra-soft X-ray spectra of GaP and InP are shown. These spectra were obtained with the electron beam excitation equipment of which composition of the spectrometer was almost same as that of BL07A. The measurement was carried out by the research laboratory of JEOL Co. Ltd.

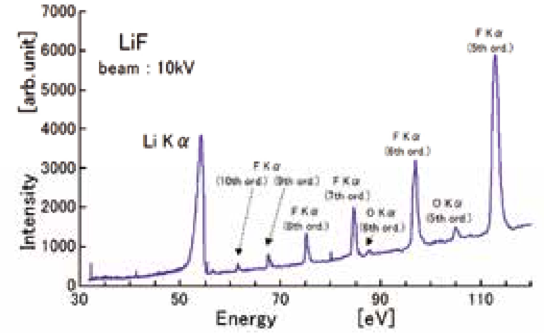

Fig.1 Ultra-soft X-ray spectrum of LiF with 10kV electron beam excitation[1].

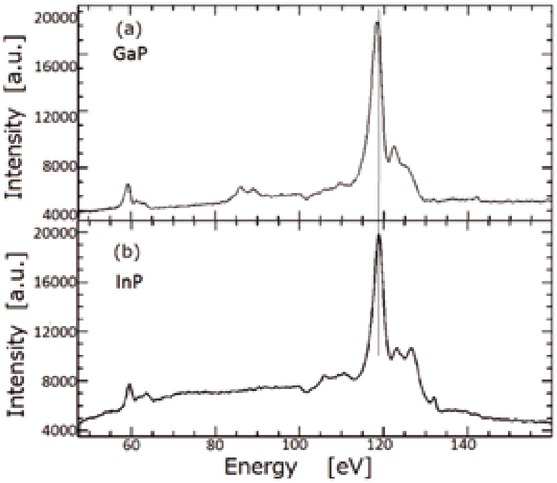

Fig.2 P $L_{2,3}$ ultra-soft X-ray spectra by electron beam excitation. (a)GaP (b)InP

As shown in Fig.2, the main peak of GaP shifts lower energy side slightly from InP. And the structure at the right side of main peak (above 120eV) is remarkably different each other. Using the energy values of Ga $L\alpha$ and $L\beta$ by Bearden [2], the most of structures on P $L_{2,3}$ of GaP can be assigned the higher order lines of

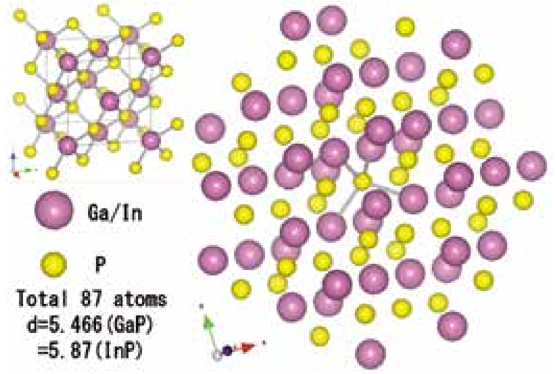

Fig.3 The cluster model used in this study.

Ga $L\alpha$ and $L\beta$. However, there were no higher order lines of In L series which showed agreement with the structure on InP spectrum. In addition, the energies of In M series were not reported anywhere. Thus, theoretical calculation for obtain the energy values of In M series of InP should be necessary.

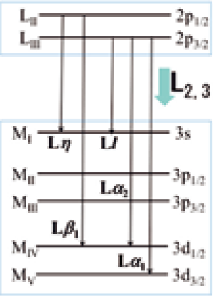

Fig.4 Electron transition diagram.

As known well, the crystal structure of GaP and InP is exactly same, and the only difference is the lattice constant (GaP : 0.5466nm[3], InP : 0.587nm[4]). Thus, if this spectral change above 120eV is caused by the difference of the bonding structure, study aided the cluster calculation should be useful too.

Calculation

In Fig.3, the cluster model for both GaP and InP is shown. The crystal structural data of both compounds were obtained from the database of NIMS "Atom Work" (http://crystdb.nims.go.jp/crystdb/search-materials) as CIF files. Both two cluster models were $PX_4P_{12}X_{12}P_6X_{12}P_{24}X_{16}^{3+}$ (X=Ga or In) which were constructed within 7th neighbor atoms from the center P atom.

The calculation method used in this study was DV-Xα [5]. In the case of P $L_{2,3}$, only transitions between 3d-2p (corresponding with $L\alpha_{1,2}$, $L\beta_1$) and 3s-2p ($L\eta$, Ll) should be target for calculation, because the energy splitting of sub-shell (between L_{II} and L_{III}, M_{IV} and M_V) are sufficiently narrow. However, in the cases of Ga and In, the energy splitting of sub-shell are not disregarding, as shown in Fig.4. Thus, in order to calculate individual energies of these transitions, the relativistic calculation method is necessary. The relativistic DV-Xα [6] was also used for this aim, which was opened to public in the limitation.

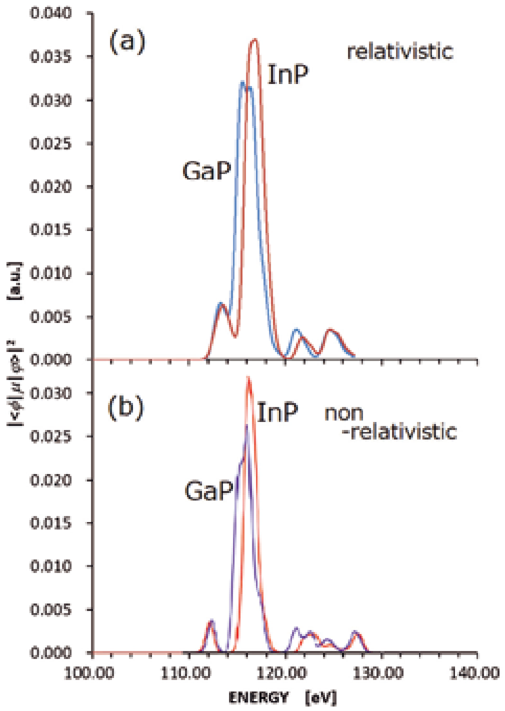

Fig.5 Results of the cluster calculation
(a) relativistic (b) non-relativistic

Results and Discussion

In Fig.5, theoretical P $L_{2,3}$ spectra of GaP and InP by relativistic and non-relativistic calculation are shown individually. All the lines were broadened with a Gaussian profile of which FWHM was 1eV. In both calculation results, the energy change of main P $L_{2,3}$ peak shows same tendency. Thus, it can be clearly said that this small energy changes between GaP and InP is essential so that one can distinguish these two materials using this energy change.

As the result by the relativistic calculation shows clearly, the difference of the structure below 120eV between both materials is hard to be recognized. Because the each sub-shell of Ga or In gives any effect to chemical bonding individually, the relativistic calculation should give more correct results than non-relativistic calculation.

For making advance of discussion, the energy calculation of Ga $L\alpha_{1,2}$, $L\beta_1$ of GaP and In M series of InP was carried out. According to Barden's data [2], the energy of Ga $L\alpha_{1,2}$ is 1097.92eV and the splitting value between $L\alpha_1$ and $L\alpha_2$ is negligible in 1st order. Thus, in the case of overlapping on to P $L_{2,3}$ line, the splitting of $L\alpha_{1,2}$ is not necessary to consider. The results of the relativistic calculation Ga $L\alpha_{1,2}$, $L\beta_1$ of GaP and In M series of InP are shown in Fig.6. All the lines were broadened with a Gaussian profile of which FWHM was 10eV. 10eV width of 1st. order peak is about

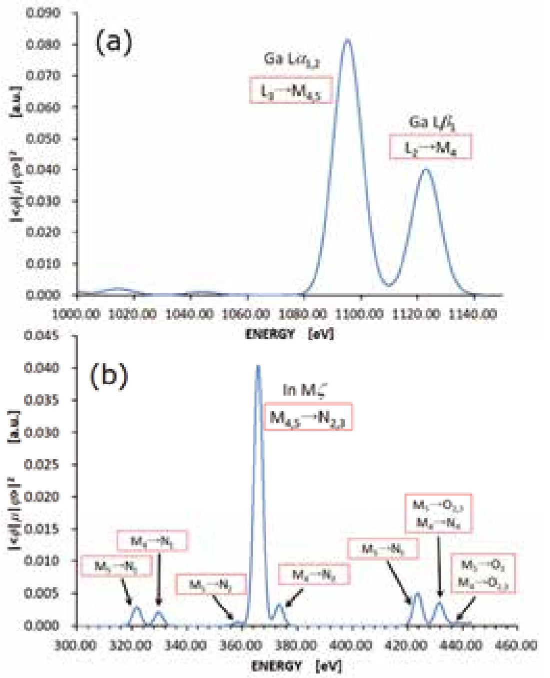

Fig.6 (a) Ga L$\alpha_{1,2}$, Lβ_1 of GaP, and (b)In M series of InP by the relativistic cluster calculation.

1eV width of 9th order, and 1eV is comparable value of the energy resolution of the spectrometer used in this study. Barden's data [2] assigned $M_{4,5}$-$N_{2,3}$ transition to Mζ in Sn case, so that the strongest $M_{4,5}$-$N_{2,3}$ transition line of In shown in Fig.6 was also assigned Mζ.

Fig.7(a) shows the result that superimposed 9th order Ga L$\alpha_{1,2}$ and Lβ_1 calculated from Fig.6 on P $L_{2,3}$ of GaP shown in Fig.5(a). The intensity of 9th order Ga lines were adequately adjusted referring to the observation spectrum. As shown in Fig.5(a), the structure above 120eV consists of two peaks of the almost equal height. However, as shown in Fig.2(a), the measured structure has two different strength peaks, and the synthesized spectrum shown in Fig.7(a) is very similar to Fig.2(a). This result also indicates this shape of structure reflects the higher order Ga lines in GaP case.

Fig.7(b) was synthesized with Fig.5(a) and 3rd order In M series calculated from Fig.6(b). It can be seen that the energy position of 3rd order In Mζ is almost same the left side peak of the structure above 120eV. However, in Fig.2(b), the intensity of two small peaks is almost same, and this is well corresponding with the calculation result shown in Fig.5(a). Thus, in the case of InP, it can be concluded that the overlap of 3rd order In Mζ is not remarkable, and that the structure above 120eV shown in Fig.2(b) can be regarded as the true structure.

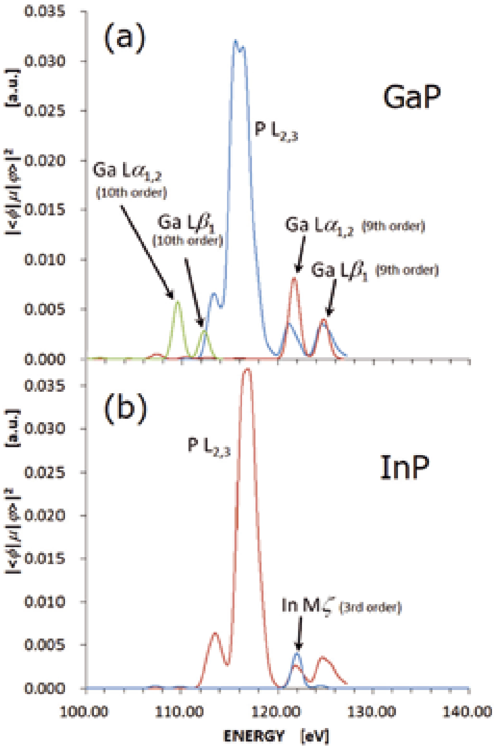

Fig.7 The results of the superimpose Fig.6 on Fig.5. (a) GaP (b) InP.

Conclusion

In this report, the difference of P $L_{2,3}$ spectra of GaP and InP was discussed with the relativistic cluster calculation as the example of examining the change of ultra-soft X-ray spectrum measured with the detector which has not ability of energy discrimination. From the result of calculation, it was found out that the energy of the main peak of P $L_{2,3}$ of GaP was slightly lower than InP. And, about the structure above 120eV on P $L_{2,3}$, it was also found out that the shape of this of GaP was almost same as InP, and that the higher order (9th order) Ga L$\alpha_{1,2}$ was remarkably overlapped this structure in the case of GaP in spite for no observation of higher order lines of In M series on that structure of InP. In addition, it can be said that the theoretical examination is so useful for distinguish that the observed spectral change is essential or not.

In spite of above discussion, the causes of some of other spectral differences of P $L_{2,3}$, the structure around 100~110eV for example, could not be revealed. It can be presumed that the origin of this structure might not be the bonding structure of GaP or InP, and that the characteristic of the spectrometer might be a cause of this structure.

References

[1] S. Fukushima *et al*. Microchim. Acta **161**, pp.399 (2007).

[2] J. A. Bearden, Rev. Mod. Phys. **39**, pp.78 (1967)

[3] R. Saravanan *et al.* J.Phys.Status Solidi B **165**, pp.67 (1991).

[4] R. Saravanan *et al.* Z. Kristallogr. **200**, pp.7 (1992).

[5] H.Adachi *et al.* J. Phys. Soc. Jpn. **45**, pp.875 (1978).

[6] H.Adachi, Technol. Rept. Osaka Univ. **27**, pp.569 (1977).

Growth of Monolayer Hexagonal Boron Nitride in Ultra-High Vacuum for In-Situ Spectroscopic Analyses

Satoru Suzuki and Yuichi Haruyama,
LASTI, University of Hyogo

Abstract

We succeeded in growing atomically thin h-BN films in the endstation of BL7B. This enable us to analyze the h-BN film by electron spectroscopic techniques using synchrotron radiation light with keeping the sample in ultra-high vacuum.

Introduction

Hexagonal boron nitride (h-BN) is a structural µanalogue of graphene and has a layered structure consisting of B_3N_3 six-membered rings. On the other hand, the electronic structure of h-BN is complementary to that of graphene. It is an insulator with a large bandgap (about 6 eV), in good contrast to that graphene is metallic. Recently, many applications of h-BN are expected, such as a substrate material for graphene devices and an atomically thin tunneling barrier. To study the electronic structures of such a 2D material with sub-nanometer-thick, soft x-ray spectroscopy is very suitable, because interaction of soft x-ray and a material is very large.

Now, the chemical vapor deposition (CVD) method is usually used to grow atomically thin h-BN. However, the CVD method often uses toxic and flammable gases as a source and carrier gas. Thus, safety is the concern. Moreover, the CVD growth is usually done in relatively low vacuum or even in atmospheric pressure. Therefore, in-situ analyses of the growth by electron spectroscopic technique is generally very difficult.

We have proposed the diffusion and precipitation method for growing atomically thin h-BN [1-3]. This method only utilizes a solid source and solid state reaction. Thus, it is much more low-cost and safer than the CVD method. Here, based on our previous studies [1-3], we report monolayer h-BN growth by the diffusion and precipitation method in ultra-high vacuum. This enables us to analyze the h-BN film by electron spectroscopic techniques using synchrotron radiation light with keeping the sample in ultra-high vacuum.

Experiments and Results

Figure 1 shows a schematic of the diffusion and precipitation method. A Ni foil with a thickness of 25 µm (Nilaco) was commercially available. As a B and N source, amorphous BN (a-BN) with a thickness of ~100 nm was deposited on the Ni foil by using radio frequency magnetron sputtering method [Fig. 1(a)]. Then, the sample was mounted in the sample preparation chamber of the endstation of BL7B. The a-BN-deposited side of the Ni foil was irradiated by an electron beam and the sample was heated at about 900-1000°C for typically 30 m [Fig. 1(b)]. At high temperatures, B and N

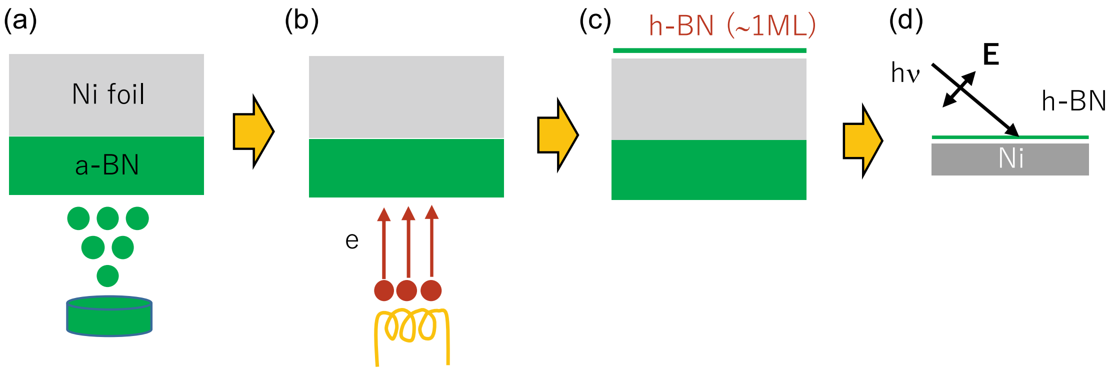

Fig.1 Schematic of monolayer h-BN growth by the diffusion and precipitation method. (a) a-BN deposition on a Ni foil. (b) heating by electron bombardment in the endstation of BL7B. (c) h-BN growth on the opposite face by diffusion and precipitation. (d) in-situ analysis using synchrotron radiation light.

atoms diffuse into Ni foil. The diffusion of B atoms can simply be explained by the bulk diffusion, because B is slightly soluble in Ni at such a high temperature [1]. The diffusion of N atoms is very puzzling, because N solubility in Ni is known to be almost zero even at high temperatures [1]. We think that the mass transport of N atoms is caused by the grain boundary diffusion, although the details are still open question. Anyway, atomically thin h-BN is ultimately formed on the back side of the Ni foil [Fig. 1(c)]. The sample was transferred from the sample preparation chamber to the analysis chamber of the endstation of BL7B. Now, we can analyze the h-BN film by photoemission spectroscopy and x-ray absorption spectroscopy with synchrotron radiation light [Fi.1(d)].

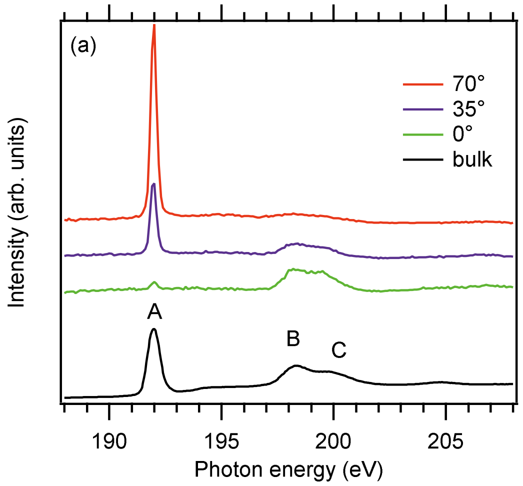

Fig.2 Polarized B-*K* absorption spectra of monolayer h-BN/Ni grown by the diffusion and precipitation method and of bulk h-BN.

Figure 2 shows B-K absorption spectra of a sample after the procedure shown in Fig. 1 and of bulk h-BN. The results unambiguously show that h-BN is formed on the Ni foil. The large incidence angle dependence indicates that the h-BN sheet is parallel to the surface of the Ni foil, as reasonably expected. Currently, detailed electronic structure of the monolayer h-BN on the metal foil and the growth process of h-BN are under investigation. Synchrotron radiation photoemission spectroscopy and x-ray absorption spectroscopy will be powerful tools to address these issues.

References

[1] S. Suzuki et al., J. Phys. D: Appl. Phys. **45**, 385304 (2012).

[2] S. Suzuki et al., J. Vac. Sci. Technol. B **31**, 041804 (2013).

[3] S. Suzuki et al., Jpn. J. Appl. Phys. **56**, 06GE06 (2017).

Evaluation on the molecular orientation in photoreactive liquid crystalline polymer films by NEXAFS spectroscopy

Y. Haruyama[1], M. Okada[1], M. Kondo[2], and N. Kawatsuki[2]
[1] Laboratory of Advanced Science and Technology for Industry, University of Hyogo
[2]Graduate School of Engineering, University of Hyogo

Abstract

The molecular orientation of the pre-aligned photoreactive liquid crystalline polymer PMCB10M films has been investigated using the near-edge X-ray absorption fine structure (NEXAFS) at the C K-edge region. By combining the thickness dependence of PMCB10M films and three types of simultaneous detection methods of NEXAFS measurements, the molecular orientations of PMCB10M films at the near-surface (<2 nm), at the inner-surface (~10 nm) and in the bulk (~100 nm) were evaluated. In addition, it was found that the orientation of the liquid crystalline molecules near the surface was parallel to the surface irrespective of the thickness of PMCB10M films.

Introduction

The studies on the photoinduced molecular orientation of the polymeric films have attracted significant attention for a potentially wide range of applications such as birefringent optical devices, the photo alignment layer of liquid crystal displays, and optical memories. The polymethacrylate comprised of 4-methoxycinnamolybihenyl (MCB) side groups connected via decylene spacers (PMCB10M) is one of photoreactive liquid crystalline polymers [1, 2]. It was reported that the molecular orientation of photoreactive liquid crystalline polymer controlled by the linearly polarized UV radiation and the subsequent annealing procedure [1, 2]. However, the molecular orientation of photoreactive liquid crystalline polymer near the surface and the interface between the film and the substrate is not clear. To investigate the molecular orientation of PMCB10M films, NEXAFS spectra at the C K-edge region were measured by three types of simultaneous detection methods with the different probing depth.

Experiments

PMCB10M was synthesized as described in a previous paper [1]. PMCB10M films of 15-150 nm thickness were prepared by spin-coating a tetrahydrofuran (THF) solution of the polymers onto ITO coated glasses. The pre-aligned PMCB10M films were prepared by irradiating the linearly polarized UV light to the films and by subsequently annealing at 120-240 °C for 10 minutes.

NEXAFS experiments were performed at a beamline 7B of the NewSUBARU synchrotron radiation (SR) facility, the University of Hyogo. NEXAFS spectra were simultaneously measured by Auger electron yield (AEY), total electron yield (TEY) and fluorescence yield (FY) methods as shown in figure 1. The sample could be rotated around a vertical axis to change the incidence angle of the SR to the sample surface. The direction of the linear polarization in the SR was horizontal. To evaluate the molecular orientation of PMCB10M films, NEXAFS spectra were recorded in parallel and perpendicular configurations, where the direction of linearly polarized UV light irradiated to the films was parallel and perpendicular to that of the linear polarization in the SR, respectively.

Results and discussion

Figures 2(a) and 2(b) show the C K-edge NEXAFS spectra of pre-aligned PMCB10M films, measured by the AEY method, as a function of incidence angle of the SR in parallel and perpendicular configurations, respectively. The thickness of PMCB10M films was 150 nm. A sharp peak at 284.8 eV, which was assigned to transitions from the C 1s orbital to the unoccupied π* orbitals originating from aromatic ring sites, was observed [2, 3]. With increasing

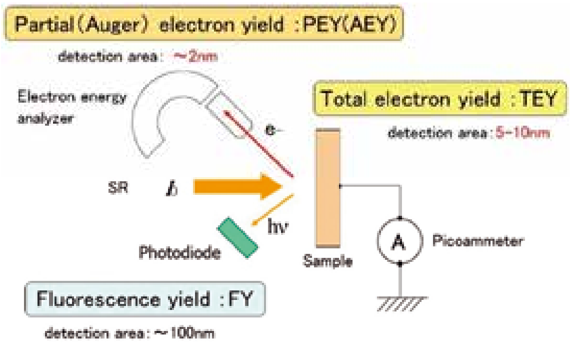

Fig. 1 Three types of simultaneous detection methods with the different probing depth [4].

the incidence angle, the intensity of the peak at 284.8 eV decreased remarkably in the parallel configuration while it was almost unchanged in the perpendicular configuration. This indicates that the orientation of the liquid crystalline molecules in PMCB10M at the near-surface is parallel to the polarization direction of the UV light. On the other hand, the angular dependence of the intensity at 284.8 eV in the TEY method became smaller than that in the AEY method as shown in figure 2(c). In addition, the angular dependence of the intensity at 284.8 eV in the FY method as shown in figure 2(e). had the similar angular dependence to that in the TEY. These results indicate that the orientations of the liquid crystalline molecules in pre-aligned PMCB10M films at the inner-surface and in the bulk are different from that at the near-surface.

NEXAFS spectra of pre-aligned PMCB10M films in the thickness of 15 and 55 nm were also measured in parallel and perpendicular configurations. In the case, the angular dependence of the intensity at 284.8 eV in the AEY method showed the similar behaviour to that in the thickness of 150 nm. Therefore, it was found that the orientation of liquid crystalline molecules near the surface was parallel to the surface irrespective of the thickness of PMCB10M films.

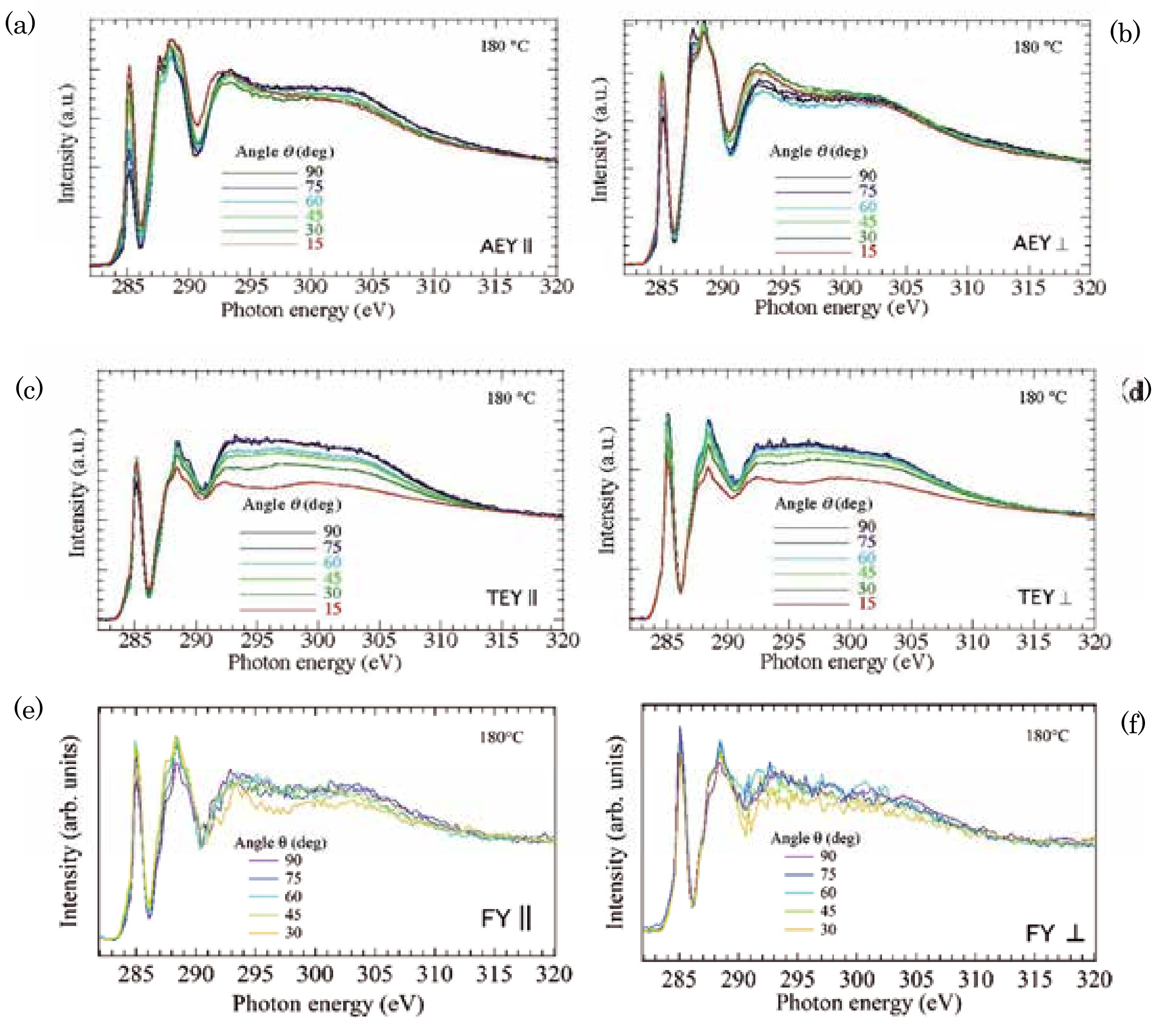

Fig. 2 C K-edge NEXAFS spectra of pre-aligned PMCB10M films, measured by the AEY, TEY, and FY methods, as a function of incidence angle of the SR in parallel (a), (c), (e) and in perpendicular (b), (d), (f) configurations, respectively.

References

[1] N. Kawatsuki and J. Horii, Mol. Cryst. Liq. Cryst. **498**, 49, (2009).
[2] N. Kawatsuki, Y. Taniguchi, M. Kondo, Y. Haruyama, and S. Matsui, Macromolecules **48**, 2203, (2015).
[3] N. Kawatsuki, Y. Inada, M. Kondo, Y. Haruyama, and S. Matsui, Macromolecules **47**, 2080, (2014).
[4] J. Stöhr, Nexafs Spectroscopy, (Springer Series in Surface Sciences, 1996).

Analysis of Spray-pyrolysis Deposited NiOx Layers with Different Temperatures in Inverted Perovskite Solar Cells

Naoyuki Shibayama[1], Hidetaka Sugita[1], Yuya Nakazawa[1], Hiroyuki Kanda[1], Fukumoto Syota[1],
Yuichi Haruyama[2], and Seigo Ito[1]
[1]Graduate School of Engineering, University of Hyogo
[2]Laboratory of Advanced Science and Technology for Industry, University of Hyogo

Abstract

We investigated the effect of the NiOx layers on the performance of perovskite solar cells through detailed analysis (X-ray diffraction, X-ray and vacuum ultraviolet photoelectron spectroscopy) of NiOx layers fabricated at different temperatures using spray pyrolysis deposition. It was confirmed that the conversion efficiency of the perovskite solar cell is high as the crystallite size of NiOx is large. It was also revealed that Na^+ ions migrated from the glass substrate changed the band state of the NiOx layer and affected the conversion efficiency. Based on the results of this study, it was clarified that doping materials for hole and electron transport materials affect the band structure. Engineering of these materials is important as a guide for improving the performance of perovskite solar cells.

Introduction

The NiOx layer is actively used as hole extraction layer for inverted structure perovskite solar cells. However, clear guidelines on NiOx chemical composition, manufacturing methods, energy levels, and the hole-transport process remain unclear.

In this conference, high-density NiOx layers with various manufacturing temperatures are produced with Nickel acetylacetonate using the SPD method in order to improve the performances of inverted perovskite solar cells. The chemical composition of the NiOx is investigated using X-ray photoelectron spectroscopy (XPS), and X-ray diffraction (XRD). Furthermore, the influence of Na^+ ions in the valence band of the NiOx layer is investigated by vacuum ultraviolet photoelectron spectroscopy (PES) using synchrotron radiation. The results showed that the conversion efficiency of the perovskite solar cell is high as the crystallite size of NiOx is large. The highest perovskite solar cell conversion efficiency was obtained at a NiOx layer production temperature of 500 °C. Inversed perovskite solar cells were fabricated with over 16.1% conversion efficiency and no observed hysteresis. The conversion efficiencies of the perovskite solar cells using NiOx films with various deposition temperatures are summarized in Table 1.

Experiments and Results

The perovskite solar cells conversion efficiency increased along with the NiOx layer production temperature to 550 and 600 °C; however, it decreased slightly when the temperature increased further to 600 °C. As a result, the perovskite solar cell conversion efficiency reached its peak when the NiOx layer production temperature was 500 °C. To highlight the performance change, we herein investigated the composition, structure and the band state of the NiOx layers.

To investigate the states of the regions near the edges of the valence bands of the NiOx layers, PES measurements were carried out with a BL-07B end station at the NewSUBARU synchrotron radiation facility at the University of Hyogo, and the results are shown in Figure 1. The regions near the edges of the valence bands of the NiOx correspond to Ni 3d (label A), O 2p

Table 1. Parameters of photoelectric characteristics of perovskite solar cells.

NiOx fabrication temperatures	J_{sc} (mA/cm^2)	V_{oc} (V)	FF (-)	η (%)
300 °C	15.1	0.921	0.653	9.06
400 °C	17.6	0.966	0.657	11.2
500 °C	19.6	1.08	0.760	16.1
550 °C	18.2	1.01	0.706	12.9
600 °C	17.5	0.983	0.687	11.8

(label B), and the charge transfer transition from an O 2p level to Ni 3d photoionization (label C). From the PES measurement results, the region (around 4-5 eV) corresponding to O 2p was stronger at 300 and 600 °C than at 500 °C. This is because the influence of the O 2p orbital increased because the proportion of oxygen in NiOx increased owing to the loss of Ni ions. Although the ratio of Ni^{2+} to Ni^{3+} ions affects the energy levels in the vicinity of the HOMO, a change in these energy levels does not contribute to hole extraction in perovskite solar cells. From these results, it was found that the valence of the Ni ions has little influence on the performance of the solar cells.

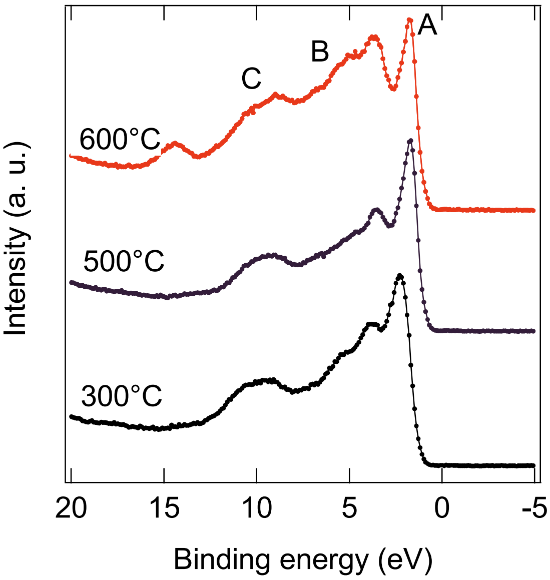

Fig. 1. Spectra obtained by PES using synchrotron radiation in the valence-band region of the NiOx layer as a function of the photon energy, taken at a photon energy of 120 eV.

Both the structures and crystallite sizes of the thin NiOx films formed by SPD were investigated via grazing-incidence X-ray diffraction (GIXRD), as shown in Figure 2. The five peaks that appeared at 2θ values of approximately 37.6° 43.6°, 63.3°, 75.6°, and 79.6° were assigned to the 111, 200, 220, 311, and 222 planes, respectively, and then attributed to the randomly oriented NiOx crystal. At 250 °C, no diffraction peaks were observed because the NiOx film did not crystallise. This implies that crystallised NiOx films formed with annealing temperatures above 300 °C.

The NiOx crystallite sizes were calculated from the intensities of the 200 peaks using the Scherrer equation, and the results are shown in Figure 1, which indicates that their sizes increased with increasing SPD temperatures. The size of a NiOx crystallite and the tendency of conversion efficiency were consistent, except at 550 and 600 °C, where the FTO layer broke beyond the glass transition point. In other words, as a guideline for manufacturing high-performance inverted perovskite solar cells, it is important to enlarge the crystallites in the NiOx film**.**

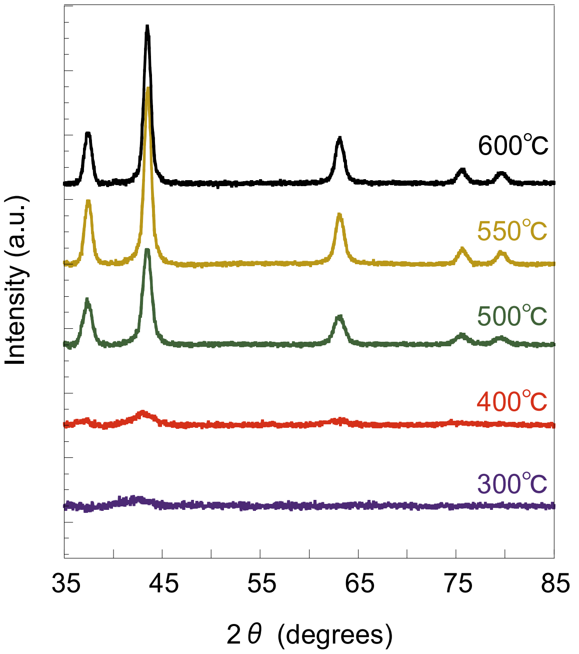

Fig. 2. Grazing-incidence X-ray diffraction patterns of NiOx films for various SPD fabrication temperatures.

Conclusions

We demonstrated that it is related to the NiOx crystallite size and the conversion efficiency of the perovskite solar cells, which can be used as a guideline to achieve high performance. The highest perovskite solar cell conversion efficiency was obtained at a NiOx layer production temperature of 500 °C. In the inverse perovskite solar cell, the conversion efficiency exceeded 16.1%, and hysteresis was not observed. Moreover, the measurements of the valence band using synchrotron radiation indicated that the ratio of Ni^{2+} to Ni^{+3} had little effect on the solar cell performance. This is an important guideline for improving the performance of perovskite solar cells.

References

[1] A. Kojima, K. Teshima, Y. Shirai, T. Miyasaka, Organometal Halide Perovskites as Visible-Light Sensitizers for Photovoltaic Cells, J. Am. Chem. Soc. **131**, 6050 (2009).

[2] J. Nakazaki, H. Segawa, Evolution of organometal halide solar cells, J. Photochem. Photobiol. C. 2018, in press.

Cleaning of Carbon-Contaminated Ni-coated Mirror Using Atomic Hydrogen

Masahito Niibe[1], Tetsuo Harada[1], Akira Heya[2], Takeo Watanab[1]e, and Naoto Matsuo[2].
[1]LASTI, University of Hyogo, [2]Graduate School of Eng., University of Hyogo

Abstract

In synchrotron radiation (SR) mirrors coated with easily-oxidized metal such as Ni or Cr, the UV-O_3 ashing method cannot be used for removing the contaminated carbon film deposited during use in the beamline. We have demonstrated that surface treatment technology using atomic hydrogen is effective as a new contaminated carbon film removal technology. Hydrogen gas was flew into contact with tungsten mesh (catalyst) heated to 1700 °C. to obtain atomic hydrogen. By flowing this atomic hydrogen on the surface of the Ni-coatrd mirror, deposited contaminants could be almost completely removed. The reflectance of the mirror recovered from about 10% to about 70% at the C-K absorption region. The reflectance also increased about 20% at the photon energy greater than 300 eV because of the removal of carbon film and reduction of native oxide at the mirror surface.

Introduction

Optical elements such as metal coated mirrors installed in synchrotron radiation (SR) beamlines are contaminated with mainly carbon consisting film which is deposited during use, therefore the reflectance of the mirrors decreases. In many SR facilities, efforts to deal with this problem have been done for a long time [1-3], but it has not yet been completely solved. When the coating material of the mirror is a noble metal such as Au, Pt, etc., ashing method using ozone gas under ultraviolet irradiation (VU-O_3 ashing) is used to remove the contaminants [4]. However, when the coating material is an easily-oxidizable metal such as Ni or Cr, there is concern that the reflectance may be lowered due to oxidation of the metal surface. As a recent previous study, Toyoshima succeeded in removing contaminants *in situ* by introducing oxygen gas into a mirror chamber at 8×10^{-2} Pa and irradiating undulator light to a Cr-coated mirror [5]. However, in order to realize such a mechanism, it is necessary to install a large differential pumping system, and oxidation of the coating material has still been observed. Also, Swaraj reported that contaminants were removed and the reflectance recovered by keeping a small amount of oxygen gas ($\sim 4 \times 10^{-6}$ Pa) for 2 years in the beam line during the time of beam operation [6]. However, this method takes time to recover reflectance and the problem of surface oxidation for easily-oxidizable metal is still unsolved.

We investigated carbon contamination removal method of synchrotron radiation mirror by treatment with atomic hydrogen (AH treatment). There is a possibility that AH can prevent oxidation even for a metal film which is easily oxidized. We report the AH treatment on mirrors which actually received carbon contamination during the beamline operation and evaluate the reflectance of the mirror before and after the treatment.

Experiments

The specimen is a Ni coated mirror on which contaminants are deposited, and which has been used in the beam line, BL-09 [7], of the NewSUBARU synchrotron radiation facility. For cleaning of contaminants, atomic hydrogen irradiation equipment of the University of Hyogo [8] was used. The W mesh was heated to 1700 °C, and hydrogen gas was passed there at a gas pressure of 30 Pa to obtain atomic hydrogen. The distance between the W mesh and the treated sample was 90 mm, and the heating operation of the sample was not performed.

The evaluation of the mirror before and after the AH treatment was carried out with visual observation (photograph), surface profile measurement by optical interferometer (Zygo, NewView7300), surface roughness measurement by atomic force microscope (AFM), thin film structure in depth direction evaluation by hard X-ray reflectometry at grazing incidence (XRR), and surface composition analysis by X-ray photoelectron spectroscopy (XPS, PHI 5000 VersaProbe). Because the size of the mirror is too large to introduce in the XPS chamber, we used dummy Ni coated mirror for XPS, which has slightly contaminated with carbon film and has been put together with the Ni-coated SR mirror during the AH treatment.

The soft X-ray reflectance of the mirror before and after this treatment was measured using a

BL-10 reflectometer [9] of the NewSUBARU facility. The measurement was carried out at a grazing incident angle of 3°, and the reflectance and its distribution at photon energy of 150 to 750 eV were evaluated.

Results

First of all, as a preliminary experiment, the surface roughness before and after the AHT was measured and compared with a mirror coated with Ni on the Si wafer substrate using atomic force microscope. As a result, the surface roughness hardly changed by this treatment.

The thickness of the contaminant on the Ni coated mirror was evaluated as 11 nm at the maximum as measured by the optical interference thickness gauge. The contaminants could be removed by 1 hr atomic hydrogen irradiation to such a degree that trace was visible by visual inspection. Figure 1. shows the photographs of Ni-coated mirror surface used in the beamline BL-09 of the NewSUBARU SR facility (a) before, and (b) after the AH treatment. By the surface profiler analysis, in this treatment, deposited contaminants remained about 1 nm at maximum.

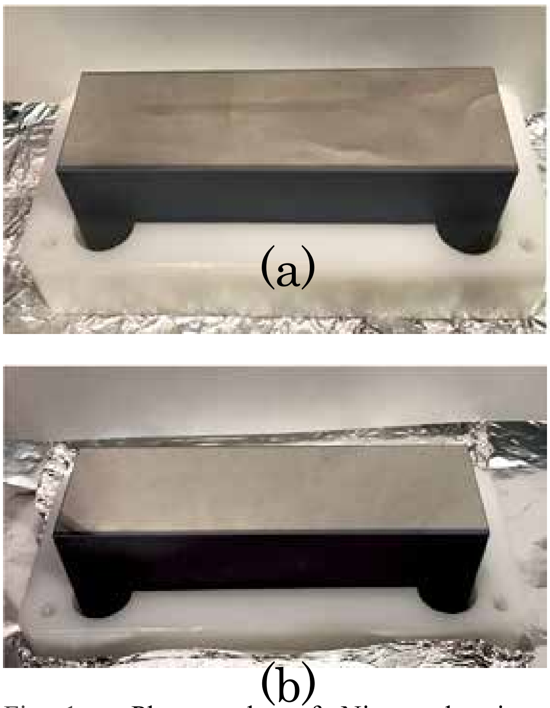

Fig 1. Photographs of Ni-coated mirror surface used in the beamline of the NewSUBARU SR facility (a) before, and (b)

Figure 2. shows the composition analysis of the reference mirror simultaneously introduced by XPS. Fig.2 showed that only the signal of C1s (280 eV) decreased and the signal of Ni2p (850 eV) increased and no special compound formation was observed.

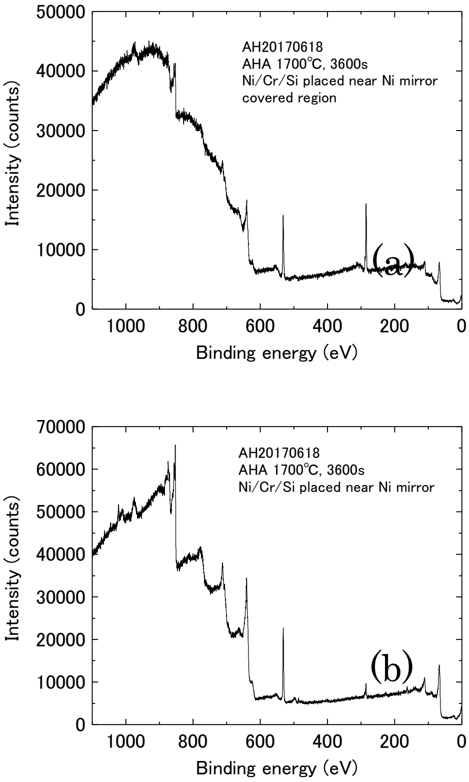

Fig 2. Composition analysis of the reference mirror simultaneously introduced by XPS, (a) before, and (b) after the AH treatment.

Figure 3. shows soft X-ray reflectance spectrum of the Ni coated mirror in a wide photon energy range from 150 to 750 eV before and after the AH treatment. As shown in Fig. 3, even in the region where the contaminants were thickly deposited, the reflectance could be recovered to about 10 → 70%.

It can be seen that the reflectance decreased to about 50% due to accumulation of carbon contamination even at an energy of 300 eV or higher above the C-K absorption edge. With this AH treatment, we could recover this reflectance to about 70%, this value is close to the theoretical reflectance.

At the photon energy of 280 eV or less, the reflectance is slightly decreased by the AH treatment. This is because C, which is advantageous in terms of optical constant at 280 eV or less, disappears from the surface, which is theoretically expected.

After this experiment, we also succeeded in removing the contamination film by conducting AH treatment on the Ni-coated diffraction grating (L150 × W30 × T20 mm, Si substrate) which also received carbon film contamination.

As summary, we attempted a new cleaning

method called atomic hydrogen treatment and could successfully remove carbon contaminants deposited on synchrotron radiation mirrors. The damage (roughening or compound formation) of the AH treatment to the mirror was very small. This method is very simple and there is a possibility that contamination can be removed *in situ* without installing differential pumping system or irradiation of intense undulator radiation.

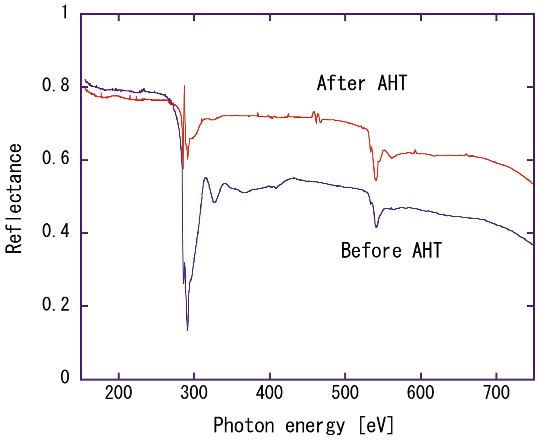

Fig 3. Change in reflectance of Ni-coated mirror before and after AHT.

References

[1] K. Boller, R.-P.Haelbich, H. Hogrefe, W. Jark and C. Kunz, Nuclear Instrum. Method. **208**, 273-279 (1883).

[2] T. Koide, S. Sato, T. Shidara, M. Niwano, M. Yanagihara, A. Yamada, A. Fujimori, A. Mikuni, H. Kato and T. Miyahara, Nuclear Instrum. Method. Phys. Research A**246**, 215–218 (1986).

[3] R. A. Rosenberg, Nuclear Instrum. Method. Phys. Research A**291**, 101–106 (1990).

[4] R. Kohli and K.L. Mittal Ed., *Developments in Surface Contamination and Cleaning* (Elsevier, Amsterdam, 2015), pp. 71–95.

[5] A. Toyoshima, T. Kikuchi, H. Tanaka, K. Mase, and K. Amemiya, J. Synchrotron Rad., **22**, 1359-1363 (2015).

[6] S. Swaraj, R. Belkhou, S. Stanescu, M. Rioult, A. Besson, and A. P. Hitchcock, J. Phys. Conf. Ser. **849**, 012046 (2017).

[7] M. Niibe, M. Mukai, S. Miyamoto, Y. Shoji, S. Hashimoto, A. Ando, T. Tanaka, M. Miyai, and H. Kitamura, AIP Conf. Proc. **705**, 576-579 (2004).

[8] A. Heya and N. Matsuo, Jpn. J. Appl. Phys. **46**, 3545-3548 (2007).

[9] H. Iguchi, H. Hashimoto, M. Kuki, T. Harada, T. Watanabe, and H. Kinoshita, Proc. SPIE **9658**, 965819 (2015).

Development of a standalone coherent EUV scatterometry microscope with high-harmonic-generation EUV source for EUV mask observation

Daiki Mamezaki, Tetsuo Harada, and Takeo Watanabe
Center for EUV lithography, LASTI, University of Hyogo

Abstract

We have developed a coherent EUV scatterometry microscope (CSM), which is a simple microscope without objective optics. The EUV phase and intensity images were reconstructed with diffraction images by ptychography. For a standalone mask review, the high-harmonic-generation (HHG) EUV source was employed. In this study, we updated the sample stage, pump-laser reduction system, and gas-pressure control system to reconstruct the image. As a result, an 88 nm line-and-space pattern and a cross-line pattern were reconstructed. In addition, a particle defect of 2 μm diameter was well reconstructed.

Introduction

Extreme-ultraviolet (EUV) lithography is the most promising method for manufacturing semiconductor electronic devices. The EUV mask is composed of an absorber pattern (50 - 70 nm thick) and a Mo/Si multilayer (280 nm thick) on a glass substrate, which has a three-dimensional (3D) structure at the EUV wavelength. The development of a review apparatus for the EUV mask pattern at an exposure wavelength of 13.5 nm is required. As the 3D structure modulates the EUV reflection phase, focus and pattern shifts are generated.[1] These phase modulations on the mask behave similarly to an aberration. Thus, the development of the EUV microscope that can observe both the intensity and phase images is strongly required to control this aberration. For EUV intensity and phase image observations, we developed a coherent EUV scatterometry microscope (CSM).[2,3] The CSM is a simple microscope without objective optics developed based on coherent diffraction imaging (CDI).[4] The EUV phase and intensity images are reconstructed with diffraction images, which are diffracted from the mask pattern with coherent EUV exposure. This coherent EUV illumination is a key element for the CSM. In the previous CSM system, a synchrotron radiation EUV light was used as a coherent EUV source. The synchrotron radiation is a large-scale facility, which is not practical to use in a factory. For practical uses, we have developed a high-harmonic generation (HHG) EUV source as the coherent EUV source of the CSM.[2] The high harmonics, including the EUV wavelength region, are pumped by a laboratory-scale femtosecond laser.[5] The HHG source is suitable for CDI because of its high coherence.

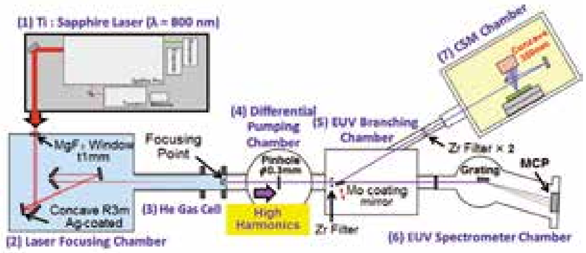

Figure 1. Schematic layout of the HHG-CSM system.

Experiments and Results

- HHG EUV source

Figure 1 schematically depicts the HHG-CSM system, which is composed of seven parts: (1) a Ti:sapphire femtosecond laser, (2) a laser-focusing chamber, (3) a gas cell, (4) a differential pumping chamber, (5) an EUV branching chamber, (6) a spectrometer chamber, and (7) a CSM chamber. As the pump laser system, we introduced the Spitfire Pro 6W (Spectra Physics), which is a commercially available table-top laser system. The main specifications of the pump laser are wavelength: 800 nm, repetition frequency: 1 kHz, pulse energy: 6 mJ, and pulse width: 36 fs. The pump-laser light is led to the laser focusing chamber. A thin MgF_2 (1-mm-thick) crystal was used as the vacuum window at the entrance of the laser focusing chamber, which would not cause the phase dispersion of the pump laser. The pump laser was focused in the gas cell by a silver-coated concave mirror (radius of curvature: 3 m) installed in the laser focusing chamber. The focusing chamber and gas cell were filled with helium gas with a pressure of 13.4 kPa. The focused Ti:sapphire laser pumped the output of the high harmonics through a nonlinear interaction with the helium gas. The 59th-order harmonics of 13.5 nm wavelength (EUV light) were used for the CSM system. The source of the EUV light was determined to be 28 µm in diameter on the basis of the full width at half maximum (FWHM) criterion. High harmonics were led to the CSM chamber by a branch mirror with a Mo single-layer coating in the branching chamber.

The HHG output included not only the EUV light but also the pump laser. As the pump laser power was 10^6 - 10^7 higher than the EUV output power, the pump laser power should be reduced to less than 1/10,000 of the EUV power. In the case of residual pump laser power, the CCD camera records the pump laser signal as the background. Three Zr filters (200 nm thick) with a silicon-nitride back support (50 nm thick) were inserted to reduce the pump laser power. However, the filters were easily broken by the pump laser owing to its high power. To reduce the pump laser power before the filters, a reduction pinhole of 0.3 mm diameter was inserted 600 mm downstream from the gas cell in the differential pumping chamber. The beam divergence of the pump laser (4 mrad) was more than 10 times larger than the EUV output (0.2 mrad). The EUV beam almost passed through the pinhole; however, the transmitted pump laser power was reduced to approximately 1/100. This reduction pinhole was a simple mechanical system with a high resistance to the pump laser power. With this reduction pinhole, the Zr filters were not broken by the pump laser power.

- CSM system

Figure 2 schematically depicts our CSM. The observation method is based on CDI, which is a simple system without objective optics. The CSM is composed of a concave mirror (radius of curvature: 350 mm) for focusing on the EUV mask, a Mo/Si folding mirror, an EUV-mask stage, and an EUV CCD camera (Roper Scientific MTE-2048B). The image size of the CCD camera was 27.6 × 27.6 mm^2. The distance from the mask surface to the CCD surface was approximately 109 mm. The HHG-CSM had a numerical aperture of 0.13. The expected spatial resolution was a 54 nm half-pitch. The angle of incidence in the mask was 6°, equal to that in the EUV exposure tool. The EUV mask was exposed to the high harmonics, which were monochromatized by the Mo/Si multilayer reflection and Zr filters. The diffraction from the EUV mask was directly recorded by the CCD camera. The diffraction image corresponded to the amplitude information in the frequency space. The focusing concave mirror had a radius of curvature of 350 mm and the distance between the light source and the CSM concave mirror was approximately 3.0 m. Therefore, the magnification of the CSM optics was 1/17. The source of the EUV light was 28 µm in diameter (FWHM). As a result, the expected focused beam size on the mask was 1.6 µm in diameter.

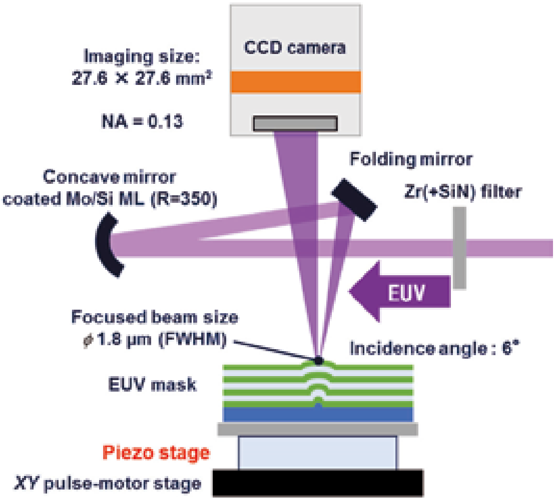

Figure 2. Schematic view of the CSM. The diffraction image is the directory recorded with the CCD camera.

- EUV mask imaging method

The EUV mask pattern was reconstructed by ptychography[6], which is a type of CDI. In ptychography, the sample is illuminated with step-and-repeat exposures. The diffraction images are recorded at each step position. The step length should be smaller than the beam diameter to have an overlapped region. Thus, some diffraction images have overlapped sample information under different illumination conditions. This redundancy is an important constraint condition in the iterative calculations of ptychography. In this experiment, the scanning step size was 0.8 µm, which was half the expected focused-beam size. The sample was illuminated in 15 × 15 steps, where the illuminated area was approximately a region of 12 × 12 μm^2. The diffraction images correspond to the amplitude information in the frequency space. To reconstruct the real space image, phase information was retrieved by the iterative calculations of Fourier and inverse-Fourier transforms with constraints. Therefore, the reconstructed image has amplitude and phase information. The position accuracy and the illumination beam stability of the shape and intensity are very important in reconstructing the mask pattern.

The output from the HHG gas cell included high-power pump laser light. In previous systems, the reduction pinhole was made of a SUS304 steel plate of 1 mm thickness. However, the pinhole melted owing to heating by the high-power pump laser beam. To improve the stability of the EUV light shape, a tungsten pinhole with high thermal resistance was employed. The thickness of this tungsten pinhole was the same as that of the SUS304 pinhole (1 mm thick). The melting point temperature of tungsten is 3,420 °C, which is 2.4 times higher than that of SUS304 (1,400 °C). The beam shape with this tungsten pinhole was significantly improved; the beam had a clear round shape without any scattering light. The pinhole did not melt after the half-year experiment using the CSM.

- Sample EUV mask

The EUV mask sample with an absorber line pattern on the substrate. In this experiment, two types of absorber patterns were observed. One was an 88 nm line-and-space (L/S) pattern, which was designed in a square region of 25 × 25 μm^2. Its line-to-space ratio was 1 to 1. This 88 nm L/S pattern corresponds to a 22 nm L/S pattern on a wafer. The other was a cross line-pattern of 2 μm width and 10 μm length.

- Diffraction image using HHG-CSM

Figure 3 shows diffraction images from (a) a cross-line pattern and (b) an 88 nm L/S pattern recorded by the CCD camera. The intensity is shown on a log scale. The measurement was carried out at 15 × 15 points for step-and-repeat measurements. The exposure time was 0.3 s at each point. The readout time of the CCD camera was 4.5 s per image. The total observation time was 17 min at 15 × 15 points, where the readout time was dominant for the observation time. The EUV light intensity was 1.3×10^7 counts per s on the CCD camera. The exposure dose on the mask was estimated to be 71 pW. The power density in the focused beam was approximately 3.5 mW/cm^2. This EUV power of the HHG-CSM was 175 times higher than that with the synchrotron bending light. In the diffraction image of the 88 nm L/S pattern, the brightest center part was the 0th-order light, which was a specular reflection from the mask. The 1st-order diffractions were recorded near the 0th-order light. Since the shape stability of the HHG EUV source was improved by the tungsten reduction pinhole, diffractions from the pattern were clearly recorded.

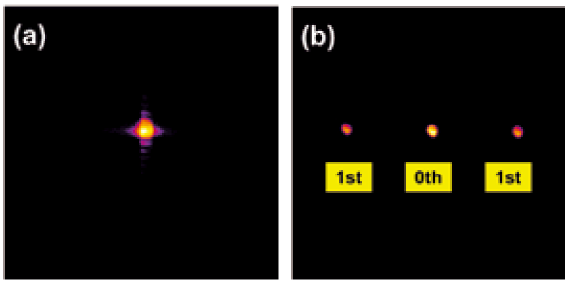

Figure 3. Diffraction images from (a) cross-line and (b) 88 nm L/S patterns.

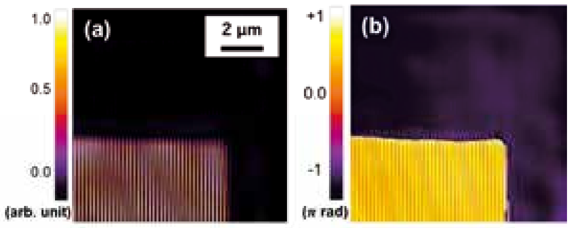

Figure 4. Reconstructed results of the corner structure of the 88 nm L/S pattern in terms of (a) intensity and (b) phase contrast.

- Reconstructed results of absorber patterns

Figure 4 shows a reconstructed image of a corner structure of the 88 nm L/S pattern. The intensity image is shown in Fig. 4(a), and the phase image in Fig. 4(b). The line and corner structures were well reconstructed. In the phase image, the phase modulation of the line pattern was observed. Thus, the CSM can observe the absorber pattern phase, which is very important in predicting the mask-induced aberration.

Figure 5 shows a reconstructed image of the cross-line pattern. The intensity image is shown in Fig. 5(a), and the phase image in Fig. 5(b). The cross structure was well reconstructed. In the right part of the cross pattern, there were some reconstruction errors, because this region was at the outer side of the step-and-repeat measurement. In the phase image, we estimated the phase shift of the absorber pattern. The cross-line region was the reflective multilayer without the absorber. The outside region of the cross structure was covered with the absorber layer. The difference between the absorber and reflective regions was estimated to be 2.8 rad (160°). The CSM can estimate the absorber phase shift, which is very important for the attenuated phase-shift mask. In addition to the cross pattern, the natural defect that seems to be a particle on the pattern was observed. The phase shift of the particle was the same as the absorber pattern, which indicated that this particle would be a peeled absorber. The phase shift was very helpful in characterizing the defect origin.

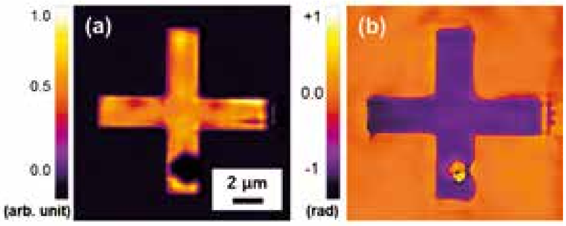

Figure 5. Reconstructed results of the cross-line pattern in terms of (a) intensity and (b) phase contrast.

The HHG-CSM clearly showed the 88 nm L/S and cross line patterns on the EUV mask. In addition, a natural defect that seems to be a peeled-absorber particle on the cross line was well reconstructed. A high spatial resolution of 54 nm half-pitch was expected in this CSM with an NA of 0.13 equivalents. This result shows the successful observation of the EUV mask pattern using the HHG-CSM. The CSM also showed the EUV reflection phase modulation, which causes the mask aberration and degrades the wafer image. Thus, the CSM will be a powerful system for EUV phase review in factories, such as mask shops and semiconductor fabrication plants.

Acknowledgement

The HHG EUV source was developed by Yutaka Nagata of RIKEN.

References

[1] T. Last, L. de Winter, and J. Finders, Proc. SPIE **9635**, 96350K (2016).
[2] M. Nakasuji, A. Tokimasa, T. Harada, Y. Nagata, T. Watanabe, K. Midorikawa, and H. Kinoshita, Jpn. J. Appl. Phys. **51**, 06FB09 (2012).
[3] Y. Tanaka, T. Harada, T. Amano, Y. Usui, T. Watanabe, and H. Kinoshita, Jpn. J. Appl. Phys. **53**, 06JC03 (2014).
[4] J. Miao, D. Sayre, and H. N. Chapman, J. Opt. Soc. Am. A **15**, 1662 (1998).
[5] Y. Nagata, T. Harada, M. Nakasuji, H. Kinoshita, and K. Midorikawa, Proc. SPIE **8849**, 884914 (2013).
[6] J. M. Rodenburg and H. M. L. Faulkner, Appl. Phys. Lett. **85**, 4795 (2004).

Evaluation of Block Copolymer Structure Using Soft X-Ray Scattering (BL-10)

Yusuke Nakatani, Tetsuo Harada, Motoyuki Yamada, and Takeo Watanabe
Center for EUV lithography, LASTI, University of Hyogo

Abstract

We developed a scattering measurement method using soft X-rays near the carbon absorption edge. Since the absorption spectrum varies in the near carbon absorption edge for each polymer molecule, the individual physical structures can be observed from the scattering profile with different photon energy. In this study, both the physical and chemical structures of the triblock terpolymers such as poly(isoprene-block-styrene-block-(2-vinylpyridine)) which consists of polyisoprene, polystyrene, and poly(2-vinylpyridine) were observed. By varying the photon energy of the scattering measurement, the scattering light intensity changed greatly, and the signal from each polymer could be evaluated. The soft X-ray scattering measurement at the near absorption edge can be measured the molecular structure of a composite material such as a blended polymer individually and can be utilized in material development.

Introduction

The directed-self-assembly (DSA) is one of the candidates for the advanced lithography of half pitch (hp) 5 nm and below to fabricate semiconductor devices.

In general, the X-ray absorption spectroscopy (XAS) is very powerful tool to evaluate the electronic state of each element of the chemical compound. We have developed this method for characterizing extreme-ultraviolet (EUV) resist materials at NewSUBARU BL-10 beamline [1]. Under EUV exposure, from the absorption peak value and the chemical shift in the X-ray absorption spectra, the chemical bonding changes can be estimated at the C_K region. As the result, it can be understood the EUV chemical reaction for advanced EUV resist materials by XAS measurement. Recently, evaluation of stochastic process in resist such as acid diffusion and its distribution, and distribution of functional groups become significant issue to achieve low line-edge-roughness. Thus, it is required to evaluate the chemical state and functional groups distribution in nanometer scale. If the spatial resolution of XAS realize in nanometer scale, the stochastic which is own to the electron state of each element in the resist material can be captured by this high-spatial-resolution XAS.

The scattering measurement is benefit for observation of the physical structure. In X-ray region, small angle X-ray scattering (SAXS) is widely used for the physical structure analysis using the X-ray energy of 8 keV in usual.

In this study, soft X-ray scattering employed as a probe light with varied photon energy was employed to study the physical and chemical structures of a tri-block polymer. The scattering signal from the sample includes not only the information of the physical structure but also the information of the chemical structure. And the scattering signal intensity depends on the chemical state near the absorption edge. Wang et al. reported this scattering method of resonant soft X-ray scattering (RSoXS) for the measurement of the triblock terpolymers such as poly(1,4-isoprene-block-styrene-block-(2-vinylpyridine)). The RSoXS is used for the measurement of spatial composition correlations in organic sample [2].

In this study, we have analyzed the physical structure of poly(isoprene-block-styrene-block-(2-vinylpyridine)) (ISP) triblock terpolymer blends. In this paper, isoprene, styrene, and 2-vinylpyridine polymers are represented as I, S, and P polymers, respectively. This terpolymer has cylinder structure of I and P polymers in S polymer. These samples were also measured by the transmission electron microscopy (TEM). The block copolymer consists of two or more covalently bonded polymer chains and self-assembles by microphase separation into a regular microstructure [3]. The 3-component block terpolymer is widely used for controlling morphology with a complicated microphase separated structure [4].

Experiments and Results

● samples

Figure 1 shows the triblock polymer samples with (a) hexagonal packed cylinders and (b) tetragonal packed cylinders, respectively. These sample were prepared by same method for the physical structure observation using TEM. The triblock polymer was packed by surrounding with epoxy resin. Thin packed sample were sliced to a thickness of 400 nm using a microtome. The ultrathin sections were floated on a water and transferred onto a Cu grid with having a center hole of 1.5-mm-diameter.

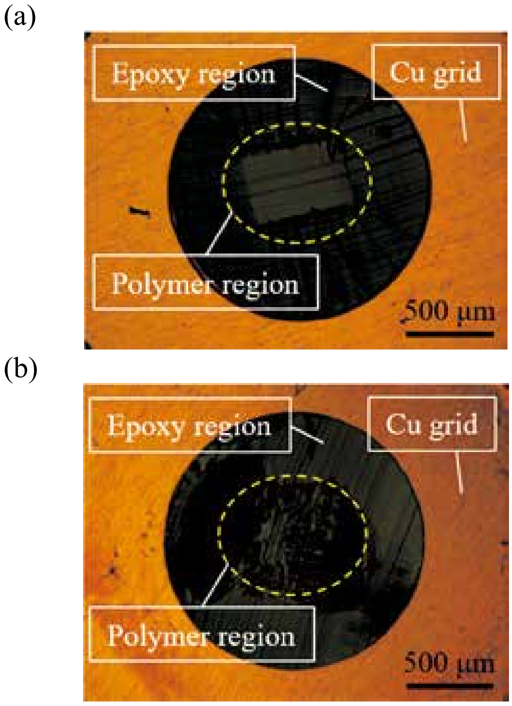

Fig. 1. Photograph of the optical-microscope sample images of ISP triblock copolymers; (a) the hexagonal packed copolymer, and (b) the tetragonal packed copolymer.

- RSoXS method

In this study, we have constructed a RSoXS measurement system at the BL-10 beamline of the NewSUBARU synchrotron light facility. The BL-10 beamline has a bending magnet as a light source, and a monochromator which is a Monk-Gillieson type spectrometer using varied-line-spacing grating with incident slitless design to monochromate the incident photon energy. The photon energy range to expose on a sample is from 60 to 1100 eV. The number of photons estimated by photodiode current at the focal point under the condition of the exit-slit 20 µm is 4×10^9 photons/s at the photon energy of 280 eV. The energy resolution E/ΔE is approximately 2500. The scattering measurement chamber using in this study is installed at 2.1 m downstream from the vertical and horizontal focal points in the beamline. The stage and the CCD camera which we have been used for a EUV microscope described in the paper [5].

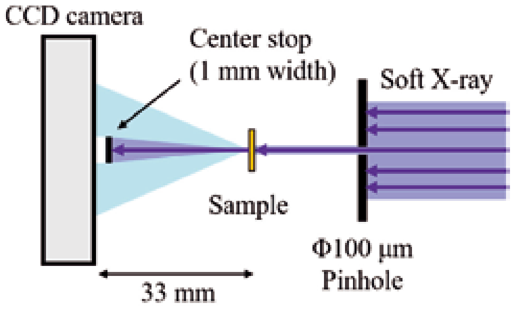

Fig. 2. Schematic diagram of the scattering measurement system which is installed in the BL-10 beamline.

Fig. 2 shows a schematic diagram of the scattering measurement system which is installed at the BL-10 beamline. A ϕ100-µm pinhole was used as an aperture for the soft-X-ray incident beam. The distance from the pinhole to the sample is 30 mm, and the distance from the sample to the CCD camera is 33 mm. The maximum acceptance angle is 24°, which corresponded to q_{max} of 0.59 nm^{-1} at 280 eV.

The scattering light from the sample is recorded by the CCD camera in vacuum. To cut off the direct light with strong intensity, a 1-mm-wide center-stop plate was set in front of the CCD camera.

The scattering angle and pitch of the sample structure are described by the following diffraction equation eq. (1).

$$d\sin\theta = m\lambda \qquad (1)$$

Where d is the pitch of the cylinder structure, θ is the scattering angle, m is the diffraction order, and λ is the wavelength of the incident soft X-ray.

- Hexagonal packed cylinder

Figures 3(a)-(e) show scattering images of the hexagonal packed ISP triblock terpolymer at five photon energies of 280.0, 284.0, 285.6, 288.6, and 300.0 eV, respectively. And in each figure, the contour plots of the light intensity distribution is shown in logarithmic scale.

Figure 3(f) shows a TEM image of this terpolymer. The black circle, the grey circle, and the back white region indicate the I, P, and S polymers, respectively.

In the scattering images, the bright center region indicates scattering light from the incident pinhole. The outer region of this scattered light was blocked with the Cu grid hole. The black rectangle at the center region indicates shadow of the center block plate, which blocked the bright direct beam.

Two scattering signals with the ring-shape were recorded, with ellipse shape, not circle shape. The radius of horizontal direction was smaller than the vertical direction. This ellipse indicates that the sample is stretched along the horizontal direction. In addition, the ring-shape indicates that the domain size of the terpolymer is sufficiently smaller than the beam diameter of 100 μm. This scatter signal is an averaged signal obtained from a small cylinder having a random direction.

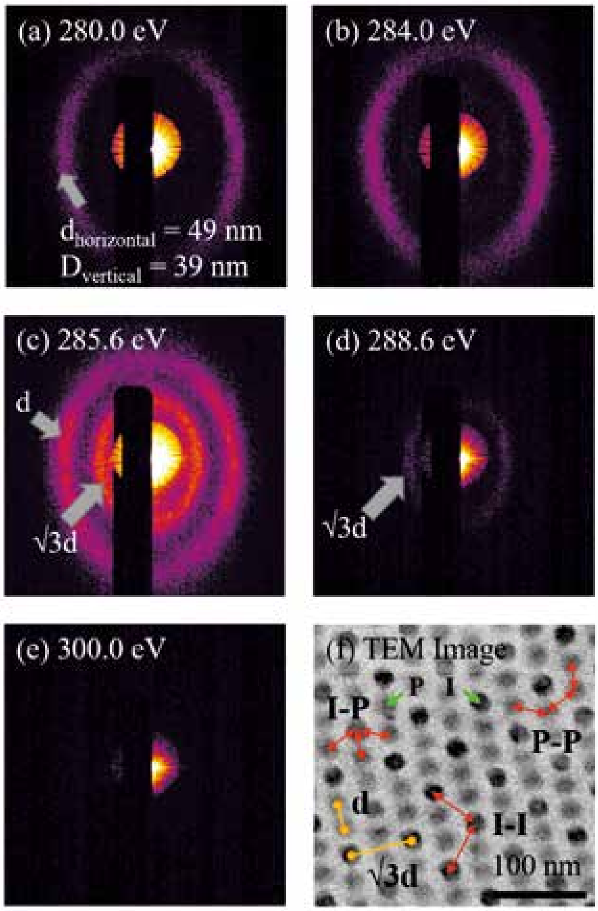

Fig. 3. Scattering and TEM images of the hexagonal packed ISP triblock terpolymer.

The scattering intensity of scattered ring strongly depends on the incident photon energy. The outer ring signals were observed as shown in Fig. 3 (a), (b), and (c), the inner signals were observed as shown in Fig. 3 (c), and (d). At the absorption energy of 285.6 eV which can assigned as π* bonding of benzyl group, the scattering intensity of the two rings were strongest. The d-spacing of the outer ring was estimated to be 49 nm along the horizontal direction, and 39 nm along the vertical direction. The inner ring had √3 times larger pitches. The d-spacing ratio and TEM image indicates that the outer and inner rings corresponded to the scattering from the P-P and I-P physical structures, and I-I physical structure. These structures are shown in Fig. 3(f).

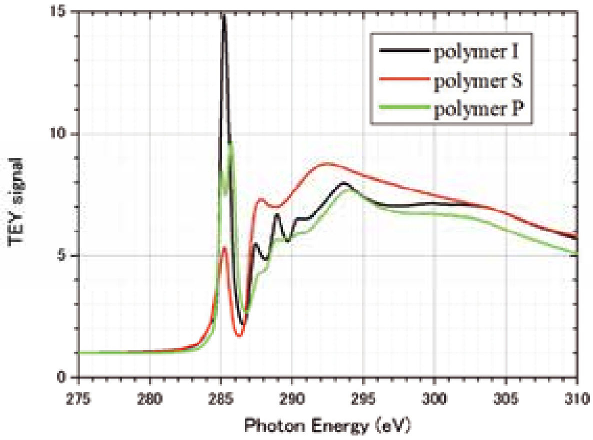

Fig. 4. TEY result around C_K region of three polymers which were coated on Si wafers individually.

Figure 4 shows XAS result of the three polymers coated on Si wafers measured by the total electron yield (TEY) method at the BL-10 beamline described in the paper [7]. The TEY signal depends on the absorption of its sample, where the large TEY signal indicates large absorption. The three polymers which were included in the terpolymers were the I, S, and P polymers. At the photon energy of 280.0 eV, the absorption of all three polymers were small and approximately same. At the photo energy of 284.4 eV, the absorption of the I and S polymers were approximately same, and the P polymer had slightly small absorption. As a result, only the inner scattering ring of the nearest neighbor scattering was observed as shown in Fig. 3(b). At the photon energy of 285.6 eV which can assigned as π* bonding of benzyl group, three polymers had large and different absorption. As a result, both the outer and inner scattering rings were observed. At the photo energy of 288.6 eV, the S and P polymers had approximately same absorption. As a result, only the inner scattering ring was observed, which corresponded to scattering from the I-I physical structure.

Since scattering efficiency depends on not only the absorption but also the refractive index, it is hard to discuss the scattering signal only with the TEY result. However, the refractive index is close related to the absorption, and the scattering intensity was strongly depended on the absorption. At the RSoXS measurement, it is possible to obtain scattering signals distinguishing the polymer types by changing the probe photon energy.

This triblock polymer usually measured by the SAXS. However, the scattering signal includes only the I polymer physical structure in the S and P polymers. For the SAXS measurement, the photon energy is usually 8 keV. The S and P polymer has the same contrast. Thus, it is hard to achieve the P polymer physical structure information.

Figure 5 shows the scattering profiles of the hexagonal packed cylinders observed by seven photon energy conditions. The horizontal axis shows the scattering vector (q), which is shown in Eq. (2).

$$q = \frac{4\pi}{\lambda} sin(\frac{\theta}{2}) \quad (2)$$

The vertical axis shows the scattering intensity at the radial position. Since it is an ellipse rather than a circle, scattering intensity in vertical direction is shown in Fig. 5.

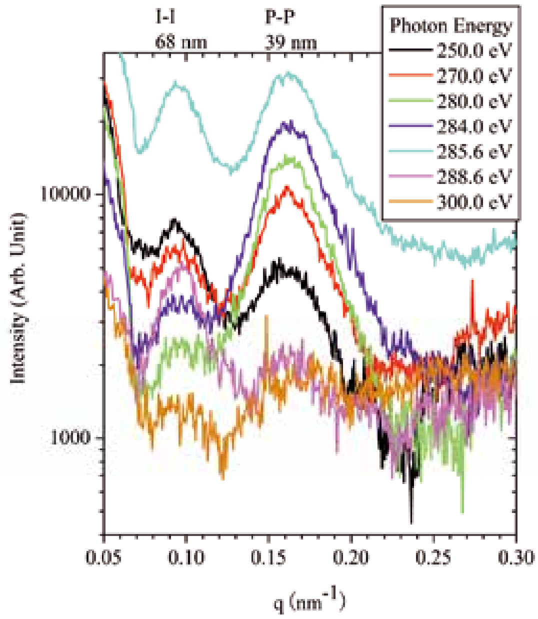

Fig. 5. Radial intensity average obtained by the scattering measurement results of the hexagonal packed ISP triblock terpolymer.

As results, at the seven photon energy from 250.0 eV to 300.0 eV in Fig. 5, there are two peaks of inner and outer ring as shown in Fig. 3(a)-(e) around q = 0.093 nm^{-1} and 0.16 nm^{-1}, where these d-spacing of its physical structure width were 68 and 39 nm, respectively The ratio of these peaks is exactly √3. The scattering intensity strongly depends on the photon energy. The scattering intensity ratio of the outer peak to the inner peak was also changed with varying the photon energy. For example, at the photon energy of 285.6 eV, the ratio was approximately 1, where the scattering signals were due to the P-P, I-P, and I-I polymer physical structures. At the photon energy of 288.6 eV, the scattering signal was mainly due to the I-I polymer physical structures because the intensity ratio was 0.4. The scattering contrast of the P polymer to the base S polymer was small. At the photon energies of 280.0 and 284.0 eV, the ratio was 6. The scattering signal was due to the P-P polymer physical structure. The scattering contrast of the I polymers to the base S polymer was very small. Thus, the RSoXS measurement resolved the I and the P polymer physical structures.

- Tetragonal packed cylinder

Figures 6(a)-(e) show the scattering image of the tetragonal packed ISP triblock terpolymer. In each figure, the contour plots of the light intensity distribution is shown in logarithmic scale. Figure 6(f) shows the TEM image. Figure 7 shows the scattering profiles of the tetragonal packed cylinders observed by seven photon energy conditions.

In the scattering image of Figs. 6(a)-(e), there was no ring-shaped scattering like the hexagonal packed cylinders. Four scattering signals were recorded at each inner and outer region. This non-ring scattering indicates the domain size of this terpolymer was larger than the illumination size of 100 μm. The azimuth angle of the inner scatterings has 45°-difference from that of the outer scatterings. The scattering angle of the outer scatterings was approximately √2 times larger than that of the inner scatterings. The d-spacing of the inner scatterings was estimated to be 59 nm. The d-spacing of the outer scatterings was estimated to be 42 nm, which corresponded to that of the I-I and P-P physical structures.

Since the scattering angle ratio of the horizontal to vertical directions was approximately one, this terpolymer was not stretched. The scattering intensities of the inner four scatterings were symmetric, and asymmetric

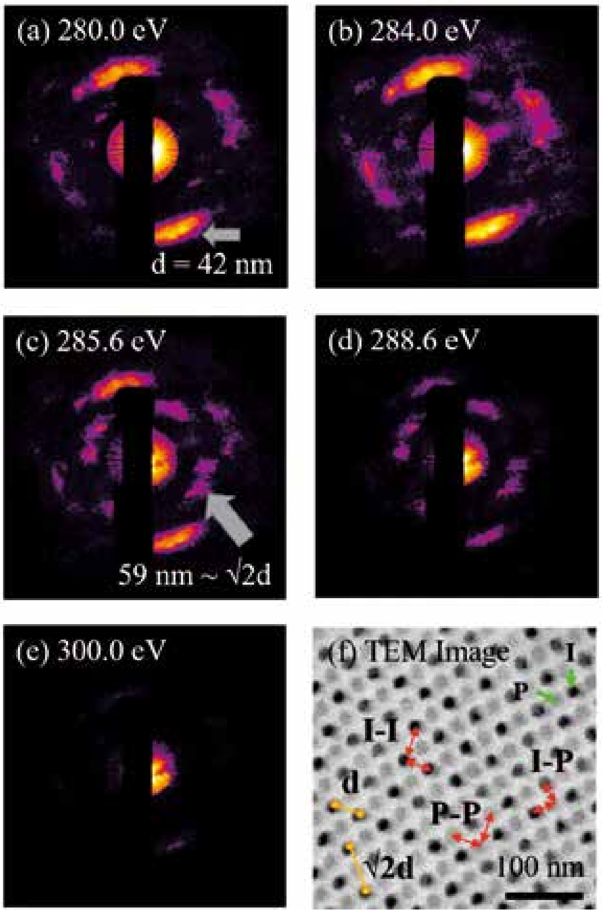

Fig. 6. Scattering and TEM images of the tetragonal packed ISP triblock copolymer.

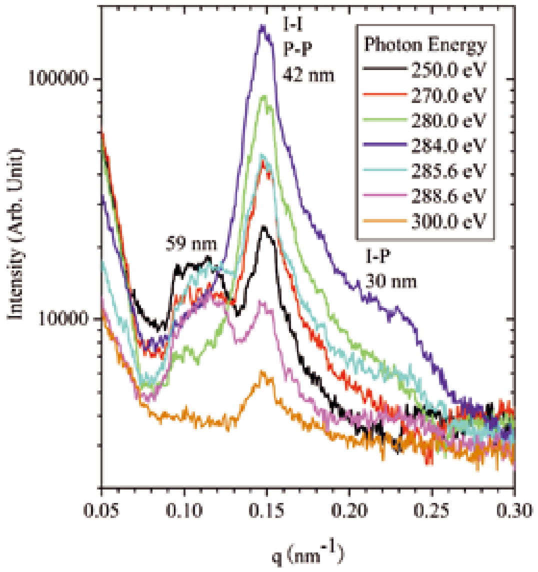

Fig. 7. Radial intensity average obtained by the scattering measurement results of the tetragonal packed ISP triblock terpolymer.

at the outer side. According to the previous hexagonal packed case, the P-P physical structure was observed without the information of the I-I and I-P structures at the photon energies of 280.0 and 284.0 eV. The outer asymmetric scattering signal was due to nearest neighbor the P-P physical structure shown in Fig. 6(f). As a result, microdomain structure of the P polymer would have the lamellar structure, which caused this asymmetric scattering. This structure was not observed in the TEM image.

In the RSoXS, soft X-rays irradiates on a thin film sample, and a scattering signal corresponding to the structure of the sample material and the absorption / refractive index contrast is obtained. By changing the energy of incident light near the absorption edge, the contrast images of the constituent atoms, molecular structure, and chemical state can be obtained. Therefore, it is possible to distinguish each component of blend polymer having close density, and it is a method that can evaluate the structure of each molecule. Especially, it is possible to obtain very strong intensity with repetitive pattern and it is suitable for physical structure analysis of the triblock terpolymer.

Acknowledgement

The author would like to thank Dr. Atsushi Takano for providing the triblock terpolymer samples.

References

[1] K. Emura, T. Watanabe, M. Yamaguchi, H. Tanino, T. Fukui, D. Shiono, Y. Haruyama, Y. Muramatsu, K. Ohmori, K. Sato, T. Harada, and H. Kinoshita, J. Photopolym. Sci. Technol., **27**, 631 (2014).

[2] C. Wang, D. H. Lee, A. Hexemer, M. I. Kim, W. Zhao, H. Hasegawa, H. Ade, and T. P. Russell, Nano Lett., **11**, 3906 (2011).

[3] F. S. Bates, G. H. Fredrickson, Phys. Today, **52**, 32 (1999).

[4] Y. Asai, A. Takano, and Y. Matsushita, Macromolecules, **49**, 6940 (2016).

[5] T. Harada, Y. Tanaka, T. Watanabe, Hiroo Kinoshita, Y. Usui, and T. Amano, J. Vac. Sci. Technol. B, **31(6)** , 06F605-1 (2013).

Total-electron-yield measurements of insulating thick film samples put on conductive substrates

Yasuji Muramatsu and Yukina Tani
Graduate School of Engineering, University of Hyogo

Abstract

We have proposed a new method for soft X-ray absorption measurements of insulating thick films using a total-electron-yield (TEY) method. TEY of insulating paper, cloth, and tape samples put on conductive substrate can be successfully measured in BL10/NewSUBARU. This method enables to easily measure TEY-XANES of insulating film samples whose thickness is several-tens µm.

1. Introduction

The yield of electrons emitted from matter by X-ray irradiation is generally proportional to the X-ray absorption intensity. Thus, photocurrent can flow in electrically conductive matter by X-ray irradiation when matter is grounded. The photocurrent measured in grounded matter is usually called as sample current. Monitoring the sample current during the X-ray energy scanning is easy using X-ray absorption spectroscopy (XAS), which is a total electron yield (TEY) method [1,2]. In particular, the TEY method is commonly used in soft X-ray absorption spectroscopy because the fundamental transmission method for XAS is difficult to apply to soft X-ray absorption measurements.

Although numerous XAS studies have used the TEY method to examine electrically conductive materials, it is generally hard to apply the TEY method to insulating bulk materials because sample charge-ups distort the TEY. To avoid or suppress charge-up effects of insulating bulk samples during X-ray irradiation, bulk samples are often powdered and placed on conductive substrates [3, 4]. The TEY of the insulating powder samples can be easily measured via the sample surface in contact with a conducting substrate. This system effectively monitors the surface sample current of insulating particles, but it requires deconstructive preparations of bulk samples. We have quite recently found another method to easily observe the TEY of insulating bulk thin samples [5]. In this method, insulating thin samples are put on conductive substrates, and the sample current generated by soft X-ray irradiation can be efficiently detected though the backside of the substrate. Such phenomena suggest that electrically conductive paths are induced inside insulating thin samples by soft X-ray irradiation. This paper demonstrates the TEY measurements of insulating thick films such as papers, clothes, and tapes which are put on conductive substrates [6].

2. Experiments

Figure 1 shows insulating thick film samples of papers, wiping clothes, and tapes, which are put on a conductive carbon tape substrate. Label, thickness, and density of the samples are denoted in the Figure. Thickness of these samples are approximately 40 ~ 150 µm. Papers take middle density of 0.46 ~ 0.82 g/cm^3, wiping clothes take lower density of 0.20 ~ 0.23 g/cm^3, and tapes take higher density of 1.0 ~ 1.3 g/cm^3. Sample current of these film samples were measured through the carbon tape substrate during soft X-ray irradiation. Sample current and TEY measurements were performed in BL10/NewSUBARU. Spectral measurements in 200 - 600 eV, C*K*, and O*K* regions.

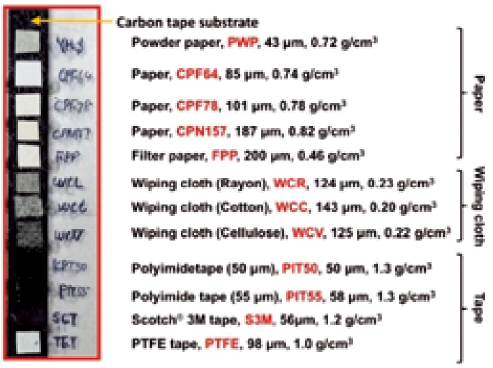

Fig. 1 Insulating film samples of paper, wiping cloth, and tape, which are put on a conductive carbon tape substrate.

3. Results and Discussion

3.1 TEY-Spectra of Thick Film Samples

Figure 2 shows sample current and TEY spectra in the 200 – 600 eV region of the samples. Sample current of paper and tape samples is several pA, and that of cloth samples is several tens pA. It is therefore confirmed that sample current of these thick film samples can be surely measured through the carbon tape substrate. TEY-XAS of them exhibits C*K* and O*K* absorption structures. This clearly shows that XAS of such the insulating thick films can be easily obtained with the TEY method. Absorption intensity in the C*K* region of paper and tape samples is fairly smaller than that in O*K* region. On the other hand, C*K* intensity is larger than O*K* intensity in wiping cloth samples. These results imply that the measured sample current is strongly dependent on the excitation energy and density of the samples. In paper and tape samples, the lower C*K* intensity than O*K* intensity results in the lower energy and higher density. In the wiping cloth samples, the higher C*K* intensity results in lower density.

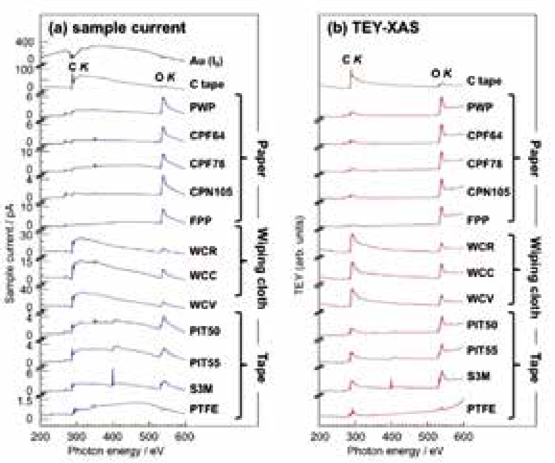

Fig. 2 Sample current (a) and TEY-XAS in the 200 - 600 eV region of the paper, wiping cloth and tape samples.

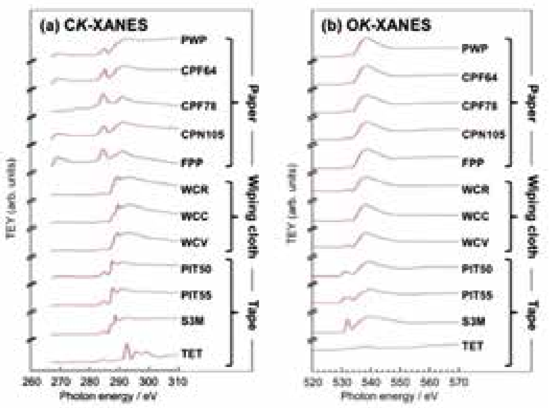

Fig. 3 XANES in the C*K* (a) and O*K* (b) regions of the paper, wiping cloth and tape samples.

Figure 3 shows XANES in the C*K* and O*K* regions of the samples. The C*K*-XANES exhibits different profiles in paper, wiping cloth and tape samples. The O*K*-XANES of them are also clearly observed. It is therefore confirmed that chemical analysis of the insulating thick films can be performed with the TEY method. It is additionally mentioned that the 2nd order of O*K* absorption is little observed in the lower energy region of C*K*-XANES. This means that 2nd order diffraction can be effectively suppressed in BL10/NewSUBARU, which is an advantage for the CK-XANES analysis by using this TEY method.

3.2 Application for Environmental Samples

XANES of environmental dust samples collected on filter papers were directly measured for demonstration of the TEY method. Upper panel of Figure 4 shows a photo of samples. Air monitoring PTFE filter membrane and dust collected on the filter were put on a conductive carbon tape substrate. Lower panel of Figure 4 shows the sample current spectra of the samples. The samples exhibit several pA in the 200 – 600 eV region. Absorption peaks in C*K*, N*K* and O*K* regions are clearly observed in the sample.

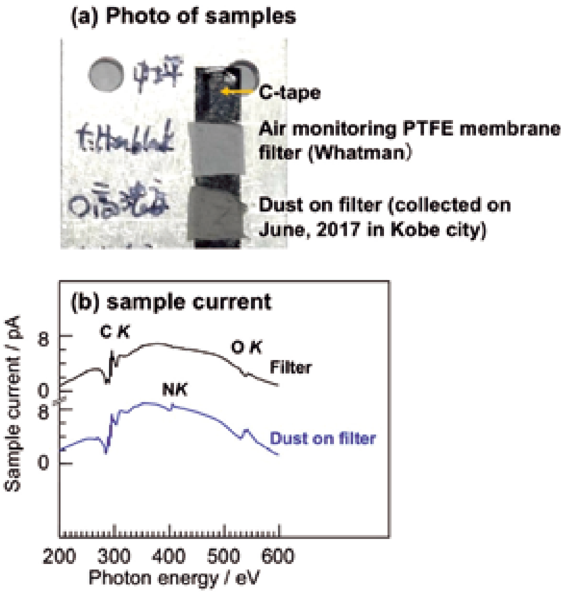

Fig. 4 Upper panel (a) shows a photo of the filter and dust on filter samples put on conductive carbon tape. Lower (b) shows sample current spectra of the filter and dust on filter samples.

Figure 5 shows the XAS or XANES in the 200 - 600 eV, O*K* and C*K* regions of the dust on filter and filter samples, and the spectral difference of (dust on filter) - (filter). The spectral difference in the 200 – 600 eV region clearly shows the C*K*, N*K*, and O*K* absorption peaks of dust. The spectral difference in O*K* region exhibits the π* peak at 530 eV, suggesting the carbonyl oxygen on dust surface. The spectral difference in *CK* region exhibits a small π* peak at 285.5 eV and an intense peak at 288 eV. This suggests that the dust contains small portion of aromatic or unsaturated organic compounds and that oxygenated organic compounds are clearly exist on dust surface. It is therefore confirmed that XANES of environmental samples collected on insulating filters can be directly observed by using the proposed TEY method.

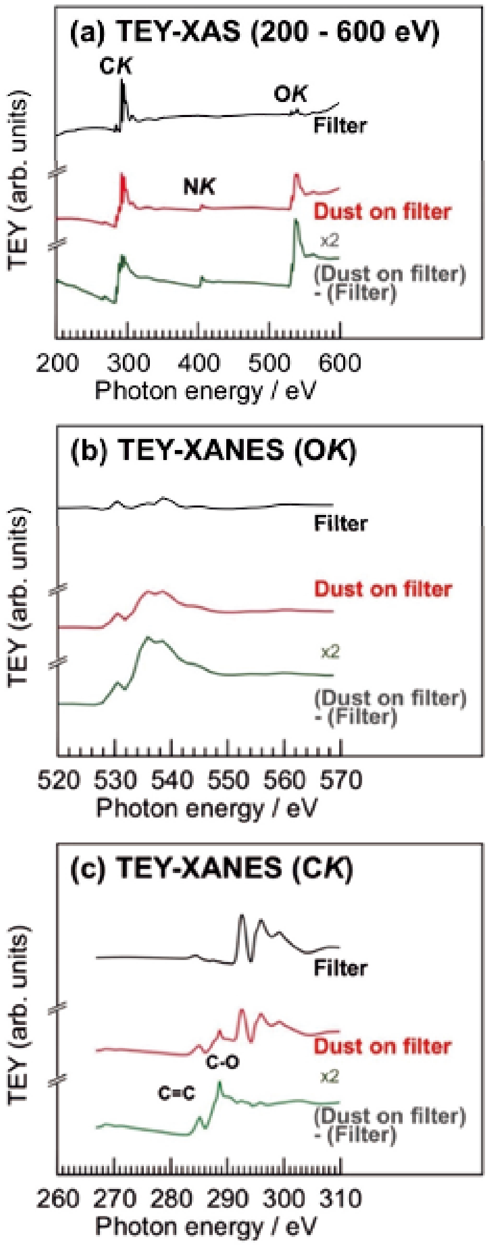

Fig. 5 TEY-XAS in the 200 - 600 eV region (a), and TEY-XANES in the *OK* (b) and *CK* (c) regions of the filter and dust on filter samples. Subtracted spectra of (Dust on filter) - (Filter) are also described in the figures.

4. Conclusion

XANES of insulating thick film samples of paper, wiping cloth, and tape can be successfully measured by using the TEY method in which the insulating samples are put on conductive substrates. For application of the present method, TEY-XANES of environmental dust samples collected on filters can be measured. It is therefore concluded that the proposed TEY method will be a powerful tool for chemical analysis of insulating thick film samples.

References

[1] J. Stöhr, C. Noguera, and T. Kendelewiez, Phys. Rev., B30, 5571-5579 (1984).

[2] J. Stöhr, NEXAFS Spectroscopy (Springer-Verlag, 1996) pp. 118-133.

[3] G. J. Baker, G. N. Greaves, M. Surman, M. Oversluisen, Nucl. Instrum. Meth. in Phys. Res., B97, 375-382 (1995).

[4] H. M. Wang and G. S. Henderson, J. Non-Cryst. Solids, 354, 863-872 (2008).

[5] Y. Muramatsu, The76th Annual Meeting of Analytical Chemistry, Japan, F1010 (2016).

[6] Y. Muramatsu, Y. Tani, Y. Tobita, S. Hamanaka, and E. M. Gullikson, Adv. X-Ray Chem. Anal. Japan, 49, 219-230 (2018).

Chemical analysis of coal tar using soft X-ray absorption spectroscopy

Yasuji Muramatsu and Kosuke Shirai
Graduate School of Engineering, University of Hyogo

Abstract

To characterize coal tar, we have measured XANES in C*K*, N*K*, and O*K* regions of them in BL10/NewSUBARU. Minor components of nitrogen and oxygen can be successfully detected and chemical states of them were estimated with a finger print method. The π^* peak map from C*K*-XANES suggested that the coal tar samples can be identified from the size of aromatic compounds as major components.

1. Introduction

Coal tar is one of the important industrial carbon materials. It is well known that coal tar takes complex structure of aromatic and aliphatic compounds. The compounds have been usually analyzed chromatographic method, infrared (IR) spectroscopy, and NMR [1]. However, local structure of coal tar has not been clearly clarified by using these conventional analytical methods. In this study, we have measured XANES of various industrial coal tar samples to identify the local structure of them.

2. Experiments

Commercially available six coal tar samples (denoted as T1 ~ T6) were used for characterization of coal tar. Coal tar is generally sticky liquid and electrically insulating. Thus, we have prepared thin coal tar samples on gold (Au) substrates; (1) coal tar was dissolved in organic solvent, (2) the solution was dropped on a gold (Au) substrate, and (3) evaporate the solvent.

X-ray absorption spectra (XAS) of tar samples were measured at the XAS system [2-5] in BL10/NewSUBARU, and partially measured in BL-6.3.2/ALS (Advanced Light Source). XANES in the C*K*, N*K*, and O*K* regions were measured with a total-electron-yield (TEY) method. For finger print analysis for N*K*- and O*K*-XANES, reference aromatic compounds having nitrogen and oxygen functional groups were also measured [6,7].

3. Results and Discussion

3.1 XANES

Figure 1 shows XAS in 200 - 600 eV region of tar samples (T1 ~ T6). Each sample can be successfully measured with a TEY method without charge up. All samples exhibit intense absorption at C*K* edge and weak absorption at N*K* and O*K* edges. It is therefore confirmed that small portions of N and O in tar can be detected by TEY-XAS.

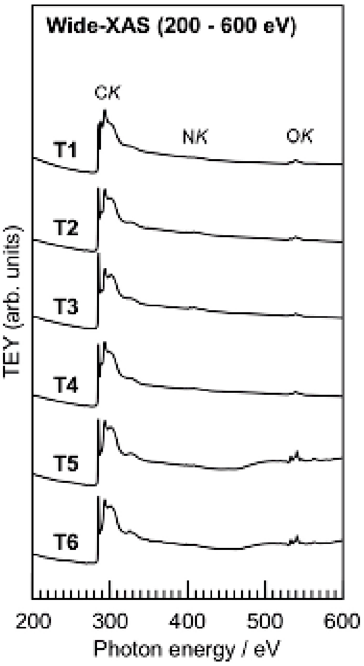

Fig. 1 TEY-XAS in the 200 - 600 eV region of tar samples.

Figure 2 shows the C*K*-XANES. Each tar exhibits π^* peak at 285.5 eV and σ^* peak at 293 eV. Such the profiles suggest that major carbon components of tar are aromatic compounds. Characteristic peaks are also observed at 287~289 eV, which suggests the aliphatic C-C structure. Thus, components of tar can be estimated to be aromatic compounds as major components with aliphatic compounds.

As shown in Figure 1, N is a minor portion in tar. However, N is surely incorporated as shown in N*K*-XANES of Figure 3. The N*K*-XANES exhibit three peaks (denoted as *a* ~ *c*). From the finger-print analysis compared to reference N-having aromatic compounds, the peaks *a* ~ *c* suggest the structures of -NH$_2$ and N in aromatic rings.

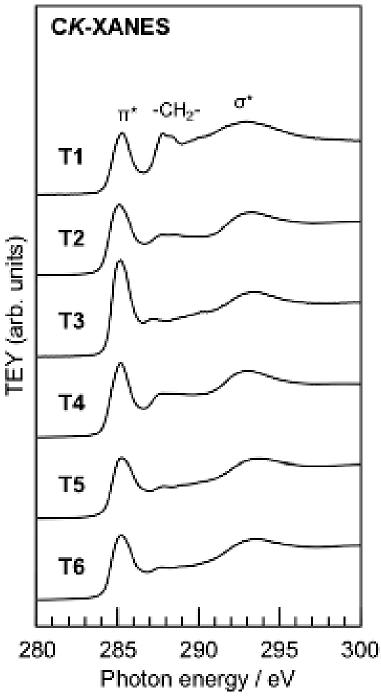

Fig. 2 C*K*-XANES of tar samples.

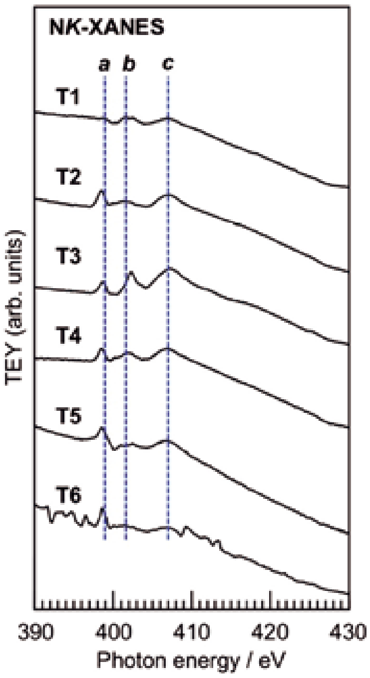

Fig. 3 N*K*-XANES of tar samples.

Figure 4 shows O*K*-XANES. All tar samples exhibit three peaks (denoted as *d* ~ *f*). From the finger-print analysis compared to reference O-having aromatic compounds, the peaks *d* ~ *f* suggest the structures of carbonyl or quinone >C=O and -OH.

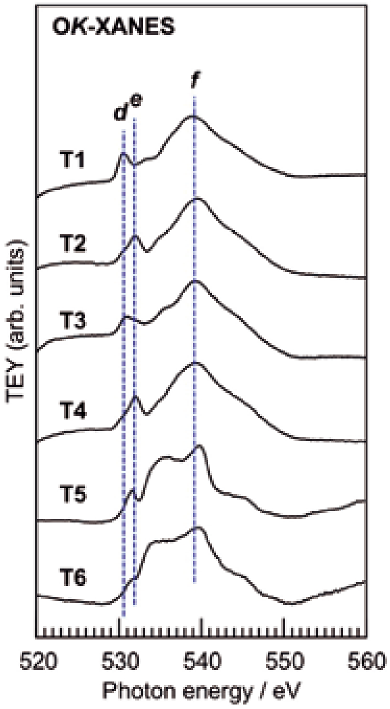

Fig. 4 O*K*-XANES of tar samples.

3.2 Identification of Tar on π* Peak Map

Width and height of π* peak in C*K*-XANES of graphitic carbons are strongly dependent on local structure of hexagonal carbon layers [8]. From the theoretical analysis of π* peak profile in various aromatic compounds and graphitic particles, we have clarified that the relationship between the width and height of π* peak are determined by the edge structure and size of hexagonal carbon structures. Then, we have proposed a unique index "π* peak map" for identification of graphitic carbon structure from the relationship [9].

We have applied the π* peak map to the tar samples. Figure 5 shows the C*K*-XANES of tar with reference HOPG (highly oriented pyrolytic graphite). Subtracted spectra of (Tar) - (HOPG) are also described on XANES. A peak at 284 eV (denoted as *a*) in the subtracted spectra means the wide portion of π* peak of tar compared to HOPG. Thus, peak *a* height is an index for π* peak width. The π* peak map can be plotted with the π*/σ* peak height ratio as the function of peak *a* height. Figure 6 shows the π* peak map of tar samples with the nano-graphite [9] and carbon black. Comparing to the nano-graphite and carbon black, tar samples distributed upper area on them. This suggests that major carbon compounds are polycyclic aromatic hydrocarbons (PAH) in which edge carbon atoms may be more than 50% in all carbon atoms. In tar samples, π* peak height widely distributes in 1.0 ~ 1.5. This also suggests that molecular size of the PAH components distributes in T1~T6.

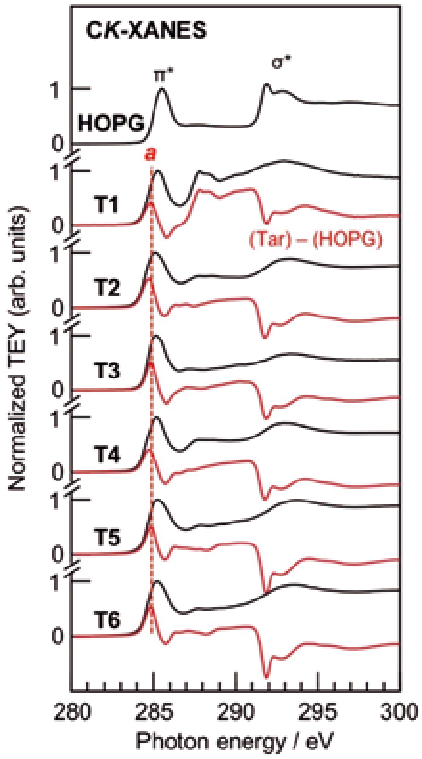

Fig. 5 C*K*-XANES and subtracted spectra between tar and HOPG.

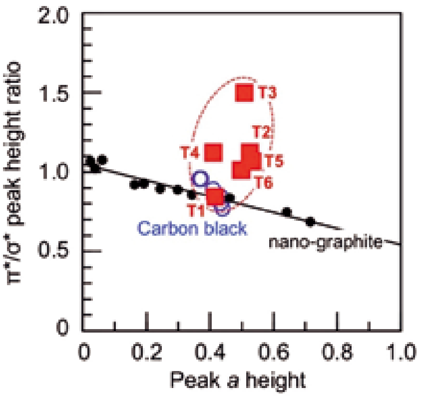

Fig. 6 π* peak map of tar samples compared to nano-graphite and carbon black.

4. Conclusion

We have successfully measured TEY-XANES in C*K*, N*K*, and O*K* regions of tar. Minor portion of N and O can be clearly observed. From the finger print analysis using reference compounds, chemical state of N and O in tar can be estimated. From the π* peak map, major components of tar are confirmed to be PAH in which edge carbon atoms may be more than 50% in all carbon atoms. It is therefore concluded that XANES is a powerful tool for characterization of tar.

References

[1] Z. Sun and W. Zhang, Chin. J. Chem. Eng., **25**, 815-820 (2017).

[2] Y. Muramatsu, A. Tsueda, T. Harada, and H. Kinoshita, Adv. X-ray Chem. Anal., Japan, **43**, 407-414 (2012).

[3] Y. Muramatsu, A. Tsueda, T. Uemura, T. Harada, and H. Kinoshita, Adv. X-ray Chem. Anal., Japan, **44**, 243-251 (2013).

[4] T. Uemura, Y. Muramatsu, K. Nambu, T. Harada, and H. Kinoshita, Adv. X-ray Chem. Anal., Japan, **45**, 269-278 (2014).

[5] T. Uemura, Y. Muramatsu, K. Nambu, D. Fukuyama, M. Kuki, T. Harada, T. Watanabe, and H. Kinoshita, Adv. X-ray Chem. Anal., Japan, **46**, 317-325 (2015).

[6] Y. Muramatsu, S. Ueda, and E. M. Gullikson, TANSO, **236**, 9-14 (2008).

[7] T. Amano, K. Shirode, Y. Muramatsu, and E. M. Gullikson, Jpn. J. Appl. Phys., **52** 041304 (2013).

[8] Y. Muramatsu, T. Ooe, T. Okada, and E. M. Gullikson, Proceedings of the 9th International Symposium on Atomic Level Characterizations for New Materials and Devices '13, ALC'13, 516-518 (2013).

[9] Y. Muramatsu, K. Murayama, and T. Okada, Proceedings of the 10th International Symposium on Atomic Level Characterizations for New Materials and Devices '15, ALC'15, 27p-P-38 (2015).

Sample holder for TEY-XAS measurements in BL10 of extended rubber samples

Yasuji Muramatsu and Yuki Tobita
Graduate School of Engineering, University of Hyogo

Abstract

A new sample holder of the extended rubber has been developed for X-ray absorption measurements in BL10/NewSUBARU. By using the holder, C*K* XANES of extended isoprene rubber (IR) and carbon black (CB) -mixed IR samples were successfully measured. The sample holder enables XANES analysis of rubber from the view point of conformation of rubber polymers.

1. Introduction

Property of rubber is strongly dependent on local structures and interactions among the component compounds such as rubber polymers, carbon black, sulfur, and oxygen. Oxygen is especially an important component for degradation of rubber. However, the component molecules take complex structures and the structure is dependent on extension. To clarify the local structure of rubber by using XANES in BL10/NewSUBARU, we have developed a sample holder for extended rubber. This report briefly describe the holder and XANES of typical rubbers measured by varying the extension.

2. Details of the Holder

X-ray absorption analysis system in BL10 [1-4] uses a sample transfer plate with the size of 75mm^L x 25 mm^W. Thus, the sample holder for rubber should be put on the transfer plate. Left panel of Figure 1 shows the developed rubber holder which fits to the transfer plate. Size of the holder is 75mm^L x 25 mm^W x 8mm^T. The holder is made from aluminum. On this holder, extended rubber sheets can be fixed on side plates with screws. Width of the measuring area on rubber is 13 mm. Three rubber samples can be put on the holder. The sample holder can be rotated around vertical axis as shown in right panel of the Figure. Direction of extension is parallel to the polarization of incident soft X-ray beam. Thus, incident-angle-dependent XANES measurements can be performed to investigate the orientation of the rubber molecules.

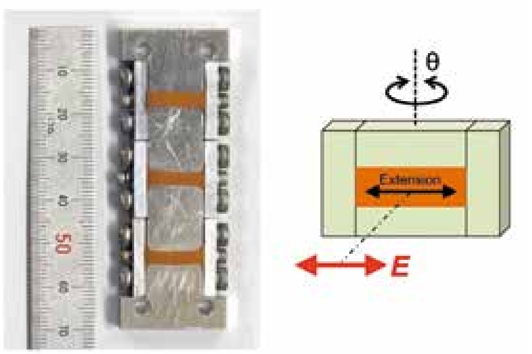

Fig. 1 Left photo shows the newly developed sample holder for extended rubber samples. Right shows the schematic of the holder for incident-angle rotation.

3. XANES of the Extended Rubber Samples

To demonstrate the utility of the holder, XANES of the extended rubber samples were measured in BL10. Rubber samples are typical isoprene rubber (IR) and carbon-black mixed IR (CB-IR), which were supplied from Yokohama Rubber Co., Ltd. Thin sheet samples of IR and CB-IR were extended on the holder with the extension of x1, x2, and x3. Incident angle (θ) was also varied to 90 (normal incidence), 54.5 (magic angle) and 30 degrees. XANES in the C*K* region can be measured with a total electron yield (TEY) method by monitoring sample current through the holder and transfer plate.

Figure 2 shows the incident-angle-dependent C*K*-XANES of the extended IR and CB-IR samples. IR and CB-IR samples exhibit the π* peak at 285.5 eV, σ* peak near 293 eV, and peaks at 287 - 289 eV. The π* peak reflect unsaturated bonds in IR molecules. The peaks at 287 - 289 eV suggest the saturated C-C bonds. In both IR and CB-IR, π* peak height depends on extension. This suggests that conformation of unsaturated bonds can be changed by extension. Figure 3 shows the π* peak height as the function of extension. The π* peak height of IR decreases as the extension increases. However, behavior of the π* peak height of CB-IR is different from IR. This suggests that conformation and local structure of unsaturated bonds in IR polymers are strongly dependent on CB particles.

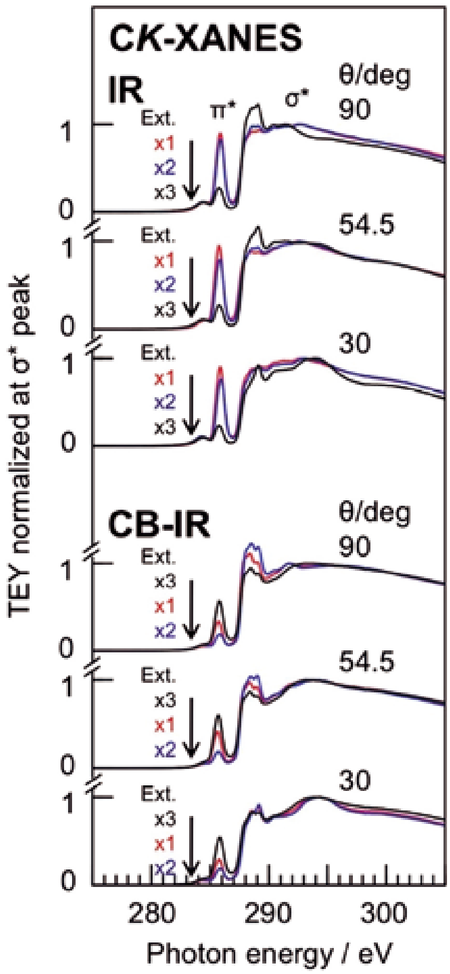

Fig. 2 Incident-angle-dependent *C**K*-XANES of the extended IR and CB-IR.

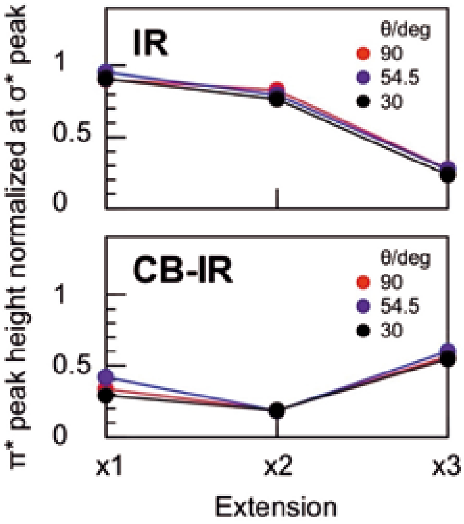

Fig. 3 Extension-dependent π* peak heights of IR and CB-IR.

Figure 4 shows the π* peak heights of the extended IR and CB-IR as the function of $\cos^2\theta$. As mentioned in Figure 3, π* peak height depends on extension in both IR and CB-IR. However, the π* peak height is not dependent on incident angle. This means that unsaturated bonds in extended rubber are not oriented in the sample plane.

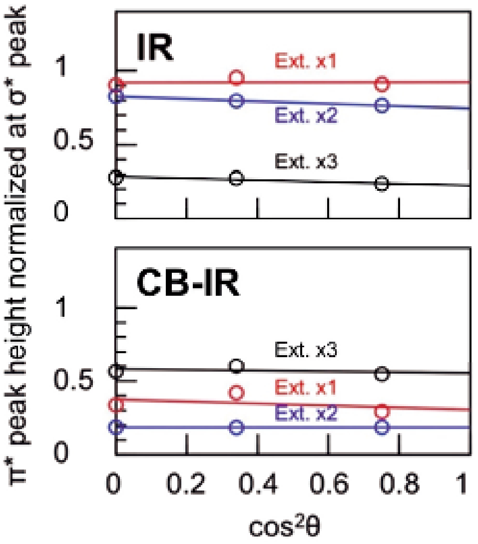

Fig. 4 The π* peak heights of the extended IR and CB-IR as the function of $\cos^2\theta$.

4. Conclusion

Sample holder for extended rubber samples were developed and XANES measurements of the extended rubbers can be successfully demonstrated. By using the holder, XANES analysis of the rubber can be performed by varying extension and incident angles in BL10.

References

[1] Y. Muramatsu, A. Tsueda, T. Harada, and H. Kinoshita, Adv. X-ray Chem. Anal., Japan, **43**, 407-414 (2012).

[2] Y. Muramatsu, A. Tsueda, T. Uemura, T. Harada, and H. Kinoshita, Adv. X-ray Chem. Anal., Japan, **44**, 243-251 (2013).

[3] T. Uemura, Y. Muramatsu, K. Nambu, T. Harada, and H. Kinoshita, Adv. X-ray Chem. Anal., Japan, **45**, 269-278 (2014).

[4] T. Uemura, Y. Muramatsu, K. Nambu, D. Fukuyama, M. Kuki, T. Harada, T. Watanabe, and H. Kinoshita, Adv. X-ray Chem. Anal., Japan, **46**, 317-325 (2015).

Deterioration Analyses of Polymer Thin Film

Hideo Kobayashi[1], Yosuke Azuma[1], Yasuko Mitsushita[1], Shogo Suehiro[1],
Sohta Hamanaka[2], Keigo Yoshida[2], Yuki Tobita[2], and Yasuji Muramatsu[2]

[1] Sumika Chemical Analysis Service, Ltd.,
1-135, Kasugade-Naka 3-chome, Konohana-ku, Osaka 554-0022, Japan
[2] Graduate School of Engineering, University of Hyogo,
2167, Shosha, Himeji, Hyogo 671-2280 Japan

Abstract

Usage environments affect the surface of polymers used in automobiles, home appliances, and other products. We conducted the deterioration analyses of polyamide and polybutylene terephthalate films by using soft X-ray absorption spectroscopy at BL10/NewSUBARU. In this report, we discuss the changes in the molecular structure and molecular orientation of the surface of these polymers due to heat deterioration.

Introduction

Polymers are widely used in many products, such as automobile, home appliances. As for automobile, many of the parts, such as interior and exterior decors are made from polymers. These polymers continue to deteriorate from the surface by UV and heat.

Soft X-ray is useful for surface analysis and total electron yield (TEY) method makes it possible to analyze insulating samples. We have studied about materials used for organic light-emitting diodes so far. However, polymers are difficult to analyze due to their poor electrical conductivity and complex structures.

The purpose of this study is to analyze polymer deterioration by using soft X-ray absorption spectroscopy (XAS) with TEY method at BL10/NewSUBARU.

Experiments

1. Deterioration analysis of polyamide using chemical bonding state

Polyamide (PA) was cut to 1.5 µm thickness by microtome. In order to examine deterioration caused by heating treatment, heat-treated PA film at 140°C over 50 hours and untreated film were measured by XAS. XAS measures were performed across carbon *K*-edge, nitrogen *K*-edge and oxygen *K*-edge (C*K*, N*K* and O*K*) with TEY. The incident angle (θ) of soft X-ray was tuned to 90°.

2. Deterioration analysis of polybutylene terephthalate using molecular orientation

Polybutylene terephthalate (PBT) was cut to 1.5 µm thickness by microtome. In order to examine deterioration caused by heating treatment, heat-treated PBT film at 180°C over 6 hours and untreated film were measured by XAS. XAS measures were performed across C*K* and O*K* with TEY. To examine the molecular orientation, the incident angles of soft X-ray were tuned to 90°, 54.5°, and 30°.

Results and Discussion

1. Deterioration analysis of polyamide using chemical bonding state

Figure 1 shows X-ray absorption near-edge structure (XANES) for C*K*-edge of untreated PA and heated PA. These spectra clearly show that the peak positions were different around 293 eV. From C*K*-XANES, spectral analysis with DV-Xα, this difference is considered to be the result of cutting and random recombination of CO-NH bond by heating. XAS is an effective measure to surface deterioration, since detection depth of XAS is nano-order.

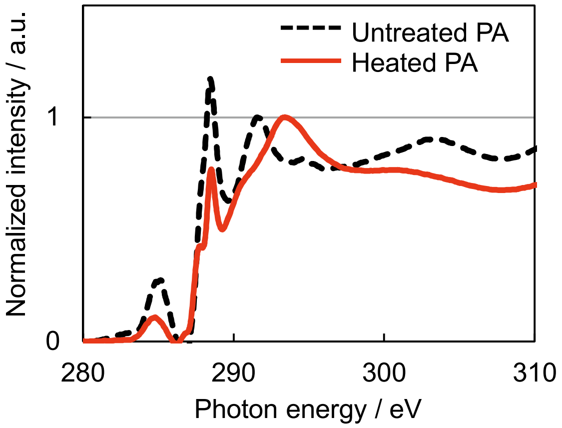

Figure 1. C*K*-XANES spectra of heated PA and untreated PA. The difference of peak positions around 293 eV is considered to be the result of cutting and random recombination of CO-NH bond by heating.

2. Deterioration analysis of polybutylene terephthalate film using molecular orientation

No difference in XANES was observed between untreated PBT and heated PBT measured at $\theta = 54.5°$.

Figure 2 shows the θ-dependent C*K*-XANES of PBT samples. The spectra were taken at incident angles of 30° ~ 90°, which were normalized by σ* peaks at 294 eV. PBT samples exhibit strong θ-dependence of the π* peak intensity at 285 eV, exhibiting minimum at $\theta = 30°$, and maximum at $\theta = 90°$. This tendency indicates that π bond is horizontally-oriented.

To estimate orientation angles, normalized intensities of π* peak were plotted in Figure 3. The angle (α) between the perpendicular π* orbital to the substrate surface and the molecular plane was calculated according to the method of previous study[1]. The calculation gave α = 48° for untreated PBT and α = 41° for heated PBT. It is speculated that this change of α was caused by rearrangement of PBT with annealing.

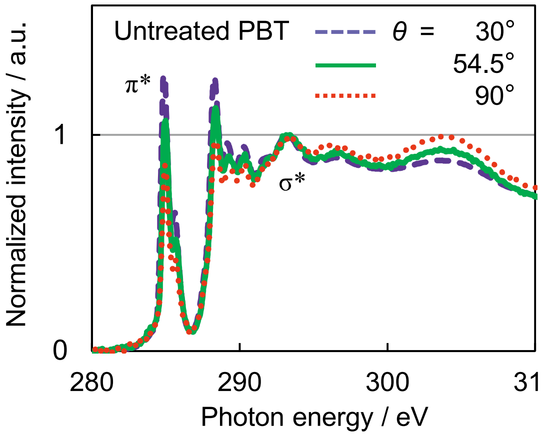

Figure 2. Incident angle dependency of XANES for untreated PBT. These spectra were normalized by σ* peak at 294 eV. The tendency of π* peak intensity indicates that the orientation of π bond is horizontal to PBT surface.

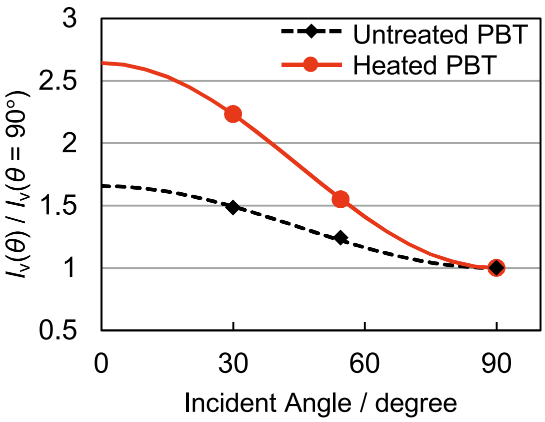

Figure 3. Molecular orientations of untreated PBT and heated PBT. Plots are experimental data and curve lines are calculated data [1].

Reference

[1] F. Zheng, B. N. Park, S. Seo, P. G. Evans, F. J. Himpsel, J. Chem. Phys., **126**, 154702 (2007).

Crystallographic orientation of graphite along activated surface of iron particle via mechanochemical process

Satoshi Motozuka[1], Keigo Yoshida[2], Sota Hamanaka[2] and Yasuji Muramatsu[2]

[1]Department of Mechanical Engineering, Gifu National Colledge of Technology, Gifu, Japan
[2]Graduate School of Engineering, University of Hyogo, Himeji, Japan

Abstract

This study aims to examine crystallite orientation of graphite particles along mechanochemically prepared surfaces on iron particles using angle-dependent C K-edge X-ray absorption near edge structure (XANES) spectroscopy at the BL10 beamline of the NewSUBARU synchrotron radiation facility. Two types of iron surfaces, bare iron and iron oxide, were mechanochemically prepared on iron particle surfaces using a ball-milling process under ambient atmosphere and Ar-3%H_2 atmosphere, respectively. During milling, iron particles were plastically deformed and their shape changed from granular to platelet. Simultaneously, milled graphite particles adhered onto the platelet surface of the iron particles. The angle-dependent XANES spectra revealed that the mechanochemically prepared surfaces affect the orientation of the basal plane of the graphite particle adhering to them.

Introduction

Mechanochemical surface treatment is a powerful tool to modify a solid state and to introduce new defect states that are unachievable by other means [1]. Since the defective structure is an unstable or metastable state, the structure will interact with surrounding materials. In this study, bare iron and iron oxide surfaces with defect structures were achieved via mechanochemical processing using a ball-milling method. The configuration interaction between the surfaces and graphite particles present in the milling vessel as a mechanochemical reactor were investigated using X-ray absorption near edge structure (XANES) measurements at the BL10 beamline of the NewSUBARU synchrotron radiation facility.

Experimental

Water-atomized iron particles (ML35N, Kobe Steel Co., Ltd., D_{50} = 125.0 μm, purity >99.8%) and graphite powder (UCP, Nihonkokuenkogyo Co., Ltd., average diameter: ca. 10 μm, purity >99%) were processed using ball-milling. The iron (5 g) and graphite (0.035 g) particles were placed in a stainless steel vessel, and 20 steel balls were added as the milling medium. The vessel was mounted on a centrifugal ball mill and swung at 59.1 rad/s for 1.0 h. The vessel was surrounded by a water jacket to suppress the heat generated by milling. Milling was conducted under ambient atmosphere, and another mixture of iron and graphite particles were milled under an Ar-3%H_2 atmosphere. Although the measurement system used in this work cannot confirm due to air exposure before the measurement, bare iron and iron oxide surface would be formed on the iron particles milled in each atmosphere during milling.

XANES measurements were conducted at beamline BL10 of the NewSUBARU facility at the University of Hyogo. XANES spectra at the C K-edge region were collected via the total electron yield method to investigate the crystal orientation of graphite on the milled iron particles. The milled samples were embedded in indium plates using a spatula. As shown in Figure 1, the milled samples were gradually deformed and their shape changed from granular to platelet during milling. Therefore, when the particles were pressed against the indium plate by the spatula, the platelet particles spontaneously oriented with their surface parallel to the indium plate surface. The indium plate samples could be rotated around a vertical axis to change the angle of incidence of the SR to the sample surface.

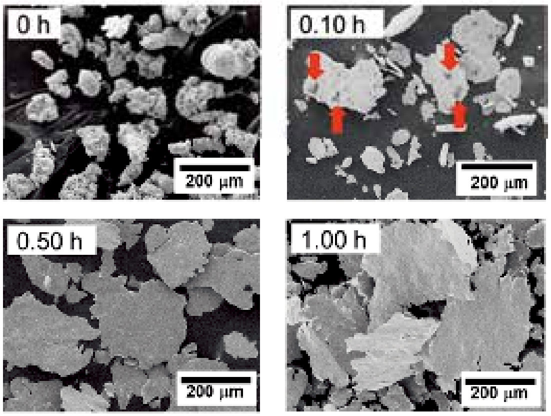

Fig. 1 Representative SEM images of iron particles milled for 0, 0.10, 0.50, and 1.00 h under ambient atmosphere. Red arrows indicate

graphite particles adhered to the iron particles

Results and discussion

Figures 2(a) and 2(b) shows C K-edge XANES spectra of iron powder milled under ambient and Ar–H$_2$ atmospheres, respectively, as a function of glazing angle θ of the SR (see the insets of Figure 2(a) and (b)). Sharp peaks observed at 284.8 eV were assigned to transitions from C 1s orbitals to the unoccupied π* orbitals originating from the basal plane of the graphite. For comparison, iron particles were milled in the absence of graphite and the spectrum of the milled iron particles did not show the peak at 284.8 eV. Therefore, the peak at 284.8 eV was assigned to graphite milled with iron particles. With a decreasing in glazing angle, the relative intensity of the π* peak increased gradually in the spectra of both samples. However, the angle dependency of the relative intensity of the π* peak differed, indicating a difference in orientation strength of the graphite basal plane on the iron surfaces.

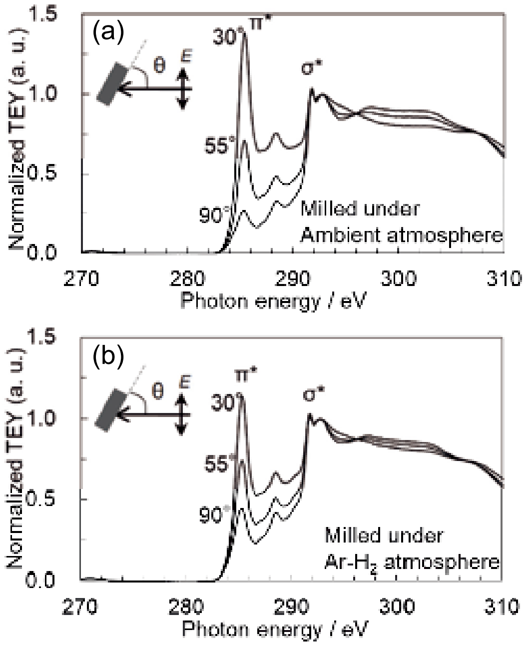

Fig. 2 Incident-angle-dependent C *K*-edge XANES spectra of iron/graphite composite particles milled under (a) ambient and (b) Ar-H$_2$ atmospheres.

Figure 3 shows the π*/σ* peak ratios as a function of cos$^2\theta$ for highly oriented pyrolytic graphite (HOPG), the graphite, iron particles milled under ambient and Ar–H$_2$ atmospheres, and carbon black, which has no crystal orientation. According to the dipole selection rules, the peak intensity associated with the π* states follows a cosine-squared dependence with the glazing angle between incident light and the π bonds, whereas σ* states are insensitive to the angle of incidence of the light [3]. Therefore, the π*/ σ* peak ratios in the spectra of HOPG and carbon black show the strongest and weakest angle dependency, respectively. The ratio of the iron particles milled under an Ar–H$_2$ atmosphere shows a stronger dependency than that of the iron particles milled under ambient atmosphere. These findings indicate that the mechanochemically prepared samples affect the crystallographic orientation of the graphite on their surface.

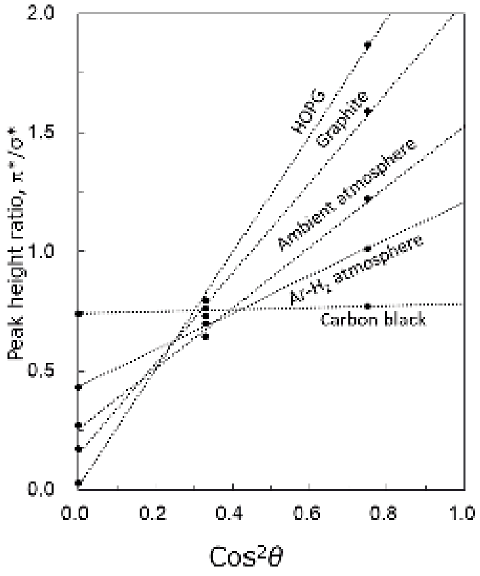

Fig. 3 The π*/σ* peak height ratio in the spectra of HOPG, graphite, and carbon black plotted as functions of cos$^2\theta$.

Frictional force on the milled iron particles was measured using a lateral modulation friction force microscope [4]. The frictional force on the surface of the iron milled in Ar–H$_2$ atmosphere is higher than that of the iron milled in ambient atmosphere, although the data are not shown here. The results obtained from XANES measurements revealed that the mechanochemically prepared iron surface affects the crystallographic orientation of graphite, and graphite orientation is known to play an important role in determining its lubricating behavior.

References

[1]M. K. Beyer, H. Clausen-Schaumann, Chem. Rev. **105**, 2921-2948 (2005).
[2] R. A. Rosenberg, P. J. Love, V. Rehn, Phys. Rev. B **33**, 4034 (1986).
[3]J. Kikuma, BP, Tonner, J. Electr. Spectrosc. Relat. Phenom. **82**, 53-60 (1996).
[4]S. Miyake, M. Wang, S. Ninomiya, Surf. Coat. Technol., **200**, 6137-6154 (2006).

C-, N-, O-XANES analyses of complex organic matter produced by laboratory simulations of aqueous alteration in meteorite parent bodies

Yoko Kebukawa[1], Shusuke Misawa[1], Shinya Asano[1], Yasuji Muramatsu[2], Sohta Hamanaka[2], Yuki Tobita[2], Isao Yoda[3], and Kensei Kobayashi[1]
[1]Yokohama National University, [2]University of Hyogo, [3]Tokyo Institute of Technology

Abstract

We conducted C, N, O *K*-edge X-ray absorption near edge structure (XANES) analyses at BL10, NewSUBARU for complex suites of organic compounds synthesized by simulating experiments for aqueous alteration in meteorite parent bodies. Mixture of formaldehyde and ammonia solutions were irradiated by gamma-ray or heated at 80-150 °C, to evaluate the effects of irradiation and heating in the meteorite parent bodies during aqueous alteration. The C-, N-, O-XANES characteristics of the reaction products were different between gamma-ray irradiation and heating, and thus indicated that both have contributed for formation of diverse organic compounds.

Introduction

Primitive meteorites, such as carbonaceous chondrites contain a few wt.% organic matter. The most of organic carbon (>70 wt.%C) exists as in the form of solvent insoluble organic matter (IOM) with complex macromolecular structures. Rest of the organic carbon is in the form of solvent extractable organic compounds that include tens of thousands of different molecular compositions, with possibly millions of diverse structures [1]. Some of them, such as amino acids and nucleobases could have been contributed to the emergence of life in the early earth. The origins and formation processes of these diverse extraterrestrial organic matter were not well constrained.

Cody et al. [2] proposed IOM formation via formose reaction starting with formaldehyde and glycolaldehyde during aqueous activity in the small bodies. Additional hydrothermal experiments showed that ammonia enhanced the yields of IOM like organic matter [3] and productions of amino acids [4].

The most effective heat source during aqueous alteration is considered to be the decay of short-lived radioactive nuclides such as ^{26}Al [5]. We have been evaluating effects of gamma-ray from decay of short-lived radioactive nuclides on formation of amino acids that are recovered after acid hydrolysis of experimental products. Here we analyzed the reaction products from gamma-ray irradiations which contain precursors of amino acids, using C, N, O *K*-edge X-ray absorption near edge structure (XANES) spectroscopy at BL10, NewSUBARU.

Experimental

Mixtures of water, formaldehyde and ammonia in ratio of 100 : 5 : 5 (mol) simulating primordial materials in comets and asteroids were irradiated by gamma-ray (up to 45 kGy) using ^{60}Co gamma-ray source at Tokyo Institute of Technology. Mixtures with same compositions were heated under various temperatures (80-150 °C) for comparison. The experimental products were dried on Au plates and analyzed using C-*K*, N-*K*, O-*K* X-ray absorption near-edge structure (XANES).

Results

C-XANES spectra of the reaction products showed peaks at 284.0 eV assigned to alkenes, 286.0 eV assigned to ketones, 287.0 eV assigned to phenols and/or aliphatics, 288.8 eV assigned to carboxyls and/or esters, and 290.0 eV assigned to carbamoyls and/or carbonates (Fig. 1). N-XANES spectra of the reaction products showed peaks at around 399 eV assigned to imines, and around 401 eV assigned to amides (Fig. 2).

The gamma-ray irradiation products contain more alkenes and less O-bearing compounds compared to products from heating experiments. The results indicated that organic compounds formed by the gamma-ray irradiation to the formaldehyde and ammonia water solutions were significantly different from those produced by heating, thus the reaction mechanisms would be different between gamma-ray irradiation and heating. N-XANES showed that all products contain amides, and thus these amide bonds likely produce amino acids by acid hydrolysis.

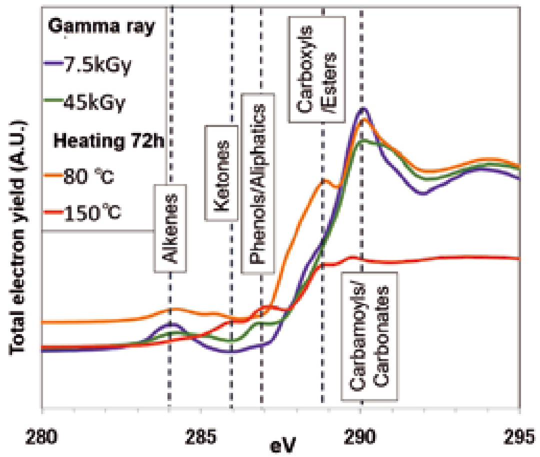

Fig. 1 C-XANES of the products from gamma ray irradiation and heating of formaldehyde and ammonia water solutions.

(a) Gamma ray

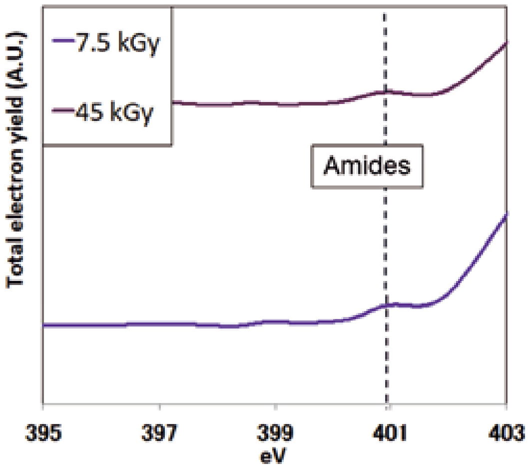

(b) Heating 72h

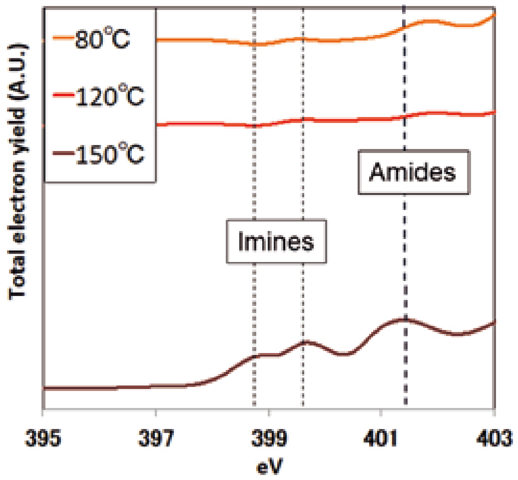

Fig. 2 N-XANES of the products from (a) gamma ray irradiation and (b) heating of formaldehyde and ammonia water solutions.

Conclusions

We successfully obtained functional group analysis of laboratory synthesized organic matter simulating aqueous alteration of meteorite parent bodies using C,N,O-XANES at BL10/NS. In addition to other analyses including infrared spectroscopy and mass spectrometry, these results will help to understand nature and chemistry of the complex organic matter synthesized during aqueous alteration.

References

[1] P. Schmitt-Kopplin, Z. Gabelica, R. D. Gougeon, A. Fekete, B. Kanawati, M. Harir, I. Gebefuegi, G. Eckel, N. Hertkorn, PNAS, **107**, 2763 (2010).

[2] G. D. Cody, E. Heying, C. M. O. Alexander, L. R. Nittler, A. L. D. Kilcoyne, S. A. Sandford, R. M. Stroud, PNAS, **108**, 19171 (2011).

[3] Y. Kebukawa, A. L. D. Kilcoyne, G. D. Cody, The Astrophysical Journal **771**, 19 (2013).

[4] Y. Kebukawa, Q. H. S. Chan, S. Tachibana, K. Kobayashi, M. E. Zolensky, Science Advances, **3**, e1602093 (2017)

[5] A. J. Brearley, In Meteorites and the Early Solar System II (eds. D. S. Lauretta and J. H. Y. McSween), pp. 587-624 (2006).

On-chip Synthesis of Ruthenium Complex by Microwave-Induced Reaction in a Microchannel Coupled with Post-Wall Waveguide

Yuichi Utsumi[1], Akinobu Yamaguchi[1], and Mitsuyoshi Kishihara[2]
[1]Laboratory of Advanced Science and Technology for Industry, University of Hyogo
[2]Okayama Prefectural University

Abstract

We demonstrate the on-chip synthesis of a ruthenium complex based on a microwave-induced reaction in a microchannel coupled with a post-wall 24.15 GHz waveguide. The chip structure for continuous microwave irradiation of solvents and reactants comprises a post-wall waveguide and a microchannel that enters and exits the waveguide by passing between the metallic posts. After microwave irradiation of the microfluidic channel, the specific fluorescence emission spectrum of Tris (2,2'-bipyridyl) ruthenium(II) is observed.

Introduction

Microwave heating is recognized as the leading method for inducing chemical synthesis with very high reaction rates and yields [6]. These advantages are due to the specific effects of microwave radiation on molecular motion (for example, ion migration and dipole rotation), which accelerates the reaction steps. To obtain multiple sequential and combinatorial chemical reactions with a small amount of source reagents and products in a reduced-size system, a promising approach is lab-on-a-chip (LOC) and microfluidics including microreactor technology. . However, by microwave heating combined with microfluidics, extremely high reaction rates and yields should be possible in a more sequentially integrated chemical-synthesis platform that offers extremely precise control of the reaction. Unfortunately, few reports exist on microreactors wherein chemical and biochemical reactions are induced by microwaves. To address this issue, we demonstrate in the present work the on-chip synthesis of a ruthenium complex achieved by a microwave-induced reaction in a microfluidic channel inside a post-wall waveguide designed to confine 24.15 GHz microwave radiation.

In this work, we propose a chip-size structure that allows continuous microwave irradiation to drive radiation-induced chemical synthesis. The structure consists of a post-wall waveguide and a microchannel that passes between the metallic posts. The temperature of water, ethanol, acetyl acetone, etc. under microwave irradiation are examined both numerically and experimentally by considering microwave sources of approximately 3 W. We also describe the on-chip synthesis of a ruthenium complex based on microwave-induced reactions in a microchannel inside a 24.15 GHz post-wall waveguide.

Experiments

Based on the design considerations, we fabricated a micro chemical chip for microwave-induced synthesis and measured the water temperature during microwave irradiation. Figure 1 shows the fabricated microreactor chip, which comprised three 1.0-mm-thick sheets of PTFE stacked to form the microfluidic channel. Finally, sub-miniature type A (SMA) connectors were attached for use as input and output ports. For impedance matching, a 50 Ω dummy load was connected to the output port. The curved microfluidic channel was fabricated by machining the central PTFE sheet, and a 1.0-mm-internal-diameter PTFE tube was laid in the microchannel to assist the flow of reagent into the channel. The water temperature was measured with an optical-fiber microscope (FS100-2M, Anritsu-Meter Co., Ltd.) under 24.15 GHz microwave irradiation with a power of 0.7 and 1.2 W. In this work, the microwave radiation was produced by amplifying the output of a 24.15 GHz Gunn oscillator up to 0.7 and 1.2 W. An isolator was inserted to prevent the microwave power from returning to the amplifier. . When inputting 3.0 W of microwave power, the temperature increases to 75.9 °C.

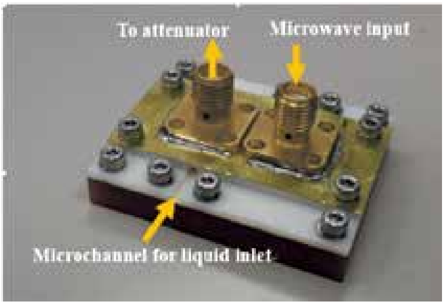

Fig.1 Photograph of fabricated structure of microchip of which microchannel is embedded in the post-wall waveguide.

Results and discussion

The experimental results indicate that the solvent in the microfluidic channel is heated by microwave irradiation with an input power of about 3.0 W or less. The present configuration of the microfluidic channel and post-wall waveguide is suitable for heating several microliters of solvent, so this assembly qualifies as a chip-size microreactor. Next, we synthesized tris(2,2’-bipyridine) ruthenium(II) perchlorate trihydrate ($[Ru(bpy)_3](Cl_4)_2 \cdot 3H_2O$) in this microreactor by using the following microwave irradiation induced chemical reaction.

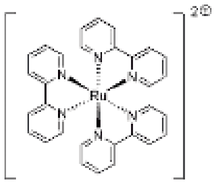

$$RuCl_3 \cdot 3H_2O + bpy \rightarrow Ru(bpy)_3{}^{2+}$$

The microchip for this synthesis was prepared as described above, and the microwave frequency and power were 24.15 GHz and 3.0 W. The irradiation time was 120.0 or 600.0 s, and an optical-fiber sensor was used to monitor the temperature of the microchannel during microwave irradiation. The temperature was fixed at 70 °C for this synthesis procedure. After the synthesis induced by microwave irradiation, the initially green solution becomes orange red. The fluorescence emission spectra of Tris(2,2'-bipyridyl)ruthenium(II) dissolved in water was acquired by using USB2000 and DH2000 instruments (Ocean Optics Co. Ltd.).

The mixture of $RuCl_3 \cdot 3H_2O$(0.25g;1.03 mmol) and 2,2’-bipyridine (bpy) (0.797g;5.09 mmol) in ethylene glycol (11.1 ml) was preparedas the starting materials for the synthesis of ($[Ru(bpy)_3](Cl_4)_2 \cdot 3H_2O$). The irradiation time was 120.0 s. The fluorescence peak of the products appears at 607 nm, which is the specific peak of Tris(2,2'-bipyridyl)ruthenium(II) [42,43]. We also conducted microwave-induced synthesis of Tris (2,2'-bipyridyl)ruthenium(II) from the same starting material by using a commercial microwave source with a frequency and power of 2.45 GHz and 200.0±4.0 W (SHARP Co. Ltd., RE-TD1, irradiation time: 180.0 s) and compared the fluorescence spectra of the products with those of the products synthesized as described above. The wavelength of each fluorescence peak of Tris (2,2'-bipyridyl)ruthenium(II) (λ_1 = 607 nm, λ_2 = 758 nm) coincides with that of the products synthesized in the proposed microreactor. The reaction yield is estimated to ~85.7% by comparing the saturated magnitude of the 607 nm fluorescence peaks of the products synthesized by the commercial microwave source**.**

We also produced the Tris (2,2'-bipyridyl)ruthenium(II) by irradiating for only 120 s. The conventional method for synthesizing Tris (2,2'-bipyridyl) ruthenium(II) by heating in an oil bath requires several tens of hours. These results show that on-chip microwave-induced synthesis of Tris (2,2'-bipyridyl)ruthenium(II) occurs in the microfluidic channel with a high rate and yield [2].

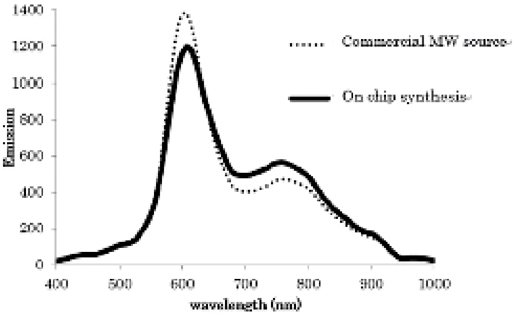

Fig.2 Fluorescence emission spectra of the products after microwave irradiation and starting materials before irradiation.

Conclusion

In this work, we demonstrate the on-chip synthesis of a ruthenium complex by using a microwave-induced reaction in a microfluidic channel integrated into a post-wall waveguide designed to contain 24.15 GHz microwave radiation. PTFE is used as the dielectric material wherein the microwaves propagate because it is an excellent chemical container owing to its low dielectric loss, high resistance to heat load (up to 300 °C), and chemical inertness. For this synthesis, the microwave frequency and power in the waveguide were 24.15 GHz and 3.0 W, the irradiation time was 120.0 or 600.0 s, and the solvent temperature was 70 °C. After microwave irradiation, the reaction products exhibit the specific fluorescence spectrum of Tris (2,2'-bipyridyl) ruthenium(II). Thus, this work demonstrates that a microwave-induced reaction in microfluidic channel integrated into a 24.15 GHz post-wall waveguide can be used for on-chip synthesis of a ruthenium complex with a high reaction rate and yield.

References

[1] P.L.Spencer, U.S.Patent 2 605 383,1952.
[2] Y .Utsumi *et al.*, Sensors and Actuators B **242**, 384-388 (2017).

Caltrop particles synthesized by X-ray radiolysis using synchrotron radiation

Akinobu Yamaguchi[1], Ikuo Okada[2], Ikuya Sakurai[2], Takao Fukuoka[1], and Yuichi Utsumi[1]
[1]Laboratory of Advanced Science and Technology, University of Hyogo
[2]Synchrotron Radiation Research Center, Nagoya University

Abstract

We report the synthesis of caltrop cupric oxide particles from the $Cu(CH_3COO)_2$ solution with an additive alcohol by X-ray radiolysis using synchrotron radiation. The particles were characterized by high-resolution scanning electron microscopy and micro-Raman spectrometry. These results indicate there are several synthetic routes to obtain caltrop particles and demonstrate the behavior of three-dimensional printers, enabling us to build composite material structure with metallic and other materials.

Introduction

The synthesis of various metallic and oxide particles has attracted considerable attention owing to the potential applications of functional nano- or micro-scale particles in various fields such as catalysis, medicine, electronics and optical-devices engineering. Recently, metallic and oxide particles have been synthesized via mnumerous methods such as sonochemical reaction, chemical reduction of metallic ions in aqueous solutions, and laser ablation and laser-induced photochemical reactions, etc.

X- or γ-ray irradiation has also been investigated as a radiation-assisted synthesis of gold particles on a silicon substrate was reported by Rosenberg and coworkers [1] and Yamaguchi *et al.*[2] In particular, the synchrotron radiolysis of these particles has also become a focus in engineering applications because it enables the generation of these particles from aqueous solutions of metallic salts. In addition, nano- or micro-scale structure consisting of functional materials can be tailored by immobilizing theses particles at a target location.

Cupric oxide (Cu_2O, CuO) particles which are p-type semiconductor materials with a low band energy have recently attracted much attention because the particles have been used in the anodes of lithium ion cells and pH sensors. The cupric particles have favorable characteristics; they are non-toxic, environmentally friendly, highly stable and recyclable.

We demonstrate the synthesis of micrometer-and submicrometer-scale cupric oxide (Cu_2O, CuO) particles using the X-ray synchrotron radiolysis from cupper (II) acetate $Cu(CH_3COO)_2$ solution. The synthesized cupric oxide particles exhibit unique morphologies that resemble caltrops, which are antipersonnel weapons made up of two or more sharp nails or spines; they have traditionally been used to slow the advance of horses, war elephants and human troops. They are often called “makibishi” in Japan, one of Ninja tools to damage the wheels of vehicles.

Experiments

The stock solution was made by dissolving 6.8 g of $Cu(CH_3COO)_2$ (Wako Chemical, 99.99%) in 100 mL of doubly distilled water. We syphoned off 200 µL of the solution into a microtube and added 10 µL ethanol to obtain the mixed solution. An 18 µL aliquot of the mixed solution was then exposed to X-ray irradiation as schematically shown in Fig. 1. In this study, a silicon substrate was dipped into the mixed solution and the specimen was placed on the irradiation system. The specimen was exposed to 5 min of X-rays and then washed using deionized water. The synthesized particles deposited on the silicon substrate were examined by field emission scanning electron microscopy with energy dispersive X-ray spectroscopy (EDX). In addition, we obtained Raman spectra using a micro-Raman spectrometer to determine the material characteristics of the synthesized particles.

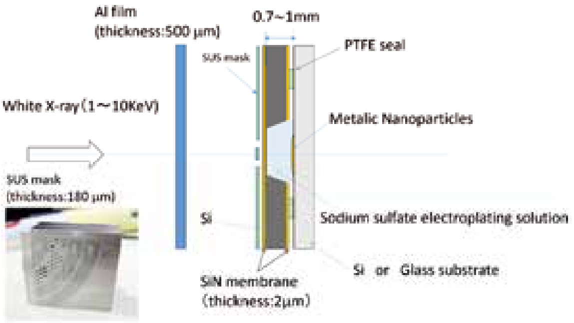

Fig. 1 Experimental setup for the X-ray irradiation of the $Cu(CH_3COO)_2$ solution.

Results and discussion

No particles were synthesized when the silicon substrate was immersed in an aqueous $Cu(CH_3COO)_2$ solution without ethanol and then exposed to X-rays. When ethanol was added to the $Cu(CH_3COO)_2$ solution, we obtain the particles immobilized on the substrate as typically shown in Fig. 2. [2]

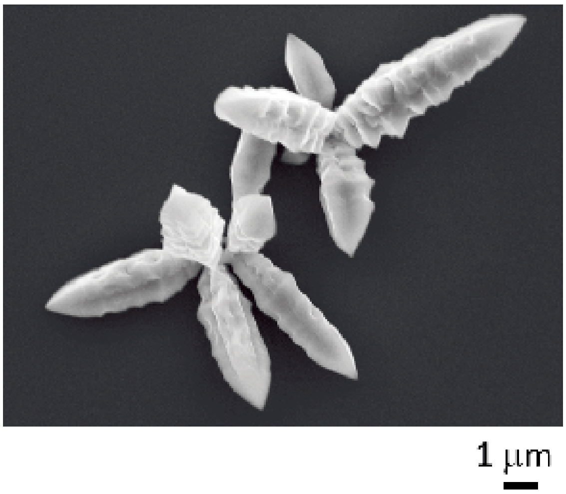

Fig. 2 SEM images of synthesized particles on silicon substrate dipped in an aqueous $Cu(CH_3COO)_2$ solution with ethanol.

Elementary analysis using EDX suggests that the caltrop particles comprise a mixture of species, such as Cu, CuO, Cu_2O and Cu_4O_3. To determine the composition of the cupric oxide particles, we measured the micro-lase Raman scattering spectra in Fig. 3. The Raman spectra is expected to be derived from Cu and CuO.

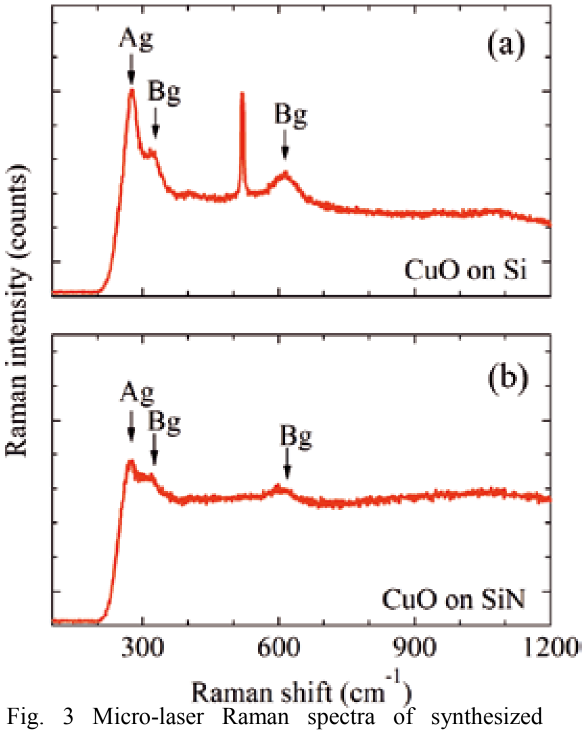

Fig. 3 Micro-laser Raman spectra of synthesized particles on (a) Si substrate and SiN membrane, respectively.

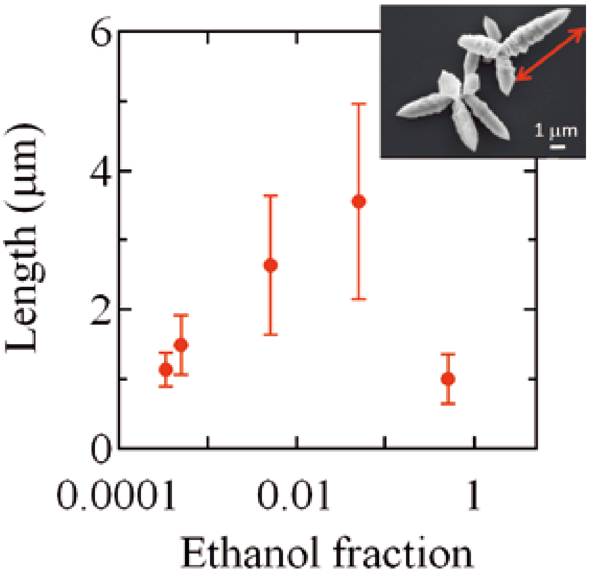

Fig. 4 The average and standard deviation of length of caltrop particles as a function of the fraction of ethanol.

The SEM images were also used to evaluate the average length of length of caltrop particles. Figure 4 summarizes ethanol fraction dependence of length of caltrop particles. The average length and standard deviation of the length depended on the concentration of ethanol, up to saturation concentration of 1/20. This trend was qualitatively predicted by typical reaction kinetics, whereby the added ethanol shows the reaction by adsorbing onto the surface of particles, preventing their growth.

Conclusion

The present work demonstrate that cupric particles can be obtained via a one-step synthesis in which an aqueous $Cu(CH_3COO)_2$ solution mixed with ethanol is exposed to X-ray irradiation at a synchrotron source. Using SEM microscopy and Raman spectroscopy, we determine that the caltrop particles comprise Cu and CuO. The alcohol that is added to the stick solution enables the copper ions to reduce the caltrop particles. This method can also provide novel lithography process to construct the additional nanostructures onto the previously patterned area.

References

[1] R. A. Rosenberg *et al*., J. Vac. Sci. Technol. B **16**, 3535 (1998); Q. Ma *et al*., Appl. Phys. Lett. **76**, 2014 (2000).

[2] A. Yamaguchi *et al*., Mater. Chem. Phys. **160**, 205 (2015); Jpn. J. Appl. Phys. **55**, 055502 (2016); J. Nanometer. 8584304 (2016); J. Synchrotron Radiation 24, 653 (2017).

High efficiency mixing for Lab-on-a-disk platform by utilizing Euler force

Masaya Takeuchi, Akinobu Yamaguchi, Yuichi Utsumi
Laboratory of Advanced Science and Technology, University of Hyogo

Abstract

Mixing of liquids in micro scale is generally difficult because a liquid unlikely to be turbulent flow, dominated by the viscous force. A mixing utilizing Euler-force can be applied to various application because the flow path structure is very simple. In previous research, this mixing method has been investigated for liquids of the same density. However, the investigation has not been performed for liquids of the different density. In this study, we examined the above effectiveness.

Introduction

Lab-on-a-disk, which controls solution by the rotation of the device, has drawn a great deal of interest in the field of microfluidic device. It is stable for chemical change of solution compared with liquid control by electrophoresis, and enables to form complex microfluidic network compared with liquid drive by syringe and peristaltic pumps. From above, it is expected in various field such as medical, biochemistry and environment. To construct a chemical reaction system on Lab-on-a-disk, it is essential that a mixing of liquids was performed in micro flow channel and reservoir. However, the mixing in micro scale is generally difficult because a liquid is unlikely to be turbulent flow, dominated by the viscous force. To solve this problem, a mixing methods using magnetic beads, Coriolis force and Euler force were presented so far. Especially Euler-force-mixing can be applied to various application because it is simple flow-path-structure and only performed by the rotation control of the device.

Euler-force is inertial force on rotating coordinate system which occurs perpendicularly to the radial direction depending on angular acceleration, and is given as

$$F_{euler} = r \cdot \frac{d\omega}{dt}$$

where r is the distance from the center of rotating coordinate system, and ω is angular frequency. The principle of the mixing is shown in Fig. 1. The magnitude of Euler-force depends on the distance from the center of rotating coordinate system, and liquids are mixed by utilizing the difference of these forces.

In previous research, this mixing method were investigated for liquids of the same density numerically and experimentally [1]. However, the investigation has not been performed for liquids of the different density. In this study, we examined the above effectiveness.

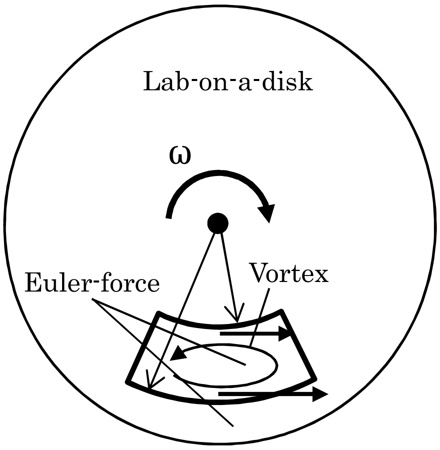

Fig. 1. Principle of Euler-force-mixing

Experiment

In this experiment, we used colored pure water (1.00 g/cm^2) and 1M phosphoric acid (1.05 g/cm^2). The evaluation of the mixing was performed by a standard deviation of gray scale of the shot image. The reservoir, where Euler-force-mixing was performed, was fabricated by punching. The diameter is 3 mm and the depth is 2.5 mm. Repeated Acceleration / deceleration of angular velocity is 1000 rpm/s for 1 second respectively.

Result and discussion

The standard deviation dependence on the number of this cycles is shown in Fig. 2. It was confirmed that the standard deviation decreases with increases of that cycles. It was 2.4 at 30 cycles. This value is almost the same as a standard deviation where these liquids is fully mixed. Therefore, we have confirmed the effectiveness of Euler-force-mixing for liquids of the different density.

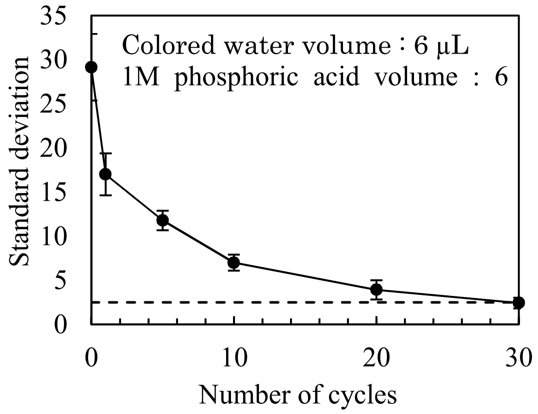

Fig. 2. Standard deviation dependence on number of cycles of acceleration / deceleration (1000 rpm /s) for 1 second respectively.

Conclusion

We investigated the effectiveness of Euler—force-mixing for liquids of the different density. As a result, we have confirmed that liquids with a specific gravity difference of 5 % can be mixed. It is expected that this mixing method can be further applied to various application

References

[1] Yong Ren, Wallace Woon-Fong Leung, International Journal of Heat and Mass Transfer, **60**, pp. 95-104 (2013).

Part 3. List of Publications

“Experiments of Material Engineering III” for third-year students in School of Engineering

List of publications

(1) Papers

1. **"Production of Medical 99mTc Isotope Via Photonuclear Reaction"**
M. Fujiwara, K. Nakai, N. Takahashi, T. Hayakawa, T. Shizuma, S. Miyamoto, G. T. Fan, A. Takemoto, M. Yamaguchi, and M. Nishimura
Physics of Particles and Nuclei, 2017, **48**, No. 1, pp. 124–133. © Pleiades Publishing, Ltd., 2017.

2. **"Effect of the nuclear medium on α-cluster excitation in ^{6}Li"**
T. Yamagata, S. Nakayama, H. Akimune, and S. Miyamoto
Physical Review C, **95**, pp.044307-1-10 (2017).

3. **"Coherent radiation at the fundamental frequency by a Smith-Purcell free-electron laser with dielectric substrate"**
D. Li, Y. Wang, M. Nakajima, M. Tani, M. Hashida, M. R. Asakawa, Y. Wei, and S. Miyamoto
Appl. Phys. Lett. , **110**, 151108-1-3 (2017).

4. **"Direct neutron-multiplicity sorting with a flat-efficiency detector"**
H. Utsunomiya, I. Gheorghe, D. M. Filipescu, T. Glodariu, S. Belyshev, K. Stopani, V. Varlamov, B. Ishkhanov, S. Katayama, D. Takenaka, T. Ari-izumi, S. Amano, S. Miyamoto
Nuclear Instrum. Methods Phy. Res. A, **871**, pp. 135-141 (2017).

5. **"Measurement of deflection on germanium and gold prisms using 1.7 MeV laser Compton scattering γ -rays"**
T. Kawasaki, S. Naito, Y. Sano, T. Hayakawa, T. Shizuma, R. Hajima, S. Miyamoto
Physics Letter A, vol. , **381**, Issue 36, pp. 3129-3133 (2017).

6. **"Low-lying Dipole Strength in 52Cr"**
T. Shizuma, T. Hayakawa, I. Daito, H. Ohgaki, S. Miyamato, and F. Minato
Physical Review C, **96**, 044316 (2017).

7. **"Photoneutron cross section measurements in the 209Bi(γ, xn) reaction with a new method of direct neutron-multiplicity sorting"**
I. Gheorghe, H. Utsunomiya, S. Katayama, D. Filipescu, S. Belyshev, K. Stopani, V. Orlin, V. Varlamov, T. Shima, S. Amano, S. Miyamoto, Y.-W. Lui, T. Kawano, and S. Goriely
Physical Review C, **96**, 044604 (2017).

8. **"Structural analysis of amorphous carbon films by BEMA theory based on spectroscopic ellipsometry measurement"**
XiaoLong Zhou, Satoru Arakawa, Sarayut Tunmee, Keiji Komatsu, Kazuhiro Kanda, Haruhiko Ito, and Hidetoshi Saitoh
Diamond & Related Materials 79C (2017) 46-59.

9. **"Soft X-ray irradiation effect on the fluorinated DLC film"**
Hiroki Takamatsu, Masahito Niibe, XiaoLong Zhou, Keiji Komatsu, Hidetoshi Saitoh, Hiroki Akasaka, Akihiro Saiga, Koji Tamada, Masahito Tagawa, Kumiko Yokota, Yuichi Furuyama, and Kazuhiro Kanda
Diamond & Related Materials 79C (2017) 14-20.

10. **"Formation of nanocrystalline silicon in SiOx by soft X-ray irradiation at low temperature"**
Akira Heya, Fumito Kusakabe, Naoto Matsuo, Kazuhiro Kanda, Kazuyuki Kohama, and Kazuhiro Ito
Japanese Journal of Applied Physics 56 (2017) 035501.

11. **"Modification Processes of Highly Hydrogenated Diamond-Like Carbon Thin Films by Soft X-ray Irradiation"**
Kazuhiro Kanda, Ryo Imai, Masahito Niibe, Hisashi Yoshioka, Keishi Komatsu, and Hidetoshi Saitoh
Sensors and Materials, 29 (2017) 817-826.

12. **"Structural analysis of amorphous carbon films by spectroscopic ellipsometry, RBS/ERDA, and NEXAFS"**
    XiaoLong Zhou, Tsuneo Suzuki, Hideki Nakajima, Keiji Komatsu, Kazuhiro Kanda, Haruhiko Ito, and Hidetoshi Saitoh
    Appl. Phys. Lett. 110 (2017) 201902.

13. **"Fabrication of DLC cone for fast ignition experiment"**
    Mayuko Koga, Kazuhiro Kanda, Tsuneo Suzuki, and Takayoshi Norimatsu
    Fusion Engineering and Design, 123 (2017) 120-123.

14. "ダイヤモンドをよく知るために　～量子ビーム利用測定技術（１）　X線吸収分光を用いた局所構造解析"
    神田一浩
    NEW DIAMOND, 126 (2017) 37-40.

15. "ＤＬＣ膜構造分析とＩＳＯ規格化"
    神田一浩
    応用物理, 86 (2017) 558-564.

16. **"Characteristics of TiO2 thin film surfaces treated by O2 Plasma in dielectric barrier discharge with the assistance of external heating"**
    Retsuo Kawakami, Masahito Niibe, Yoshitaka Nakano, Yuma Araki, Yuki Yoshitani, Chisato Azuma, Takashi Mukai
    Vacuum, 152, 265-271 (2018). doi: 10.1016/j.vacuum.2018.03.051

17. **"Nano-polycrystalline diamond synthesized from neutron-irradiated highly oriented pyrolytic graphite (HOPG)"**
    Mititaka Terasawa, Shin-ichi Honda, Keisuke Niwase, Masahito Niibe, Tomohiko Hisakuni, Tadao Iwata, Yuji Higo, Toru Shinmei, Hiroaki Ohfuji, Tetsuo Irifune
    Diamond & Related Materials, 82, 132-136 (2018).

18. **"Quenchable compressed graphite synthesized from neutron-irradiated highly oriented pyrolytic graphite in high pressure treatment at 1500°C"**
    Keisuke Niwase, Mititaka Terasawa, Shin-ichi Honda, Masahito Niibe, Tomohiko Hisakuni, Tadao Iwata, Yuji Higo, Takeshi Hirai, Toru Shinmei, Hiroaki Ohfuji, Tetsuo Irifune
    J. Appl. Phys. 123, 161577 (2018).

19. **"Characteristics of N2 and O2 Plasma-Induced Damages on AlGaN Thin Film Surfaces"**
    Retsuo Kawakami, Masahito Niibe, Yoshitaka Nakano, Ryo Tanaka, Chisato Azuma, Takashi Mukai
    Phys. Status Solidi, A214, 1700393 (2017).

20. **"Generation of electrical damage in n-GaN films following treatement in a CF4 plasma"**
    Yoshitaka Nakano, Retsuo Kawakami, Masahito Niibe
    Appl. Phys. Express, 10, 1162021 (2017).

21. **"TiO2 Thin Film Surfaces Treated by O2 Plasma in Dielectric Barrier Discharge with Assistance of Heat Treatment"**
    Retsuo Kawakami, Kengo Fijimoto, Masahito Niibe, Yuma Araki, Yoshitaka Nakano, Takashi Mukai
    Proc. 14th Int'l Symp. Sputtering & Plasma Processes (ISSP 2017), 274-277 (2017).

22. **"Laser plasma soft X-ray source based on cryogenic target"**
    S. Amano
    Proc. of SPIE, vol.10243, 10243Q (2017)

23. **"クライオターゲットによる「水の窓」レーザ生成プラズマ軟X線源"**
天野壮
電気学会論文誌 C, Vol.137, No.3, 406-410(2017)

24. **"Terahertz spectroscopy of graphene complementary split ring resonators with gate tenability"**
Satoru Suzuki, Yoshiaki Sekine, and Kazuhide Kumakura
Japanese Journal of Applied Physics 56, 095102-1-5 (2017).

25. **"Initial stage of hexagonal boron nitride growth in diffusion and precipitation method"**
Satoru Suzuki, Yui Ogawa, Shengnan Wang, Kazuhide Kumakura
Japanese Journal of Applied Physics 56, 06GE06-1-5 (2017).

26. **"Depth analysis of molecular orientation induced by nanoimprint graphoepitaxy"**
M. Okada, R. Fujii, Y. Haruyama, H. Ono, N. Kawatsuki, and S. Matsui
Jpn. J. Appl. Phys. 56 040302, 2017

27. **"Formation of complex molecular orientation patterns in nanostructures via double nanoimprint graphoepitaxy"**
Makoto Okada, Ryosuke Fujii, Yuichi Haruyama, Hiroshi Ono and Nobuhiro Kawatsuki
Appl. Phys. Express 10, pp. 105201, 2017

28. **"A study on enhancing EUV resist sensitivity"**
Atsushi Sekiguchi, Tetsuo Harada, Takeo Watanabe
Proc. SPIE 10143 (2017) 1014322.

29. **"ニュースバル放射光施設を活用したフォトマスク検査顕微鏡の開発"**
原田哲男
姫路工業倶楽部部報工学レポート vol. 28, 2017/1/1.

30. **"集光型コヒーレント回折イメージング法によるEUVマスク上の欠陥評価法の開発"**
原田哲男，橋本拓，渡邊健夫
電気学会論文誌 A, 137 (5), pp.260-264 (2017).

31. **"Imaging performance improvement of coherent extreme-ultraviolet scatterometry microscope with high-harmonic generation extreme-ultraviolet source"**
D. Mamezaki, T. Harada, Y. Nagata, and T. Watanabe
Jpn. J. Appl. Phys. 56, 06GB01 (2017).

32. **"Observation of EUVL mask using coherent EUV scatterometry microscope with high-harmonic-generation EUV source"**
D. Mamezaki, T. Harada, Y. Nagata, and T. Watanabe
Proc. SPIE 10454 (2017)1045413.

33. **"Resist Investigation Method using ab initio MO Calculation on basis of Approximation Molecular Model"**
S. Nagata, S. Niihara, T. Harada, and T. Watanabe
J. Photopolym. Sci. Technol. 30 (2017) 583.

34. **"Absorption Coefficient Measurement Advanced Method of EUV Resist by Direct-Resist Coating on a Photodiode"**
S. Niihara, D. Mamezaki, M. Watanabe, T. Harada, and T. Watanabe
J. Photopolym. Sci. Technol. 30 (2017) 87.

35. **"Evaluation of Block Copolymer Structure using Soft X-Ray Scattering"**
Y. Nakatani, T. Harada, A. Takano, M. Yamada, and T. Watanabe
J. Photopolym. Sci. Technol. 30 (2017) 77.

36. **"原子状水素を用いた Ni コートミラーの炭素汚染の除去"**
新部正人，原田哲男，部家彰，渡邊健夫，松尾直人
第 78 回応用物理学会秋季学術講演会予稿集，5a-S44-2 (2017).

37. **"軟 X 線散乱を用いたトリブロック共重合体構造の評価"**
中谷侑亮，原田哲男，高野敦志，山田素行，渡邊健夫
第 78 回応用物理学会秋季学術講演会予稿集，5p-S42-3 (2017).

38. **"軟X線 CMOS イメージセンサの特性評価"**
原田哲男，中谷侑亮，寺西信一，渡邊健夫
第 78 回応用物理学会秋季学術講演会予稿集，5p-S42-4 (2017)

39. **"フォトダイオード直接塗布法による EUV レジストの高精度な吸収係数測定法"**
新原章汰，豆﨑大輝，渡辺雅紀，原田哲男，渡邊健夫
第 78 回応用物理学会秋季学術講演会予稿集，5p-S42-5 (2017)

40. **"Synthesis of Hyperbranched Polyacetals containing C-(4-t-butylbenz)calix[4]resorcinarene; Resist Properties for Extreme Ultraviolet (EUV) Lithography"**
Hiroto Kudo, Mari Fukunaga, Kohei Shiotsuki, Hiroya Takeda, Hiroki Yamamoto, Takahiro Kozawa, Takeo Watanabe
Reactive and Functional PolymersREACT-D-18-00010.

41. **"半導体微細パターニング技術最前線（共著）～基礎から MEMS 技術、応用開発事例まで～**
第 2 章　EUV リソグラフィ技術、第 2 節　EUV 干渉露光技術"
渡邊健夫
株式会社エヌ・ティー・エス，2017.4.10.

42. **"EUV レジストの最前線（特集「第 16 回放射線プロセスシンポジウムの各論として掲載）"**
渡邊健夫
「放射線と産業」第 142 号，一般財団法人　放射線利用振興協会編

43. **"最新フォトレジスト材料開発とプロセス最適化技術"　河合晃　監修**
渡邊健夫
（株）シーエムシー出版，2017.9.

44. **"ＵＶ硬化技術を使った新製品開発（共著）**
第 8 章　UV 硬化型ソルダーレジスト、フォトレジストの設計と評価
第 7 節　EUV レジストのアウトガス評価、反応解析"
渡邊健夫
株式会社技術情報協会，2017.11.

45. **"Synthesis of cupric particles induced by X-ray radiolysis"**
A. Yamaguchi, I. Okada, T. Fukuoka, Y. Utsumi
IEEJ Transactions on Electronics, Information and Systems, vol. 137, No.3, pp. 400 -405 (2017), DOI: 10.1541/ieejeiss.137.400
"X 線照射による銅粒子生成"
山口明啓，岡田育夫，福岡隆夫，内海裕一
電気学会論文誌 C（電子・情報・システム部門誌）

46. **"A study for Sensitivity Improvement of 3-D Lab-on-a-CD based Immunosensor"**

Chiwa Kataoka, Tsukasa Azeta, Kazuyuki Sawadaishi, Yoshiaki Ukita, Akinobu Yamaguchi and Yuichi Utsumi
IEEJ Transactions on Electronics Information and Systems Vol. 137 No.3, pp. 418 – 423 (2017), DOI: 10.1541/ieejeiss.137.418
*Electronics and Communications in Japan, Vol. 101, No. 1, 2018 (Willey 英訳バージョン)

47. **"On-chip Synthesis of Ruthenium Complex by Microwave-Induced Reaction in a Microchannel Coupled with Post-Wall Waveguide"**
Y. Utsumi, A. Yamaguchi, T. Matsumura-Inoue, and M. Kishihara
Sensors & Actuator B: Chemical, 242, 384-388 (2017).

48. **"Interdigital Transducer Generated Surface Acoustic Waves Suitable for Powder Transport"**
Tsunemasa Saiki, Akio Tsubosaka, Akinobu Yamaguchi, Michitaka Suzuki, Yuichi Utsumi
Advanced Powder Technology 28, 491-498 (2017).

49. **"圧電体基板上に作製したNiCu合金微小磁性細線の磁気抵抗効果"**
山口明啓，大河内拓雄，保井晃，才木常正，内海裕一，木下豊彦，山田啓介
電気学会論文誌A, Vol. 137 (No. 8), pp. 487-488 (2017).
IEEJ Transaction on Fundamentals and Materials Vol. 138 (No. 8), pp. 487-488 (2017).

50. **"Caltrop particles synthesized by X-ray radiolysis in liquid phase with photochemical reaction"**
A. Yamaguchi, I. Okada, I. Sakurai, T. Fukuoka, M. Ishihara and Y. Utsumi
Journal of Synchrotron Radiation 24, 653-660 (2017).

51. **"Development of Bead-Based Multiplexed Immunoassay with Image Cytometric Analysis"**
Yoshiaki Ukita, Chiwa Kataoka, Kazuyuki Sawadaishi, Akinobu Yamaguchi, and Yuichi Utsumi,
Sensors and Materials, Vol. 29 (No. 5), 567-573 (2017).

52. **"Control of domain structure in artificial Ni wires fabricated on a LiNbO3 substrate"**
A. Yamaguchi, T. Ohkochi, A. Yasui, T. Kinoshita, K. Yamada
IEEE Transactions on Magnetics 53, 8108504 (2017).

53. **"X線を用いた熱化学異方性エッチングによるPTFEの微細加工プロセスの検討"**
山口明啓，木戸秀樹，竹内雅耶，内海裕一
電気学会論文誌E, Vol. 137 (No. 12) pp. 417-421

54. "金ナノ粒子のボトムアッププロセスで表面増強ラマン散乱活性なナノセンサー／ナノビーコンを造る"
福岡隆夫，山口明啓，内海裕一，倉本亮介，森康維
BUNSEKI KAGAKU Vol. 66 No.2 pp. 919-923 (2017).

55. **"Fabrication of Waveguide Butler Matrix for Short Millimeter-Wave by X-ray Lithography"**
M. Kishihara, M. Takeuchi, A. Yamaguchi, Y. Utsumi, I. Ohta
IEEE 978-1-5090-6360-4 DOI: 10.1109/MWSYM.2017.8058629 Conference: Conference: 2017 IEEE/MTT-S International Microwave Symposium - IMS 2017

56. **"Biofilm Formation Behaviors on Graphene by E. coli and S. epidermidis"**
H. Kanematsu, M. Sato, K. Shindo, D. M. Barry, N. Hirai, A. Ogawa, T. Kogo, Y. Utsumi, A. Yamaguchi, H. Ikegai, Y. Mizunoe
ESC Transactions, 80(10), 1167-1175 (2017).

57. **"Caltrop cupric oxide particles synthesized by X-ray photochemical reaction"**
A. Yamaguchi, I. Okada, T. Fukuoka, and Y. Utsumi
2017 International Conference on Electronics Packaging (ICEP 2017) Conference Proceedings IEEE Xplore, sponsored by JIEP (The Japan Institute of Electronics Packaging),IEEE CPMT Society Japan Chapter, iMAPS.

58. **"DIELECTROPHORESIS-ENABLED DYNAMIC FORMATION OF HIGHER-ORDER NANOSTRUCTURE CONSISTING OF AU-NANOPARTICLES-DECORATED POLYSTYRENE BEADS FOR SERS DETECTION"**
A. Yamaguchi, T. Fukuoka, and Y. Utsumi
Micro TAS 2017, W057c

59. **"放射光励起光プロセスと新しい応用展開"**
山口明啓, 内海裕一
公益社団法人　砥粒加工学会学会誌「特集　めっき技術における微細性」p535-538 (2017).
Journal of the Japan Society for Abrasive Technology Vo. 6, No. 10 (2017) Oct., pp. 535-538.

60. **"研究室だより：兵庫県立大学　材料・放射光専攻ナノマイクロシステム研究室"**
山口明啓
電気学会 E 部門誌　Vol. 138 (No. 2) , pp. 2

(2) International meetings

1. **"Performance measurement of HARPO: a Time Projection Chamber as a gamma-ray telescope and polarimeter"**
P. Gros, S. Amano, D. Atti´e, P. Baron, D. Baudin, D. Bernard, P. Bruel, D. Calvet, P. Colas, S. Dat´e, A. Delbart, M. Frotin, Y. Geerebaert, B. Giebels, D. G¨otz, S. Hashimoto, D. Horan, T. Kotaka, M. Louzir, F. Magniette, Y. Minamiyama, S. Miyamoto, H. Ohkuma, P. Poilleux, I. Semeniouk, P. Sizun, A. Takemoto, M. Yamaguchi, R. Yonamine, and S. Wang
arXiv:1706.06483v1 [astro-ph.IM] 20 Jun 2017 (2017).

2. **"M1 strength in photonuclear reactions with linearly polarized γ-ray beam"**
T. Hayakawa, T. Shizuma, K. Horikawa, S. Miyamoto, S. Amano, M. Yamaguchi, A. Takemoto, S. Chiba, H. Akimune, K. Ogata, M. Fujiwara
JPS Conf. Proc. 14, 021012 (2017).

3. **"Measurement of neutron spectra for photonuclear reaction with linearly polarized photonsr"**
Y. Kirihara, T. Itoga, T. Sanami1, H. Nakashima, Y. Namito1, S. Miyamoto, A. Takemoto, M. Yamaguchi, and Y. Asano
EPJ Web of Conferences 153, 01019 (2017). DOI: 10.1051/epjconf/201715301019

4. **"Measurement of neutron energy spectra for Eg=23.1 and 26.6 MeV mono-energetic photon induced reaction on natC using laser electron photon beam at NewSUBARU"**
T. Itoga, H. Nakashima, T. Sanami, Y. Namito, Y. Kirihara, S. Miyamoto, A. Takemoto, M.Yamaguchi and Y. Asano
EPJ Web of Conferences 153, 07010 (2017). DOI: 10.1051/epjconf/201715307010

5. **"Partial photoneutron cross section measurements on 209Bi"**
I. Gheorghe, D. Filipescu, S. Katayama, H. Utsunomiya, S. Belyshev, K. Stopani, V. Varlamov, T. Shima, Y.-W. Lui, S. Amano, and S. Miyamoto
EPJ Web of Conferences 146, 05011 (2017).

6. **"Photoneutron Reaction Data for Nuclear Physics and Astrophysics"**
H. Utsunomiya, T. Renstrøm, G. M. Tveten, I. Gheorghe, D. M. Filipescu, S. Belyshev, K. Stopani, H. Wang, G. Fan, Y.-W. Lui, D. Symochko, S. Goriely, A.-C. Larsen, S. Siem, V. Varlamov, B. Ishkhanov, T. Glodariu, M. Krzysiek, D. Takenaka, T.Ari-izumi, S. Amano1, S. Miyamoto
Proceedings of the CGS16 Conference (Shanghai, September 2017).

7. **"Erosion process of fluorinated diamond-like carbon films by exposure to soft X-rays"**
Kazuhiro Kanda, Hiroki Takamatsu, Eri Miura-Fujiwara, Hiroki Akasaka, Akihiro Saiga, Koji Tamada, Masahito Tagawa, Kumiko Yokota, and Yuichi Furuyama (invited)
The Collaborative Conference on Materials Research (CCMR), Jeju, South Korea, Jun. 26-30 (2017).

8. **"Classification of Hydrogen-Free and Hydrogenated DLC Films Prepared by Filtered Arc Deposition"**
Toru Harigai, Takahiro Imai, Yoshiyuki Suda, Hirofumi Takikawa, Masao Kamiya, Satoru Kaneko, Shinsuke Kunitsugu, Masahito Niibe, and Kazuhiro Kanda
IUMRS-ICAM 2017, Kyoto, Japan Aug. 27-Sep. 1 (2017).

9. **"DLC denture coating and the effect of prevention of contamination in oral cavity"**
Yuichi Imai, Kazuhiro Kanda, Yoko Kato, Teppei Horikawa, and Tatsuyuki Nakatani
Plasma Conference 2017, Himeji, Japan, Nov. 20-24 (2017).

10. **"Observation of B-K Emission and Absorption Spectra of Trace Boron Doped in HOPG"**

Masahito Niibe, Noritaka Takehira and Takashi Tokushima
The 8th International Symposium on Surface Science (ISSS-8), Tsukuba, Oct. 2017.

11. **"Surface Structure Analysis of AlGaN Thin Films Damaged by Oxygen and Nitrogen Plasmas"**
Masahito Niibe, Ryo Tanaka, Retsuo Kawakami, Yoshitaka Nakano and Takashi Mukai
The 8th International Symposium on Surface Science (ISSS-8), Tsukuba, Oct. 2017.

12. **"Generation Behavior of Electrical Damage Introduced into n-GaN Films by CF4 Plasma Treatments"**
Yoshitaka Nakano, Retsuo Kawakami and Masahito Niibe
29th International Conf. on Defects in Semiconductors (ICDS), Matsue, Aug. 2017.

13. **"TiO2 Thin Film Surfaces Treated by O2 Plasma in Dielectric Barrier Discharge with Assistance of Heat Treatment"**
Retsuo Kawakami, Kengo Fujimoto, Masahito Niibe, Yuma Araki, Yoshitaka Nakano and Takashi Mukai
Proc. 14th International Symp. Sputtering & Plasma Processes, 274-277, Kanazawa, Jul. 2017.

14. **"Laser Plasma soft X-ray Source Based on Cryogenic Target"**
S. Amano (Invited)
SPIE, Optics+Optoelectronics, Prague, Czech Republic, April 24-27, 2017.

15. **"Surface morphology changes of CVD-graphene/Cu{120} induced by post-annealing processes"**
Y. Ogawa, Y. Murata, S. Suzuki, H. Hibino, S. Heun, K. Kumakura
30th Int. Microprocess and Nanotechnology Conf. (MNC2017), Jeju, Korea, November 7 (2017).

16. **"Evolution of graphene alignment on recrystallizing polycrystalline Cu-foil for chemical vapor deposition growth"**
Yui Ogawa, Satoru Suzuki, Hiroki Hibino, Kazuhide Kumakura, Yoshitaka Taniyasu
Int. Symp. on Nanoscale Transport and Photonics 2017, Atsugi, November 14 (2017).

17. **"T Molecular orientation of photoreactive liquid crystalline polymer films observed by NEXAFS"**
Y. Haruyama, M. Okada, E. Nishioka, M. Kondo, N. Kawatsuki, and S. Matsui
European Congress and Exhibition on Advanced Materials and Processes (EUROMAT2017), Thessaloniki, Greece, 2017/9/19

18. **"CESIUM ION DOPED NICKEL OXIDE LAYERS FOR INVERTED PEROVSKITE SOLAR CELLS"**
Shota Fukumoto, Naoyuki Shibayama, Hiroyuki Kanda, Ajay Kumar Baranwal, Yuichi Haruyama, Hiroshi Segawa, Tsutomu Miyasaka, Seigo Ito
The 27th International Photovoltaic Science and Engineering Conference (PVSEC-27), Otsu, Japan 2017/11/14

19. **"Development of EUV Phase Imaging Microscope for Mask-3DEffect and Defect Evaluation"**
Tetsuo Harada, Daiki Mamezaki, and Takeo Watanabe
Photomask Japan, Yokohama, April 5 - 7, 2017.

20. **"NewSUBARU EUVL R&D Activities and EUV Mask Defect Inspection (Invited talk) "**
Takeo Watanabe, Tetsuo Harada
International Workshop on EUV Lithography, San Francisco, CA, USA, Jun. 12- 15, 2017.

21. **"Resist Investigation Method using ab initio MO Calculation on basis of Approximation Molecular**

Model"
S. Nagata, S. Niihara, T. Harada, and T. Watanabe,
The 34th International Conference of Photopolymer Science and Technology
Makuhari Messe, Chiba, Japan, Jun. 26-29, 2017.

22. **"Absorption Coefficient Measurement Advanced Method of EUV Resist by Direct-Resist Coating on a Photodiode"**
Shota Niihara, Daiki Mamezaki, Masanori Watanabe, Tetsuo Harada, Takeo Watanabe
The 34th International Conference of Photopolymer Science and Technology
Makuhari Messe, Chiba, Japan, Jun. 26-29, 2017.

23. **"Evaluation of Block Copolymer Structure using Soft X-ray Scattering"**
Yusuke Nakatani, Tetsuo Harada, Atsushi Takano, Motoyuki Yamada, Takeo Watanabe
The 34th International Conference of Photopolymer Science and Technology
Makuhari Messe, Chiba, Japan, Jun. 26-29, 2017.

24. **"EUV Lithography Research and Development Activities at University of Hyogo (Invited talk) "**
Takeo Watanabe
OSA Laser Congress 2017, Nagoya Congress Center, Oct.,.1-5, 2017.

25. **"Current Status and Prospect for EUV lithography (Panelist) "**
Takeo Watanabe
OSA Laser Congress 2017, Nagoya Congress Center, Oct.,.1-5, 2017.

26. **"EUV Lithography Research and Development Activities at University of Hyogo"**
Takeo Watanabe
IMEC meeting, Leuven, Belgium, Oct. 13, 2017.

27. **"Current Status and Prospect for EUV lithography (Plenary talk) "**
Takeo Watanabe
2017 7th International Conference on Integrated Circuits, Design, and Verification (ICDV2017), Hanoi, Vietnam, Oct. 5-6, 2017.

28. **"Observation of EUVL Mask Using Coherent EUV Scatterometry Microscope with High-Harmonic-Generation EUV Source"**
Daiki Mamezaki, Tetsuo Harada, and Takeo Watanabe
Photomask Japan, Yokohama, April 5-7, 2017.

29. **"Development of Polarization Control Unit with Broadband Mo/Si Multilayer for Accurate EUV Reflectometry"**
Masanori Watanabe, Tetsuo Harada, and Takeo Watanabe
Photomask Japan, Yokohama, April 5-7, 2017.

30. **"Large Collector Mirror Reflectometer for the High Power EUV Light Source Achievement"**
Takeo Watanabe and Tetsuo Harada Takeo Watanabe, Tetsuo Harada,
2017 International Workshop on EUV Lithography, San Francisco, CA, USA, Jun. 12- 15, 2017.

31. **"EUV Lithography Research and Development Activities at University of Hyogo"**
Takeo Watanabe and Tetsuo Harada
2017 International Workshop on EUV Lithography, San Francisco, CA, USA, Jun. 12- 15, 2017.

32. **"EUV resist development at NewSUBARU in University of Hyogo"**
    Takeo Watanabe, Shota Niihara, Shohei Nagata, Masahiro Watanabe, Daiki Memezaki, Tetsuo Harada
    Photomask Technology + Extreme Ultraviolet Lithography 2017, Monterey, CA, USA, 2017.9.11-14.

33. **"A Study of EUV Resist Sensitivity by using metal materials"**
    Atsushi Sekiguchi, Yoko Matsumoto, Yoshiyuki Utsumi, Michiya Naito, Takeo Watanabe and Tetsuo Harada
    Photomask Technology + Extreme Ultraviolet Lithography 2017, Monterey, CA, USA, 2017.9.11-14.

34. **"Development of the negative-tone molecular resists for EB/EUVL having high EUV absorption capacity, and molecular design method"**
    Takashi Sato, Tomoaki Takigawa, Yuta Togashi, Takumi Toida, Masatoshi Echigo, Tetsuo Harada, Takeo Watanabe, Hiroto Kudo
    Photomask Technology + Extreme Ultraviolet Lithography 2017, Monterey, CA, USA, 2017.9.11-14.

35. **"Development of EUV phase imaging microscope for mask-3D-effect and defect evaluation"**
    Tetsuo Harada, Daiki Mamezaki, Yusuke Nakatani, Takeo Watanabe
    Photomask Technology + Extreme Ultraviolet Lithography 2017, Monterey, CA, USA, 2017.9.11-14.

36. **"Caltrop cupric oxide particles synthesized by X-ray photochemical reaction"**
    A. Yamaguchi, I. Okada, T. Fukuoka, and Y. Utsumi2017 International Conference on Electronics Packaging (ICEP 2017), Yamagata, Japan, 2017/4/20

37. **"Control of domain structure in artificial Ni wires fabricated on a LiNbO3 substrate"**
    A. Yamaguchi, T. Ohkochi, A. Yasui, T. Kinoshita, K. Yamada
    Intermag 2017, Dublin, Ireland, 24th-28th, April, 2017

38. **"Dielectrophoresis-enabling Dynamic Formation of Higher-Order Nanostructure Consisting of Au-nanoparticles-Decorated Polystyrene Beads for SERS Detection"**
    A. Yamaguchi, T. Fukuoka, Y. Utsumi
    The 21st International Conference on Miniaturized Systems for Chemistry and Life Sciences (MicroTAS 2017), Savannah, USA, 22nd-26th, Oct., 2017

39. **"Strain-induced magnetic properties of micro-scale artificial magnets on ferroelectric LiNbO3 substrate"**
    A. Yamaguchi, K. Ueda, T. Nakajima, Y. Utsumi, T. Ohkochi, A. Yasui, T. Kinoshita, K. Yamada
    The 62nd Annual Conference on Magnetism and Magnetic Materials (2017 MMM), Pittsburgh, USA, November 6th-10th, 2017

40. **"Ferromagnetic resonance of Ni wires fabricated on ferroelectric LiNbO3 substrate for studying strain-induced magnetic properties"**
    A. Yamaguchi, K. Ueda, T. Nakajima, Y. Utsumi, K. Yamada
    The 62nd Annual Conference on Magnetism and Magnetic Materials (2017 MMM), Pittsburgh, USA, November 6th-10th, 2017

41. **"Plasmonic Nanobeacon Based on Gold Nanoparticle Self-assembly for Universal Bio-Nanosensing"**
    T. Fukuoka, A. Yamaguchi, Y. Mori
    The first International Workshop by the 174th Committee JSPS “Symbiosis of Biology and Nanodevices”（第 174 委員会主催国際ワークショップ「Symbiosis of Biology and Nanodevices」）, Kyoto, Dec. 21st, 2017

(3) Academic degrees

1. Doctor of Engineering

Chiwa Kataoka (University of Hyogo)
作付け前診断のための土壌残留ヘプタクロル類の免疫学的測定法の構築と Lab-on-a-CD への応用に関する研究
"Construction of immunoassay of heptachlor as a soil residue for diagnosis before cropping and its application to Lab-on-a-CD"

2. Master of Engineering

Kento Sugita (University of Hyogo)
レーザーコンプトン散乱ガンマ線の発生と陽電子非破壊検査システムの開発
"Development of Positron Non-destructive Inspection System Using Laser Compton Scattering Gamma-ray"

Shohei Nagata (University of Hyogo)
分子軌道計算法を用いた軟 X 線吸収分光測定によるレジスト評価手法の検討
"EUV Resist Evaluation Using Soft X-Ray Absorption Spectroscopy and Molecular Orbital Calculation"

Yusuke Nakatani (University of Hyogo)
有機材料化学状態分布評価用の軟 X 線透過顕微鏡および共鳴散乱測定手法の開発
"Developments of Scanning Transition Soft X-ray Microscope and Resonant Soft X-ray Scattering Method for Distribution Evaluation of Chemical State in Polymers"

Masanori Watanabe (University of Hyogo)
EUV リソグラフィ用多層膜の高精度反射率測定法の開発、並びにカシミール力測定用のピットパタン製作
"Development of Accurate Reflectometry of EUV Multilayer for EUV lithography, and Pit Pattern Fabrication for Cacimir-Force Evaluation"

Daiki Mamezaki (University of Hyogo)
EUV マスクパタン像観察のための高次高調波回折顕微鏡の開発
"Development of Standalone Diffraction Microscope with High-Harmonic-Generation EUV Coherent Source for EUV Mask-Pattern Observation"

LASTI Annual Report Vol.19 (2017)

September 2018, Published by
Laboratory of Advanced Science and Technology for Industry
University of Hyogo
3-1-2 Kouto, Kamigori-Cho, Ako-gun, Hyogo 678-1205, JAPAN
Phone: +81-791-58-0249 / FAX: +81-791-58-0242

Laboratory of Advanced Science and Technology for Industry
University of Hyogo

3-1-2 Kouto, Kamigori, Ako-gun, Hyogo 678-1205 Japan

兵庫県立大学 高度産業科学技術研究所
〒678-1205 兵庫県赤穂郡上郡町光都 3-1-2